TopmetalSe: Development of a CMOS Imager for Selena

Xiaochen Ni

A dissertation
submitted in partial fulfillment of the
requirements for the degree of

Doctor of Philosophy

University of Washington

2025

Reading Committee:
Alvaro Chavarria, Chair
Jason Detwiler
Shih-Chieh Hsu

Program Authorized to Offer Degree:
Physics

University of Washington

Abstract

TopmetalSe: Development of a CMOS Imager for Selena

Xiaochen Ni

Chair of the Supervisory Committee:
Alvaro Chavarria
Physics

The Selena experiment couples an amorphous selenium (aSe) ionization target to a custom complementary metal–oxide–semiconductor (CMOS) pixel array to create an imaging detector for next-generation neutrino physics. Hybrid aSe/CMOS devices combine the high-Z stopping power and room-temperature operation of aSe with the fine-pitch, low-noise readout of modern CMOS sensors, enabling precise reconstruction of ionization tracks for advanced background discrimination.

This work presents the comprehensive simulated modeling and hardware development of Selena as a candidate search for neutrinoless double-beta decay ($0\nu\beta\beta$) in ^{82}Se. A detailed simulation framework is developed to model double-beta events in a Selena detector, incorporating charge generation, drift, and collection processes, along with dedicated reconstruction techniques for event topology and energy response. In parallel, the Topmetal-Se prototype, fabricated in the open-source SkyWater 130 nm CMOS process, demonstrates direct charge sensing, low noise, and fine pixel pitch ionization track imaging when coupled to amorphous selenium.

Together, these developments establish Selena as a viable platform for high-resolution ionization imaging and rare-event detection.

TABLE OF CONTENTS

LIST OF FIGURES

LIST OF TABLES

GLOSSARY

ADC: Analog-to-Digital Converter

ASIC: Application-Specific Integrated Circuit

ASE: Amorphous Selenium

BSM: Beyond the Standard Model — theoretical extensions to the Standard Model of particle physics

CNO: Carbon-Nitrogen-Oxygen — one of the fusion cycles in stars that produce solar neutrinos

DAC: Digital-to-Analog Converter

ENC: Equivalent Noise Charge

FPGA: Field-Programmable Gate Array

GUARD RING: Guard Ring — a perimeter electrode used for field shaping and leakage current suppression

HV: High Voltage

MPW: Multi-Project Wafer — a shared silicon fabrication run used for prototyping ASICs

$Q_{\beta\beta}$: Q-value of double beta decay

ROI: Region of Interest

SNR: Signal-to-Noise Ratio

TDC: Time-to-Digital Converter

TOA: Time of Arrival

TFT: Thin-Film Transistor

TSV: Through-Silicon Via — a vertical electrical connection passing through a silicon wafer

UART: Universal Asynchronous Receiver-Transmitter — a protocol for serial communication

ACKNOWLEDGMENTS

Working within the Selena collaboration has been one of my most meaningful experiences; its small size provided close mentorship and the opportunity to lead significant parts of the project. I am grateful to everyone who has been a part of the collaboration. I would especially like to thank Alvaro Chavarria. From the moment he invited me to join the group, he recognized of projects that would challenge and motivate me. Since then, he has offered thoughtful guidance at every step while giving me the independence to grow as a researcher. Every discussion with him opened new directions for the project, and I am grateful for his trust in my ability to take ownership of Selena.

A defining point of my Ph.D. was Yuan Mei's proposal that I learn and design integrated circuits, which was an ambitious step for me. The many hours spent over a VNC client on Zoom with him remain some of my most memorable learning experiences. His confidence and mentorship enabled me to develop a unique and lasting skillset, for which I am deeply grateful.

Although brief, my overlap with former graduate students Xinran Li and Alex Piers formed the foundations of my Ph.D. This work was built on their previous efforts. I also cannot express enough gratitude for the expertise of the CENPA engineering staff. I would especially like to recognize the relentless effort, surgical hand, patience and humor of Marcel Conde, whose contributions have been essential to this work.

A wide range of friends have formed the backdrop of my Ph.D. experience. From starting the program virtually during COVID, the cohort of students I started with

shaped this journey in ways I did not anticipate, offering support, humor, and banter through every phase of graduate school. The many jokes and conversations over lunches, group chats, and hangouts will always be remembered. The people who stopped to say hi and chat in the halls of CENPA, WNF, or the IMA also helped make UW a wonderful place to call home during my Ph.D. Lastly, Teresa—and Simba[1]—have been a highlight of the latter half of this journey, bringing encouragement and joy outside the lab. Whether through countless activities or accompaniment during long hours in the office, Teresa has made my efforts feel more enjoyable and far easier to navigate.

My Ph.D. would not have been possible without the support of my parents. Any accomplishments of mine rest on their decision to move to the United States in support of me and my chance to grow up with better opportunities and education.

Thank you all.

[1]Formosan Mountain Dog

Chapter 1

INTRODUCTION

The story of the neutrino begins with the first experimental observation of beta decay in 1899 by Ernest Rutherford [1]. In his study of radiation from uranium compounds, Rutherford identified beta rays as a distinct form of energetic emission, later identified to be high speed electrons emitted during nuclear decay. However, the measured continuous beta-decay energy spectrum was unlike a two-body nuclear decay, demonstrating an apparent violation of conservation of energy. In the 1930s, Wolfgang Pauli and Enrico Fermi developed a theory for beta decay, in which this missing energy was carrier away by the *neutrino* [2, 3].

Over the 20th century, this discovery played a key role in unveiling the complex structure and behavior of the atom. Experimental results and their theoretical descriptions demonstrated that neutrinos were essential to understanding our universe, from the forces governing subatomic particles to the formation and behavior of our entire universe.

Yet, despite their abundance and significance, neutrinos remain some the more mysterious particles in the Standard Model of physics. Key questions about their fundamental nature remain unresolved: Are neutrinos their own antiparticles (Majorana particles), or are they distinct (Dirac)? What are their masses, and how are those masses ordered? Do neutrinos violate CP symmetry, and could this help explain the matter-antimatter asymmetry [4]? Lastly, are there more than the three types of neutrinos, known as sterile neutrinos [5]?

Ongoing theoretical and experimental investigations throughout the 21st century continue to probe these fundamental questions. One of the most focused efforts is the search for neutrinoless double beta decay ($0\nu\beta\beta$). Its elusiveness has driven scientific innovation across many fields, including nuclear theory, detector technology, low-background materials science, and large-scale data analysis. This thesis will describe the R&D efforts of one such initiative:

the Selena Neutrino Experiment, a future-generation search for $0\nu\beta\beta$ using hybrid amorphous Selenium/CMOS detectors.

1.1 Detection of Charge Particles

The Standard Model of particle physics describes the nature of subatomic particles and their interactions [6, 7]. Among its key successes is its ability to account for various forms of nuclear decay by categorizing them according to the fundamental forces involved. These decay processes form the foundation of nuclear physics and are traditionally grouped into three primary types:

- α, where the nucleus emits a helium nucleus ($^4_2$He). It is governed by the electromagnetic and strong nuclear force.
- γ, where a nucleus emits a high-energy photon, governed by the electromagnetic force.
- β, where a neutron is converted in a proton (or vice versa) and an electron (positron) and a neutrino (antineutrino) are emitted. It is governed by the weak nuclear force.

Of particular relevance to this thesis is the measurement and detection of these three types of radiation. Historically, the three types of emission from these decays were measured by their penetration depth in different materials and air. Alpha particles, being large and highly charged, lose energy rapidly through ionization and thus travel only a few centimeters in air or micrometers in solid matter. Beta particles, penetrate further but are still easily stopped by thin layers of metal or plastic. Gamma rays interact weakly with matter and can travel several centimeters in dense materials, making them the most penetrating of the three.

While penetration depth remains an important characteristic for distinguishing these radiation types, modern detectors employ more sophisticated methods to provide clearer identification. These methods take advantage of the different physical interactions each type of radiation undergoes within the detector material. Key distinguishing features include energy deposition patterns, track topology, and timing characteristics:

- **Energy deposition:** Charged particles deposit energy by interacting with electrons in the detector medium. Alpha particles, with their charge and large mass, deposit a large amount of energy in a very short distance, creating a high dE/dx profile in a detector [8, 9]. Beta particles, on the other hand, distribute their energy over a longer distance through ionization or δ-ray emission, resulting in more gradual energy loss profile [10]. Gamma rays, being uncharged, interact with the detector medium only indirectly: photoelectric absorption, Compton scattering, and pair production transfer the gamma energy to secondary electrons, which then produce observable ionization.These processes yield energy spectra distinct from alpha and beta interactions. Examples include Ref. [11–13].

- **Track topology:** The path left by a particle as it travels through the detector (its track) provides a distinct signature. Alpha particles, with their larger mass and charge, create short, localized tracks, often with a rapid loss of energy at the end of their path, known as a Bragg peak. Beta particles create longer, thinner tracks which also end in Bragg peaks, and gamma rays typically do not leave tracks at all but the generated secondary electrons induce distinct tracks. Examples include Ref. [13, 14].

- **Timing characteristics:** In some advanced detectors, the timing of a particle's arrival and its interaction with the detector is used to distinguish between types of radiation. For example, alpha particles tend to cause a sudden burst of energy, producing a sharp peak in timing data on the order of nanoseconds. Beta particles and gamma rays can interact over multiple interactions extending over tens to hundreds of nanoseconds [9,10]. Timing information is particularly useful in high-energy physics and other specialized applications where multiple radiation types might be present simultaneously. Examples include Ref. [15–17].

1.2 Beta Decay and Neutrino Physics

Beta decay is described by:

$$\beta^{-}\text{decay} : n \rightarrow \bar{\nu_e} + p + e^{-}$$

$$\beta^{+}\text{decay} : p \rightarrow \nu_e + n + e^{+}$$

While early formulations of beta decay failed to account for the neutrino, its presence is critical to preserve the conservation laws of the Standard Model. When measuring the energies of the proton and the electron following the decay, experimental results indicated the total energy of the decay products was lower than the energy of the original particle. The discovery of the neutrino was essential for explaining the *missing energy problem* in the decay process. Its inclusion preserves the conservation laws of the Standard Model, including those of energy, momentum and angular momentum. In addition, the total lepton number (which counts leptons and antileptons) and the individual lepton flavor numbers (which count lepton flavor) is conserved in each of the decay processes [6].

In the Standard Model, neutrinos are defined as massless neutral fermions with a spin of 1/2. They interact exclusively via the weak force, mediated by the W and Z bosons. The weak force is unique in that it couples only to particles with specific chirality states, specifically left-handed particles and right-handed antiparticles. This condition is essential for understanding the behavior of neutrinos, which are spin-1/2 chiral particles. For massless particles, helicity (the projection of spin along the direction of momentum) coincides with chirality, and this explains why neutrinos are observed only with left-handed helicity and antineutrinos with right-handed helicity [18]. If neutrinos had mass, helicity would no longer be Lorentz-invariant as massive particles can have their helicity flipped in another frame. Thus, observation of definite helicity historically supported the assumption of zero mass [6,7].

The Standard Model includes three distinct neutrino flavors: electron (ν_e), muon (ν_μ) and tau (ν_τ), corresponding to the three charged leptons. This structure aligns with the con-

servation of lepton flavor in weak interactions, which ensures that the flavor of the neutrino remains conserved in a process like muon decay:

$$\mu^- \rightarrow e^- + \bar{\nu_e} + \nu_\mu \tag{1.1}$$

where the outgoing neutrinos preserve the distinct lepton numbers associated with the muon and electron families. The electron neutrino was originally discovered in 1956 by the Cowan-Reins Experiment, the muon neutrino in 1962 by Brookhaven National Lab and the tau neutrino in 2000 at Fermilab [19–21].

1.2.1 Beyond the Standard Model (BSM)

The observation of neutrino oscillations revealed a fundamental shortcoming in the Standard Model's description of neutrinos. Much like the missing energy problem in beta decay, an anomaly known as the *solar neutrino problem* hinted at new physics. In the 1960s, the Homestake experiment measured the flux of neutrinos produced by nuclear fusion in the Sun, which was predicted to produce only electron neutrinos (further discussion of solar neutrinos can be found in Chapter 2). However, the experiment consistently detected only about one-third of the expected number of electron neutrinos [22].

The resolution came with the discovery of *neutrino oscillations*, confirmed definitively by the SNO collaboration in 2001 [23]. Neutrino oscillation is described theoretically by the Pontecorvo–Maki–Nakagawa–Sakata (PMNS) matrix [6, 24], which characterizes the mixing between the three neutrino flavor eigenstates (ν_e, ν_μ, ν_τ) and the three mass eigenstates (ν_1, ν_2, ν_3). As neutrinos propagate, they oscillate between these flavor states. The solar neutrino deficit was thus explained by two-thirds of the emitted electron neutrinos oscillating into muon or tau neutrinos through a combination of matter-enhanced (MSW) conversion into ν_2 in the Sun, yielding an electron-neutrino survival probability of $\approx 1/3$ [25]. While several parameters of the PMNS matrix, such as the mixing angles and mass-squared differences [24], have been measured with increasing precision, others, such as the CP-violating phase and the mass ordering, remain unknown. A large experimental program, including next-generation

experiments like JUNO, DUNE and Hyper-Kamiokande, is actively working to complete the PMNS matrix [26–28].

Crucially, neutrino oscillations imply that neutrinos have nonzero mass. Since only particles with mass can have distinct phase evolution in time, the ability of neutrinos to oscillate as they travel is direct evidence that they are not massless. This serves as direct evidence against the Standard Model's description of neutrinos. However, the absolute scale of neutrino masses remains unknown, with current constraints suggesting they lie below the eV-scale.

Cosmological observations place a model-dependent upper limit on the total mass of the three neutrino mass eigenstates:

$$\sum m_i < 0.12 \text{ eV} \quad (95\% \text{ CL}) \tag{1.2}$$

as constrained by measurements of cosmic microwave background anisotropies and large-scale structure [29]. Meanwhile, laboratory-based measurements such as those from the KATRIN experiment provide a complementary, model-independent upper bound on the effective electron neutrino mass [30]:

$$m_\nu < 0.45 \text{ eV} \quad (90\% \text{ C.L.}) \tag{1.3}$$

$$m_\nu^2 = \sum_i U_{ei}^2 m_i^2 \tag{1.4}$$

where U_{ei} are elements of the PMNS matrix, encoding the mixing between flavor and mass eigenstates. Together, they place a strict upper bound on the neutrino mass eigenstates, but their exact values remain a mystery.

In the Standard Model, neutrinos are treated as massless because only left-handed neutrino fields (ν_L) are included in the particle content. In order for a fermion to acquire a (Dirac) mass through the Higgs mechanism, like the charged leptons and quarks, both left- and right-handed chiral components are required. In the absence of a right-handed neutrino, such a coupling is not possible for neutrinos. Moreover, typical fermion masses range from about 0.5 MeV for the electron to 173 GeV for the top quark, whereas the neutrino mass scale

is at least six orders of magnitude smaller. This extreme disparity not only underscores the mystery of neutrino mass generation but also strongly motivates extensions to the Standard Model [7].

A leading explanation is the inclusion of Majorana mass terms, which allow neutrinos to be their own antiparticles. Such a term is not permitted within the Standard Model's renormalizable interactions but becomes possible in extended models. The most compelling of these is the *Type-I seesaw mechanism*, which introduces a heavy right-handed neutrino with Majorana mass $M_H \sim 10^{11}$ GeV and a Dirac mass $m_D \sim 1$ GeV. The Dirac mass term m_D is analogous to the fermion masses and couples to both left and right-handed neutrino states, while the Majorana mass term M_H couples only to the right-handed neutrino. Such a mass term would allow for lepton number violation. Diagonalizing the mass matrix leads to the relation [31]:

$$m_\nu \approx \frac{m_D^2}{M_H} \approx 0.01 \text{ eV} \tag{1.5}$$

This mechanism explains the tiny neutrino mass while providing a simple extension to the Standard Model. The heavy Majorana neutrino itself, being extremely massive and unstable, is unobservable in current experiments. Thus, indirect confirmation may come through lepton-number violating processes, such as neutrinoless double beta decay.

An interesting implication of the seesaw mechanism is the possibility of leptogenesis—a theoretical framework explaining the matter-antimatter asymmetry in the universe. In the early universe, the heavy right-handed neutrinos of the seesaw mechanism decay into leptons and Higgs bosons. Due to CP violation in these decays, a small excess of antileptons over leptons can be generated. This lepton asymmetry can then be converted into a baryon asymmetry via electroweak sphaleron processes [32, 33], offering a viable mechanism for baryogenesis.

Another open question is the mass ordering problem, which describes the pattern of the neutrino mass eigenvalues. Oscillation experiments have established two mass-squared differences, known as the solar and atmospheric splittings, but not whether the mass eigenstates

follow a *normal hierarchy* ($m_1 < m_2 < m_3$) or an *inverted hierarchy* ($m_3 < m_1 < m_2$). Current and future experiments such as JUNO, DUNE, and Hyper-Kamiokande aim to directly measure this ordering [26–28].

Finally, there remains the possibility of additional *sterile* neutrinos one that do not couple via the weak interaction. Sterile neutrinos are motivated by anomalies in short-baseline neutrino experiments such as LSND and MiniBooNE [34,35], which observed deficits inconsistent with the three-neutrino framework. These results, however, are in tension with null results from other experiments [17, 36], and sterile neutrinos remain one of the most intriguing potential hints of physics beyond the Standard Model.

1.3 Neutrinoless Double Beta Decay

Neutrinoless Double Beta Decay ($0\nu\beta\beta$) offers a powerful probe into BSM physics. In standard double-beta decay ($2\nu\beta\beta$),

$$(A, Z) \rightarrow (A, Z + 2) + 2e^- + 2\bar{\nu_e} \tag{1.6}$$

two antineutrinos are emitted alongside two electrons. However if neutrinos are Majorana particles, they can annihilate and only the electrons are emitted:

$$(A, Z) \rightarrow (A, Z + 2) + 2e^- \tag{1.7}$$

By the Schechter-Valle theorem, observation of this process would demonstrate that the neutrino has a nonzero Majorana mass [4], prove lepton number violation and provide support for models like the seesaw mechanism that predict Majorana neutrinos.

Double beta decay is a very rare process, with extremely long half-lives, and it occurs only in certain nuclei. It becomes possible only when ordinary (single) beta decay is energetically forbidden or highly suppressed. For example, in ^{82}Se, single beta decay would produce the intermediate nucleus ^{82}Br, which is heavier than the parent and therefore cannot be formed. In such cases, double beta decay can be allowed via the emission of two electrons in a second-order weak process. This occurs in isotopes such as ^{76}Ge, ^{82}Se, ^{100}Mo, ^{136}Xe. The half-life/decay rates for the two processes are [4]:

$$\Gamma_{1/2} = \left[T^{2\nu}_{1/2}\right]^{-1} = G^{2\nu}(Q,Z) \cdot \left|M^{2\nu}\right|^2 \tag{1.8}$$

$$\Gamma_{1/2} = \left[T^{0\nu}_{1/2}\right]^{-1} = G^{0\nu}(Q,Z) \cdot \left|M^{0\nu}\right|^2 \cdot \left(\frac{\langle m_{\beta\beta}\rangle}{m_e}\right)^2 \tag{1.9}$$

where $G(Q,Z)$ is the phase space factor, M is the nuclear matrix element, $\langle m_{\beta\beta}\rangle$ is the effective Majorana neutrino mass, and m_e is the electron mass. The phase-space factor G(Q,Z) grows rapidly with both Q-value, which enlarges the kinematically allowed region for the emitted electrons, and atomic number Z, which enhances the electron wavefunctions at the nucleus through Coulomb attraction. The nuclear matrix element M encodes the nuclear structure information and the transition dynamics. However, its calculation remains a major theoretical uncertainty due to its strong dependence on nuclear models. Equation 1.8 assumes neutrinoless double beta decay mediated by the exchange of light, left-handed Majorana neutrinos. However, many alternative mechanisms can also induce $0\nu\beta\beta$ decay, which predict certain energy distributions, angular correlations, and event topologies.

For $0\nu\beta\beta$, the effective Majorana mass $\langle m_{\beta\beta}\rangle$ is:

$$|m_{\beta\beta}| = \left|\sum_i |U_{ei}|^2 m_i\right| \tag{1.10}$$

where U_{ei} comes from the PMNS matrix. Writing $\langle m_{\beta\beta}\rangle$ in terms of known and unknown parameters [4]:

$$m_{\beta\beta} = c^2_{12}c^2_{13}m_1 e^{2i\lambda_a} + s^2_{12}c^2_{13}e^{2i\lambda_b}\sqrt{m_1^2 + \Delta m^2_{12}} + s^2_{13}\sqrt{m_1^2 \pm |\Delta m^2_{23}|} \tag{1.11}$$

where c_{ij} and s_{ij} are the trigonometric functions of PMNS mixing angles, Δm^2_{ij} are the squared mass differences, λ_a, λ_b are known as the Majorana phases, and m_1 is the lightest neutrino mass. The $\pm$ is a direct result of the mass ordering question, while the Majorana phases arise if neutrinos are Majorana particles. These unknowns, particularly the phases and m_1, make precise predictions of $\langle m_{\beta\beta}\rangle$ difficult. Figure 1.1 illustrates this dependence via the so-called "lobster plot." Thus, direct measurement of $T_{1/2}$ not only probes the Majorana nature of neutrinos, but also constrain the absolute neutrino mass scale and possibly resolve the mass hierarchy.

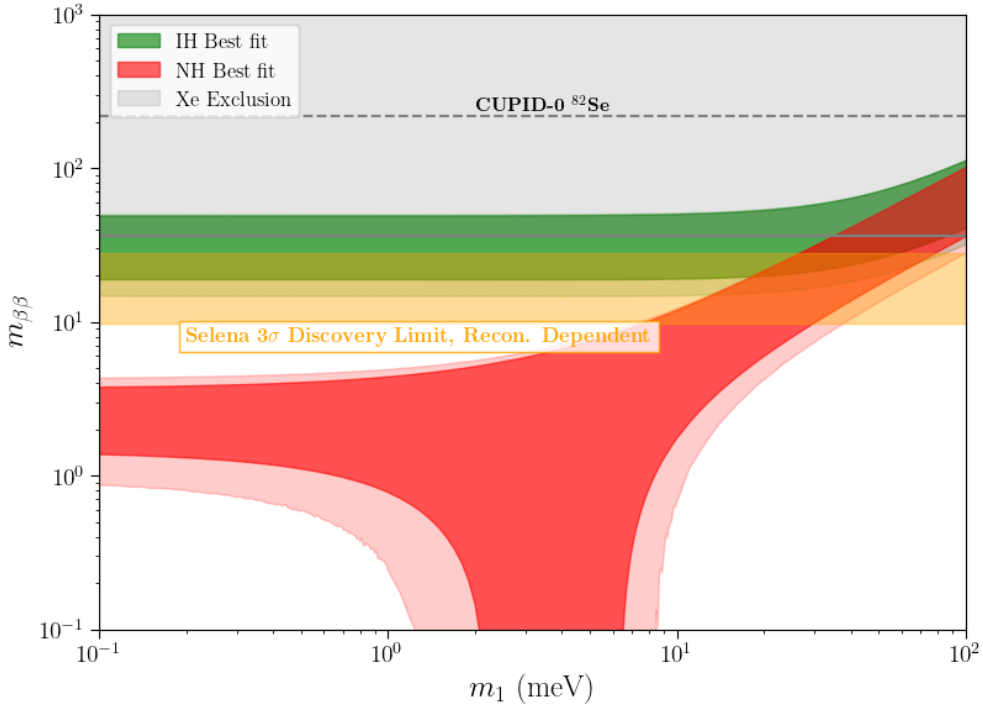

Figure 1.1: **$0\nu\beta\beta$ Lobster Plot** Plotted limits are from Ref. [37, 38]. Selena (this work) discovery limit is discussed in section 2.8. Band reflects uncertainties in both the nuclear matrix element and final detector properties and reconstruction techniques.

1.4 $0\nu\beta\beta$ Searches

The fundamental detection strategy for neutrinoless double beta decay is to measure the energies of the two outgoing electrons. Aside from a negligible recoil of the daughter nucleus, energy conservation requires that the full decay Q-value appear in the summed electron energies. In contrast, the two-neutrino double beta decay ($2\nu\beta\beta$) produces a broad, continuous energy spectrum extending from zero up to $2\nu\beta\beta$, due to the undetected neutrinos carrying away variable amounts of energy. This distinction enables experimental separation of the two processes, as illustrated in the toy spectrum of Figure 1.2, where the $0\nu\beta\beta$ peak is exaggerated for clarity.

A successful $0\nu\beta\beta$ search requires a large mass of a suitable isotope, operation in an ultra-low background environment, and the capability to measure the summed energy of the

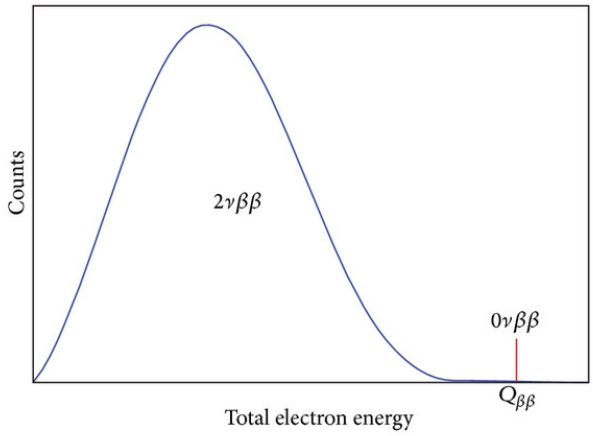

Figure 1.2: **Example Double Beta Decay Spectrum** Shown is the energy distribution of the two emitted electrons. The $2\nu\beta\beta$ spectrum is broad due to energy being carried away by the two neutrinos. The $0\nu\beta\beta$ peak at the endpoint has been exaggerated for visibility.

two emitted electrons over extended time periods, typically years. In an idealized search, the number of observed signal events at $E = Q_{\beta\beta}$ directly relates to the half-life via:

$$T_{1/2} = \ln_2 \times \frac{T N_{iso}}{N_{0\nu}} \tag{1.12}$$

where T is the experiment exposure time, N_{iso} is the number of isotope nuclei, and $N_{0\nu}$ is the signal count. In practice, however, experiments define a finite region of interest (ROI) around $Q_{\beta\beta}$, with width Δ determined by the detector's energy resolution σ_E and the expected background rate B. The ROI is optimized to maximize signal sensitivity while suppressing backgrounds, including both environmental radiation and the tail of the $2\nu\beta\beta$ spectrum. Additional limiting factors include the detection efficiency η, which accounts for energy threshold effects, dead time, and other inefficiencies. A commonly used approximation for the experimental sensitivity to the $0\nu\beta\beta$ half-life at 68% confidence level is:

$$F_{1/2} \propto \eta \sqrt{\frac{MT}{B\Delta_{\text{ROI}}}} \quad \text{(background-limited)} \tag{1.13}$$

$$F_{1/2} \propto \eta MT \quad \text{(background-free)} \tag{1.14}$$

where M is the isotope mass, T is the measurement time, and Δ_{ROI} is the width of the energy window. These expressions highlight the key requirements for a sensitive $0\nu\beta\beta$ experiment:

large exposure, excellent energy resolution, low background, and high detection efficiency [4, 39].

The experimental program for its search spans many isotopes and detector technologies and spectroscopy techniques. These techniques involve the detection of the following energy signals:

- **Ionization**: The measurement of charge carriers generated as the decay products ionize the detector medium. For example, the two emitted electrons produce ionization tracks whose charge, electron–hole pairs in semiconductors or free electrons in gaseous Time Projection Chambers (TPC), is collected to measure the deposited energy. Examples include Ref. [11, 12, 14, 40, 41]. A more detailed discussion of ionization discussion can be found in Chapter 2.

- **Scintillation**: The detection of light produced when decay products excite the detector material, which then de-excites by emitting photons. The light is typically readout using photomultiplier tubes or Silicon Photomultipliers (SiPM). Scintillation allows for easy scalibility to large detector volumes, as seen in KamLAND-Zen and SNO+ [16,37]

- **Bolometry** The detection of tiny temperature changes in a cryogenically cooled absorber resulting from energy deposition by decay particles. This technique provides excellent energy resolution and is employed in experiments such as CUORE and CUPID [42, 43].

Some experiments even involve the detection of multiple signals simultaneously—such as ionization and scintillation in EXO, or heat and light in CUPID-Mo to enhance event identification and background rejection. This multi-modal approach allows for powerful discrimination between double beta events and common backgrounds such as alpha or gamma interactions [41, 44].

To date, there has been no observation of $0\nu\beta\beta$. For ^{76}Ge, the combined GERDA, Majorana demonstrator and LEGEND-200 experiments have achieved a half-life sensitivity beyond 1.9×10^{26} years at 90% C.L., translating to an upper limit on $\langle m_{\beta\beta} \rangle$ in the range of 75–200 meV [45]. For ^{130}Te, the CUORE experiment has achieved a half-life limit of 2.2×10^{25} years, yielding $\langle m_{\beta\beta} \rangle \lesssim$ 75–350 meV [43]. For ^{82}Se, CUPID-0 placed a limit of $> 4.6 \times 10^{24}$ yr, corresponding to $\langle m_{\beta\beta} \rangle \lesssim$ 263–545 meV [38]. In ^{136}Xe, KamLAND-Zen has placed a half-life limit of 3.8×10^{26} years, corresponding to $\langle m_{\beta\beta} \rangle <$ 28–122 meV [46]. The results for ^{82}Se and ^{136}Xe are plotted on the lobster plot in Figure 1.1. The spread in these limits reflects the theoretical uncertainty in nuclear matrix elements, which complicates direct comparisons across isotopes.

Future ton-scale experiments such as LEGEND-1000, nEXO, and CUPID aim to reach sensitivities to $\langle m_{\beta\beta} \rangle$ below 20 meV [11, 14, 42], potentially covering the entire inverted neutrino mass ordering. This work presents a new detector concept capable of probing $m_{\beta\beta}$ to such a degree but relying on a fundamentally different, high-resolution imaging technology. Its projected discovery limit is shown in Figure 1.1. The absence of a discovery at this scale would strongly disfavor Majorana neutrinos in the inverted ordering scenario and push the search deeper into the normal ordering regime, requiring even lower backgrounds, improved energy resolution, and larger experiments. Its discovery, on the other hand, would have profound implications for the Standard Model, probing some of its biggest questions.

Chapter 2

THE SELENA NEUTRINO EXPERIMENT

The Selena Neutrino Experiment proposes to search for $0\nu\beta\beta$ in ^{82}Se, using enriched amorphous selenium (aSe) coupled to Complimentary Metal Oxide Semiconductor (CMOS) pixel detectors [47]. The high $Q_{\beta\beta}$ of ^{82}Seand the image-based event classification allow for a $0\nu\beta\beta$ decay search free of environmental backgrounds. The current program for Selena focuses on the R&D of the aSe/CMOS detectors, which builds upon existing technologies. This chapter will provide an overview of the proposed experiment, the detector technology and the scientific program of the Selena experiment.

2.1 Detector Concept

The proposed Selena detector is shown in Figure 2.1 and will be composed of stacked individual detector modules. Each module features $\sim$ 5 mm of aSe, enriched in ^{82}Se, deposited onto a 300 mm diameter wafer containing CMOS pixel arrays. This results in $\sim$ 2 kg of selenium. Each array covers a 2.5 $\times$ 2.5 cm^2 area and consists of hexagonal pixels with a 10-15 μm pitch. High voltage (HV) is applied via a thin gold electrode deposited over the top of the aSe. In the stack of detector modules, two modules share a common high-voltage electrode by arranging them such that the electrode sides of both modules face the same internal gap. Mechanical support is provided by a supporting frame, and electrical I/O by low-radioactivity flex PCBs connected to the arrays by Through Silicon Vias (TSV).

The detector scheme is chosen as such in order to maximize the topological reconstruction and identification of double beta decay within a detector module. In the event of ^{82}Se $\beta\beta$, two β particles are ejected from the nucleus. As they travel through the aSe bulk, they ionize electron hole pairs from the Se atoms. The low mass and charge of the β results in a long

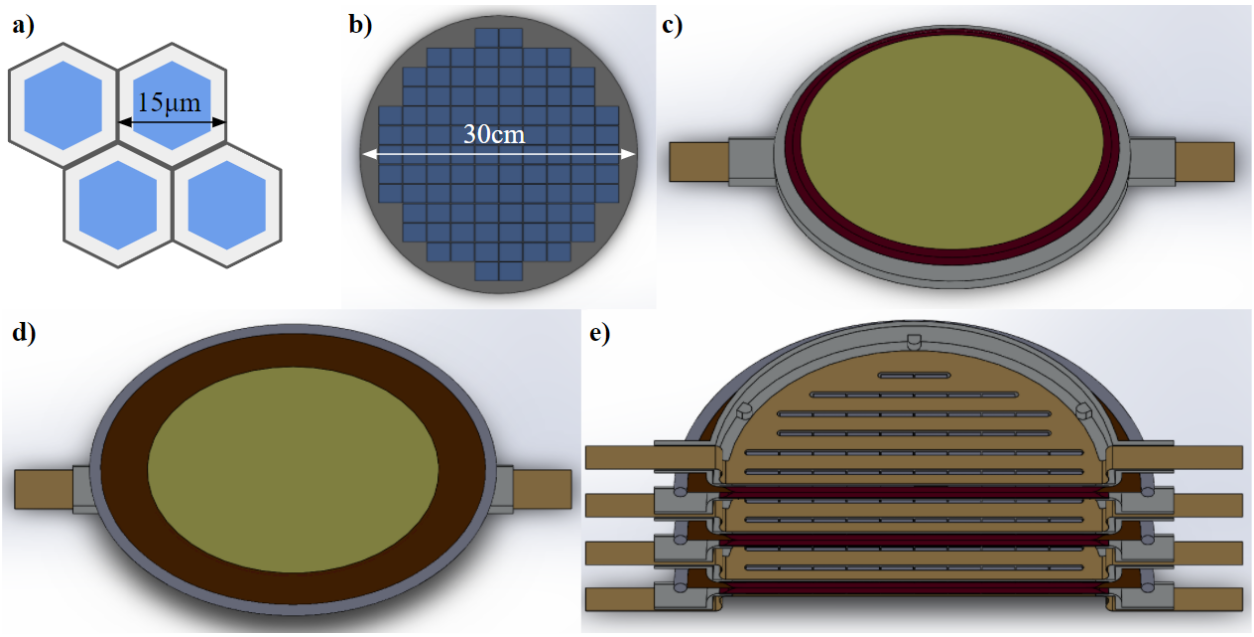

Figure 2.1: **Selena Detector Concept** (a) Hexagonal pixel array with 15 μm pitch. (b) Top view of the full sensor array spanning 300-mm, where blue indicate CMOS pixel arrays. (c) Single module comprising an aSe layer (dark red) with a gold electrode, deposited on the wafer surface in (b), and supported by a structural frame (light gray) and flexible PCB (khaki).(d) High-voltage (HV) ring installed above the module; the brown is conductive Kapton, and the surrounding gray ring provides mechanical stiffness and a rounded edge. (e) Cross-section of a stacked assembly of three module pairs. Cutouts in the flexible PCBs provide access for TSV connections.

track with frequent scatters as it interacts with the Se atoms. In a highly pixelated detector, this appears as a worm-like track. Under HV, ionized charge from these tracks will drift towards our pixel array, where we can sense, amplify and readout images of the $\beta\beta$ event. Figure 2.2 shows a simulated example of such an event. The capabilities and implications of this imaging technique will be explored in the following sections.

2.2 Amorphous Selenium as a Radiation Detector

Amorphous selenium (aSe) is commonly used in the medical imaging industry as an ionization target for digital radiography systems [48–50]. Unlike crystalline semiconductors, aSe lacks long-range atomic order, which allows it to be easily deposited uniformly over large areas. Its high photoconductivity and wide bandgap ($\sim$2.3 eV) make it suitable for detecting ionizing radiation at room temperature, as the wide bandgap suppresses thermally generated dark current and enables low-noise operation.

Typically, aSe is thermally evaporated between two electrodes to form a photoconductive layer ranging from 150 to several hundred microns in thickness. When exposed to ionizing radiation, energy is deposited in the material, liberating bound electron-hole pairs. This occurs primarily through Coulomb interactions with charged particles. The average energy required to generate a single electron-hole pair, denoted $W_{ehp}(\vec{E})$ and is field dependent.

Recombination plays an important role in determining the number of surviving charge carriers. Recombination occurs when an electron fills a hole—either its original partner (geminate recombination) or a separate carrier along the ionization track (columnar recombination). Because carrier densities are high immediately after ionization, a significant fraction of recombination occurs before the applied electric field separates electrons and holes. In disordered materials like aSe, recombination is modeled as a stochastic process characterized by a length scale r_0 [51]. Recombination reduces the number of carriers available for drift and effectively increases the work function W_{ehp}, degrading the signal-to-noise ratio. Under an applied electric field, the charge carriers drift toward the collection electrodes, inducing a signal that can be integrated and digitized.

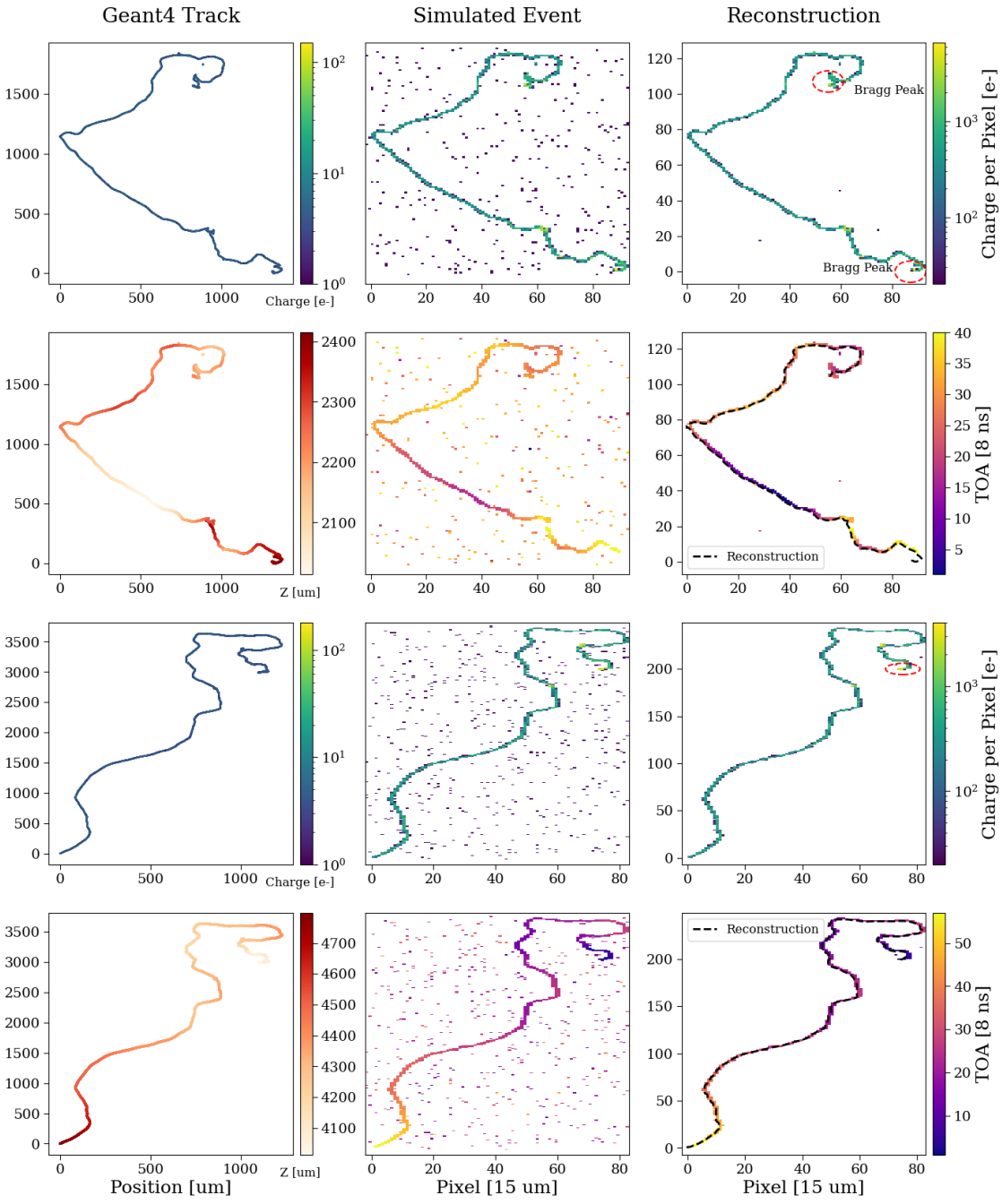

Figure 2.2: **Simulated $0\nu\beta\beta$ Tracks inside the Selena Detector** The left column shows the event generated in `Geant4`. The middle column shows the same event simulated in the Selena detector with 15 μm pixels, 10 ENC noise, and a hole lifetime of 100 μs. The right column shows the application of a noise mask. Each row displays both the pixel charge and the corresponding z-position of each pixel hit, illustrating the 3D topology of the event. The total event energy is 3 MeV under a bias field of 50 V/μm.

Once separated by the electric field, electrons and holes drift toward the anode and cathode, respectively, with velocities:

$$\vec{v}_{\text{carrier}} = \mu_{\text{carrier}} \vec{E} \tag{2.1}$$

where μ is the carrier mobility and $\vec{E}$ is the electric field. During their drift, charge carriers may undergo trapping, due to immobilization by defects in the disordered structure. It is characterized by the trapping time τ_t. Signal loss due to trapping can be modeled using the Hecht equation [10]:

$$\frac{Q}{Q_0} = \frac{\mu\tau V}{d^2}\left(1 - e^{-d^2/(\mu\tau V)}\right) \tag{2.2}$$

where d is the depth of interaction (DOI), V is the applied bias, and $\mu\tau$ is the mobility-lifetime product.

Charge carriers in aSe also undergo spatial diffusion as they drift. Diffusion causes the initial charge cloud to spread laterally. The diffusion coefficient is given by the Einstein relation [52]:

$$D = \mu \cdot \frac{kT}{q} \tag{2.3}$$

where μ is the carrier mobility, and kT/q is the thermal voltage. The lateral spread of the charge cloud (RMS width in the x-y plane) is given by:

$$\sigma_{xy}(z_{\text{DOI}}) = \sqrt{2 \cdot \frac{kT}{qE} \cdot z_{\text{DOI}}} \tag{2.4}$$

where z_{DOI} is the depth of interaction, and E is the applied electric field. In aSe, σ_{xy} is small due to the fields typically applied, enabling high spatial resolution and strong per-pixel SNR.

Although gamma rays and X-rays are uncharged, they can still generate ionization in aSe through secondary electrons produced via photoabsorption, Compton scattering, or pair production [10]. At low to moderate energies, photoabsorption is the dominant interaction. In this process, the incident photon is fully absorbed, transferring its energy to a bound

electron. If the photon energy E_γ exceeds the binding energy E_b, the electron is ejected as a photoelectron with kinetic energy:

$$E_K = E_\gamma - E_b \tag{2.5}$$

The remaining binding energy is released as the atom relaxes, typically through the emission of an Auger electron or characteristic X-ray, both of which can produce further ionization within the material. The photoelectron then ionizes additional electron-hole pairs via Coulomb interactions. In Compton scattering, the photon undergoes inelastic scattering with an electron, transferring only part of its energy. The resulting electron can ionize further charge, while the scattered photon may continue interacting via further Compton scattering or photoabsorption. At higher energies ($E_\gamma \gtrsim 1$ MeV), pair production can occur:

$$\gamma + Z \rightarrow e^- + e^+ + Z \tag{2.6}$$

$$E_\gamma = E_{e^-} + E_{e^+} \tag{2.7}$$

Here, the photon energy is converted into an electron-positron pair, and a nucleus must be present to absorb the recoil momentum. The likelihood of each interaction depends on the energy-dependent interaction cross sections of selenium, available in Ref. [53].

Other interaction mechanisms are also relevant in aSe. Direct excitation without ionization may occur, but the resulting emission of heat or photons is generally too weak for signal detection [10]. At high electric fields ($\gtrsim 70$ V/μm), impact ionization can occur, in which drifting charge carriers gain enough energy to create secondary electron-hole pairs—known as avalanche multiplication. Although challenging to implement due to the high field requirements, this process has found both scientific and commercial applications [54, 55]. Another interaction relevant for Selena is the generation of delta rays: secondary electrons emitted through inelastic scattering with a primary ionizing particle [10]. These delta electrons create additional ionization along their tracks, resulting in branching track topologies.

Charge	Mobility [μm^2/V$\cdot\mu$s]	Lifetime [μs]	Max Drift Time [μs]
Hole	37	10-40	O(1) us
Electron	1	20	O(10) us

Table 2.1: **aSe Ionization Properties** taken at a field 50 V/μm [51, 57]. Uncertainty in hole lifetime comes from sample composition and was not measured in Ref. [51]. Drift times are calculated for mm-scale thick detectors.

2.2.1 Single Pixel Detector

The specific properties of aSe were characterized in a prior Selena experiment focused on evaluating its suitability for ionization-based charge detection [51]. In this study, a 200 μm thick aSe layer was thermally evaporated by Hologic Inc in between two planar electrodes to create a *single pixel device*. The cathode is instrumented with a charge sensitive amplifier, shaping electronics and a digitizer. The authors investigated the ionization response to 122 keV gamma rays under applied electric fields from 10 to 50 V/μm. Table 2.1 shows the hole and electron transport properties for both 10 and 50 V/μm. With the flat-electrode geometry, the single-pixel detector is sensitive to charge motion from both electrons and holes. However, because holes exhibit significantly higher mobility and longer lifetime than electrons, their contribution dominates the induced signal: holes traverse the detector more quickly, suffer less trapping, and therefore produce a larger and faster current pulse. As a result, maximizing the signal-to-noise ratio requires dominant collection of the more mobile holes, known as unipolar charge sensing [56].

The principle of uniform charge sensing in aSe can be described through the formalism of the weighting potential and the Shockley-Ramo theorem [58,59]. According to this formalism, the current induced on a given sensing electrode by a moving charge is determined by a geometric quantity known as the weighting potential. For a charge q moving along a path from $\vec{x_1}$ to $\vec{x_2}$, the induced charge on the sensing electrode is:

$$Q = q\left(\Phi_w((\vec{x_2}) - \Phi_w\left(\vec{x_1}\right)\right) \tag{2.8}$$

where Φ_w is the weighting potential calculated by solving Laplace's equation after setting the sensing electrode to 1 and all other electrodes to potential 0. An important distinction is that the electric field $\vec{E}$ governs the charge carrier drift, while the weighting potential and field govern the signal induced. For a parallel plate geometry like that of the single pixel device, the weighting potential scales linearly with the distance to the sensing electrode: $\Phi_w \propto z$. The result is that the charge induced is a combination of both charge carriers in proportion to their drift in the direction of the weighting field. To achieve unipolar sensing, we employ a pixelated electrodes. In highly pixelated geometries where the pixel pitch a is much smaller than the detector thickness d ($a/d \lessapprox 0.1$), the weighting potential is flat for most of the detector but rises very sharply near the pixel, known as the *small pixel effect* [60]. This means that the majority of the induced signal occurs only when the charge carrier drifts close the electrode, ideal for high spatial resolution and low noise aSe detectors.

Ref. [51] also investigated the intrinsic energy resolution of aSe. By implementing a detailed microphysics model in `Geant4`, the study concluded that the energy resolution of aSe was dominated by recombination of charge carriers. Typically, the fundamental limit on energy resolution noise in photoconductors like aSe is governed by Fano noise [10]. However, in aSe there is an additional broadening of the spectrum as a result of charge carrier recombination correlated to the localized charge density. The measured relative energy resolution for a field of 50 V/μm was 6% RMS at 122 keV, which was recreated in simulation. The models in `Geant4` allow for detailed simulations of energy depositions in aSe. The implications of the energy resolution of aSe will be discussed in section 2.8.

2.3 CMOS Pixel Arrays

CMOS, *Complimentary Metal Oxide Semiconductor*, refers to a semiconductor fabrication process that enables highly integrated analog and digital circuitry on a single chip, or application specific integrated circuit (ASIC). This is achieved through the use of complementary pairs of p-type and n-type MOSFETs (Metal-Oxide-Semiconductor Field-Effect Transistors). It is the predominant technology in the semiconductor industry due to its low power consump-

tion, high integration capability, small feature size and cost-effectiveness in mass production, particularly when it comes to pixelated sensors [61]. The dominance of CMOS image sensors in smartphones, webcams and other digital cameras reflects this fact.

Beyond consumer electronics, CMOS pixels have found increasing application in physics instrumentation. Their ability to integrate charge collection, amplification, signal shaping, and digitization within each pixel enables high-resolution and scalable detectors. Applications include particle tracking in high-energy physics experiments, X-ray imaging in synchrotron facilities, and radiation monitoring in space-based instruments. Additionally, the maturity of commercial CMOS processes and infrastructure allows for rapid prototyping.

Several CMOS-based sensor architectures have been developed for use in physics instrumentation. A monolithic structure integrates both the sensing diode and readout electronics within the same silicon substrate. Examples include DEPFET (depleted p-channel field effect transistors) and Monolithic Active Pixel Sensors (MAPS), famously deployed in LHC experiments such as ALICE [62]. Hybrid pixel sensors, by contrast, consist of separate sensor and readout ASIC layers, which are fabricated separately and then bonded together. This architecture allows the independent optimization of the sensor for charge collection and the ASIC for readout processing. Examples include the Timepix and Medipix series, where pixels implement time-over-threshold (TOT) and/or time-of-arrival (TOA) measurements with digital readout [63].

To achieve the required performance, the Selena CMOS pixels are designed with an Equivalent Noise Charge (ENC) of 10–15 e^-, and a pixel pitch of 10–15μm to ensure high spatial resolution. For full 3D spatial reconstruction, each pixel incorporates a time-of-arrival (TOA) circuit with a timing resolution of 8 ns, enabling determination of the depth (z-position) of energy deposition based on drift time and track diffusion. The design also incorporates in-pixel analog-to-digital converters (ADCs) and time-to-digital converters (TDCs) to digitize charge and timing information locally, reducing analog signal routing and improving pixel scalability.

We envision the Selena pixel arrays to contain $\sim 10^6$ pixels, covering an an area $O(1)$

Design	Timepix4	Medipix4	Topmetal-II$^-$	TopmetalSe-V1	Proposed
Readout	Digital	Digital	Digital, Analog	Analog	Digital
Pixel Pitch [μm]	55	75/150	83	15	10-15
Array Size [mm^2]	24.7×30	24.1×25.6	6×6	1.5×1.5	25×25
TOA	200 ps	N/A	N/A	N/A	$\sim$8 ns
ENC [e$^-$]	60-80	68-178	10-15	26	10
Static Power [mW/cm^2]	< 400	< 500	< 100	~ 400	$O(100)$
Process node[nm]	65	130	350	130	TBD

Table 2.2: **Performance Comparison of Hybrid Pixel Arrays** [63–65]

cm^2. To preserve imaging uniformity and maximize the active area, these arrays must be stitched or abutted on a standard 300 mm wafer with minimal dead regions between them. This is critical, as increasing array size through simply scaling up pixel count is often limited by readout speed and complexity. However, given the extremely low expected event rate for $0\nu\beta\beta$, data throughput requirements are modest, allowing the readout architecture to prioritize low power and noise rather than speed.

To remain viable for large-area deployment, the static power consumption per pixel must be limited below a μW. This constraint arises from the need to limit the total power density on the sensor plane to less than a few hundred mW/cm^2 to avoid introducing local heating [64], which could degrade charge transport in amorphous selenium and require active thermal management. Table 2.2 shows the Selena requirements in comparison to existing hybrid pixel technologies, illustrating that the described detector performance is achievable using currently available or near-term CMOS technology.

2.4 aSe/CMOS Hybridized Detectors

Traditionally, commercial aSe x-ray imagers utilize thin-film transistor (TFT) arrays as the readout ciruitry. While suitable for medical imaging applications, TFT-based systems are limited in both spatial resolution (typically on the order of 100 μm) and noise performance (around 1000 e^-RMS), making them inadequate for rare-event searches like Selena.

To address the limitations of TFT-based aSe imagers, several research efforts have explored the development of hybrid aSe/CMOS pixel arrays [48]. These efforts have primarily targeted digital radiography, aiming to improve image quality, reduce patient dose, and enable real-time imaging. As reported in Ref. [48], typical RMS noise levels for these CMOS arrays remain in the hundreds of electrons, largely due to the use of simple 3-transistor (3T) or 4-transistor (4T) pixel architectures. These designs are compact but inherently noisy, and are not optimized for applications requiring low ENC. In contrast, the pixel designs summarized in Table 2.2 employ more complex front-end architectures to improve noise performance.

Notable recent developments include pixel sizes as small as 5.6×6.25μm with total RMS noise of 350 e^-, including a 90 e^- RMS electronics noise floor [66]. Similarly, Ref. [67] demonstrated a 1-megapixel detector with a 100 μm thick aSe layer, 7.8×7.8 μm pixels and a total pixel noise of 180 e^-. While these designs represent significant progress in spatial resolution, demonstrating the *single pixel effect*, and are promising for photon-counting X-ray imaging, they have not been employed in the context of nuclear decay spectroscopy or particle track reconstruction—capabilities essential for Selena.

2.5 Selena Detector Simulation

We simulate the Selena detector to evaluate its performance and demonstrate its capabilities. The model consists of a 5 mm thick aSe layer coupled to a 100 μm thick CMOS substrate, with an applied electric field of 50 V/μm. Ionization events in aSe are modeled using `Geant4`, which provides a step-by-step spatial distribution of deposited charge along the particle track.

Typical step size is between 400 and a few thousand nm. Recombination is incorporated using the model from Refs. [51, 68]:

$$w_{\text{ehp}} = w_0 \left(1 + \frac{E_k \alpha}{8\pi r_0^2 w_0 E_b \mu(\vec{E})} \right) \tag{2.9}$$

Here, w_{ehp} is the effective energy required to produce an electron-hole pair, w_0 is the intrinsic pair creation energy, E_k is the deposited kinetic energy in each step, r_0 is the characteristic recombination length scale, $\mu(E)$ is the field-dependent mobility, E_b is the binding energy, and α is a material-dependent constant. In practice, the model increases w_{ehp} in regions of dense ionization and the deposited energy is converted into a number of surviving charge carriers. This model has been experimentally validated in Ref. [51].

After the initial charge deposition from `Geant4`, we simulate charge transport by modeling diffusion and charge trapping. We apply lateral diffusion as a Gaussian spread using Eq. 2.4, based on the depth z of each charge cluster. Throughout the detector, the lateral diffusion σ_{xy} varies from 0 to approximately 3 μm, leading to a measurable broadening of tracks depending on their interaction depth. The z depth is also used to calculate the charge collection efficiency as a result of charge trapping, modeled by Eq. 2.2. Since the hole lifetime is sample dependent, we choose a conservative value of $\tau = 100$ μs.

To model the induced signal on the pixels, we simulate the weighting potential for the pixel geometry using a single `COMSOL` simulation under the Shockley–Ramo framework. This calculation is performed once to verify the presence of the *small-pixel effect*, as illustrated in Fig. 2.3, rather than repeated for every simulated event. The confirmation of this effect justifies the approximation that each pixel operates as an independent sensor of the local charge. In the subsequent analysis, we assume that each pixel collects 100% of charge carriers within its immediate vicinity. Under this approximation, the measured signal directly corresponds to the collected charge, the pixel pitch defines the spatial (x–y) resolution, and the TDC resolution sets the precision of the reconstructed charge arrival time.

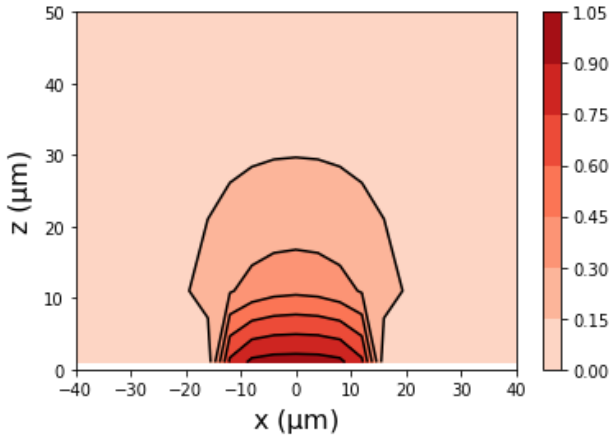

Figure 2.3: **Weighting Potential of Selena Pixel** Simulated 2D cross-section of the weighting potential in an example Selena pixel geometry (20 μm pixel pitch). The bias electrode is placed at $z = 500$ μm and is not shown. The highly localized contour near the pixel surface demonstrates the small pixel effect, where only charge carriers near the collection node contribute significantly to the induced signal.

2.6 Intrinsic Energy Resolution

The intrinsic energy resolution of amorphous Selenium informs the detector geometry. Ref. [69] extrapolated their measured energy resolution to 1.1% RMS at the Q-value. To demonstrate this capability in a pixelated detector, they simulated 3 MeV $\beta\beta$ tracks within aSe for 15 μm pixels in 200 μm thick aSe. They demonstrated that the 1.1% RMS can be achieved by taking into account both the total charge and the track length in pixels.

We extend the work presented in Ref. [69] by simulating high energy β and $\beta\beta$ tracks within a 5 mm thick aSe layer, which allows for full containment of tracks. For this, we ignore the effects of trapping, diffusion and readout noise. Each individual track is subdivided into 15 μm side voxels by starting at a seed point at one end of the track, and summing up all the charge and energy depositions within a 7.5 μm in any dimension, then continuing to subdivide the track. For each voxel, we record the energy deposited and ionized charge in aSe. We construct a histogram of energy deposited vs ionized charge per 15 μm^3 voxel. We define a charge conversion function $e_{\text{sim}}(q)$ by taking the profile, averaging each x-slice. For

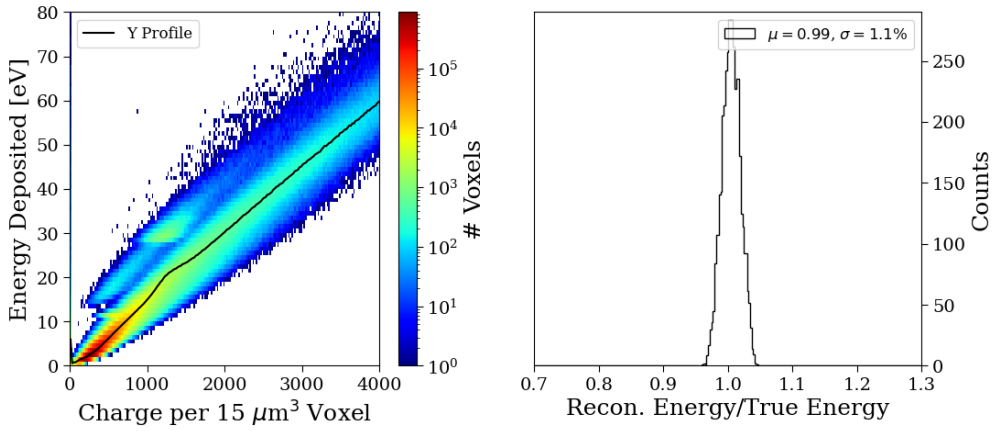

Figure 2.4: **Simulated Energy Reconstruction** Left: Calibration data and curve showing 2D histogram and profile of the average deposited energy versus ionized charge per 15 μm^3 voxel, used to derive a voxel-level energy estimator. Right: Distribution of reconstructed energy normalized to true energy for 3 MeV $\beta\beta$ tracks, yielding a resolution of 1.1% RMS.

a track, its reconstruction energy is then computed as:

$$E = \sum_i e_{\text{sim}}(q_i) \quad \text{over each 15 x 15 x 15 } \mu\text{m voxel} \tag{2.10}$$

Figure 2.4 shows $e_{\text{sim}}(q)$ and histogram of the reconstructed energies, demonstrating a resolution of 1.1% RMS. This demonstrates an additional energy reconstruction method to Ref. [69], allowing a measurement dependent on the local charge density in a predefined volume.

We also explore additional voxel geometries. Listed in Figure 2.3 is additional voxel geometries, which demonstrate that we can achieve the best resolution with a 15 μm voxel geometry. The lack of improvement at finer voxel dimensions is understood as a consequence of the recombination model. Because the number of carriers lost to recombination is no longer averaged over a sufficiently large volume, the variance of the surviving charge fraction grows as the voxel size shrinks. As a result we identify an ideal pixel sensitivity volume to be $15 \times 15 \times 15$ μm^3 for this geometry.

Voxel Dimensions	**RMS Resolution**
$15 \times 15 \times 15$ μm^3	1.1%
$10 \times 10 \times 10$ μm^3	1.2%
$10 \times 10 \times 37$ μm^3	1.5%
$30 \times 30 \times 30$ μm^3	1.3%

Table 2.3: **Voxel-segmented track reconstruction energy resolutions at $Q_{\beta\beta}$.**

2.7 Simulated Events in Selena

Each pixel in the simulated detector corresponds to a 15 μm pitch, with an equivalent noise charge (ENC) of 10 e$^-$ and a time-of-arrival (TOA) resolution of 8 ns, defining an effective voxel size of 15 μm in all dimensions. Tracks generated in `Geant4` are discretized into this pixel grid, after which electronic noise is applied independently to each pixel. The true z positions of energy depositions are converted to drift times according to the charge transport depth in aSe and then binned into 8 ns intervals. To emulate the fact that only relative z positions are measurable, the minimum drift time z_0 is subtracted from each event. This procedure yields simulated events with full four-dimensional tracking information (x, y, t, c), where c denotes the deposited charge. Example simulated double-beta events are shown in Fig. 2.2.

To suppress both noise and data volume, pixels with signals below 2σ of the noise level are removed. In addition, a spatial noise-masking algorithm was developed to further reject isolated electronic fluctuations. For each pixel, the algorithm evaluates its local charge environment in the x–y plane to determine whether it belongs to a contiguous cluster of charge depositions or represents an isolated noise hit. Pixels with charge amplitudes exceeding 5σ are automatically retained as valid hits. For all remaining pixels, the squared distance to all other pixels in the event is computed. For a given pixel, the number of neighboring pixels within a radius r_{th}^2 (excluding the pixel itself) is then counted; if this number falls below a minimum-neighbor threshold, the pixel is flagged as noise and excluded from further re-

construction. The effects of this noise filter before and after application are illustrated in Fig. 2.2.

2.7.1 Topology Reconstruction

To reconstruct the topology of ionization tracks, we employ a label-based connected-component algorithm inspired by breadth-first search (BFS) segmentation methods [70]. The function iteratively propagates through clusters of pixels. Beginning from a seed pixel (label 0), the algorithm identifies all neighboring pixels within a fixed spatial radius in the x–y plane ($r < 2$) and within a time-of-arrival difference threshold ($|\Delta z_{\mathrm{TOA}}| < 3$). These neighboring pixels are assigned the next integer label $(1, 2, \dots)$, effectively mapping the charge cloud outward layer by layer along the track. If no additional pixels satisfy the distance and timing constraints, the algorithm initiates a new seed from the nearest unlabeled pixel, allowing multiple disconnected clusters to be labeled independently.

For each label, the algorithm computes the charge-weighted mean variance of the pixel coordinates in x and y. The mean acts to trace the particle track, while the variance quantifies the local spread of charge, which is used to detect branching behavior—large increases in label-to-label variance ($\Delta\sigma^2 > 4$) indicate potential bifurcations. Pixels in these branching regions are remarked with offset labels (e.g. +1000) and reprocessed to preserve the connectivity. The result is an ordered labeling of pixels that traces the event's spatial development, providing a simplified skeleton of the charge topology in both lateral (x, y) and relative (z_{TOA}) dimensions.

The reconstruction of the absolute z-depth is more challenging. We use both the diffusion of the charge topology and the TOA to estimate depth. For a given pixel, the depth relative to the earliest charge arrival is:

$$z_{\mathrm{abs}} = z_0 + z_{\mathrm{rel}}(t) \tag{2.11}$$

$$z_{\mathrm{rel}}(t) = t\mu_h E \tag{2.12}$$

where μ_h is the hole mobility and E is the electric field. With a 8 ns TOA resolution,

the corresponding z resolution in z_{rel} is approximately 15 μm. However, since the absolute time of ionization is unknown, we cannot directly extract z_0 from TOA alone. We therefore develop a diffusion-based estimator for z_0. For the variance of charge groups with label j along the track, we calculate a pseudo-variance, so named because it incorporates the effects of coarse pixelation and overlapping charge clouds:

$$\tilde{\sigma}_j^2 \propto z_0 + z_{\text{rel}} \tag{2.13}$$

We thus use the distribution of $\tilde{\sigma}^2 - z_{\text{rel}}$ as the primary estimator for z_0. This estimator is calibrated using simulated data with known drift depths to construct a mapping between the observed distribution and true z_0.

Although this algorithm is still under development, we have explored various features of the distribution to optimize performance. For example, Fig. 2.5 shows an approach using the 30th percentile of the $\tilde{\sigma}^2 - z_{\text{rel}}$ distribution across known z_0 values. In this study, In this study, we simulate tracks at fixed drift depths, compute the corresponding 30th percentile values, and fit a mean profile curve to these points. Applying this estimator to an independent dataset yields a z_0 resolution of $\sim$1300 μm, defined as the standard deviation of the difference between true and reconstructed z_0.

Further improvements to the topology reconstruction are possible. When applied to simplified, straight-line "toy" tracks, the current method achieves a z_0 reconstruction resolution on the order of 500 μm, which likely represents an intrinsic performance limit of the present implementation. The current track-labeling algorithm could be refined to better handle branching regions, where complex and branching topologies often lead to ambiguous labeling and discontinuities in the reconstructed path. Alternative approaches, such as graph-based or density-based clustering methods, may offer a more robust treatment of complex, non-linear track geometries [71]. The z_0 reconstruction could also be enhanced by incorporating additional topological features, such as the local inclination of the track in z_{rel}, or independent treatment of high-energy-deposition regions (e.g. Bragg peaks), which have simple geometries and higher charge yield.

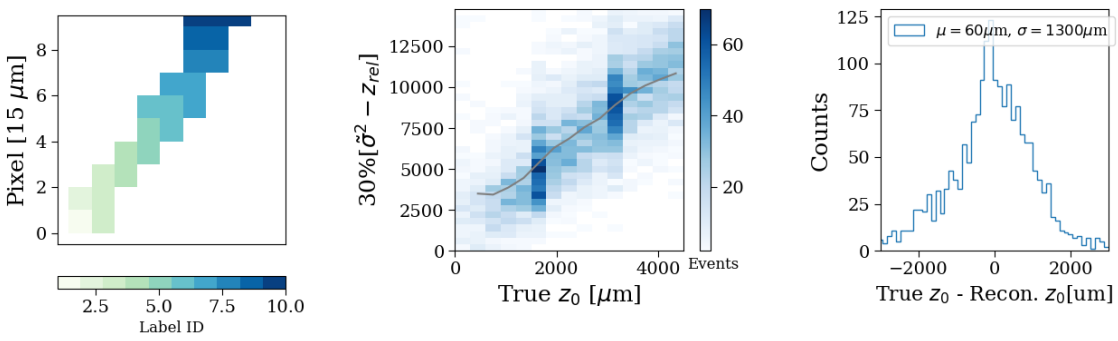

Figure 2.5: **Diffusion and z-Reconstruction in Selena** Left: Track labeling using connected components, where contiguous charge clusters are assigned a label j; the charge-weighted mean and pseudo-variance are computed for each label. Middle: Estimator construction based on the 30 percentile of the distribution of pseudo-variances across many simulated events. Right: Resolution of the estimator, defined as the standard deviation between reconstructed and true z_0.

2.7.2 Energy Reconstruction

Lastly, for a set of $0\nu\beta\beta$ events, we perform a full energy reconstruction to measure the resolution at the Q-value. We apply the voxel-based energy function $e_{\text{sim}}(q)$ to each pixel containing a charge deposition within an event (after noise masking). This function is evaluated under several detector configurations, beginning with an idealized case without charge drift diffusion, ENC noise, or trapping, and then progressively reintroducing these effects. For cases including trapping, we apply the z_0 reconstruction to estimate the charge loss and recover the total charge. The spectra for a selection of cases are shown in Fig. 2.6, and the resulting resolutions are listed in Table 2.4.

Approximately 7% of reconstructed tracks fall well below 5σ of the mean energy. These outliers arise from two main effects: about 5% correspond to events whose range extends beyond the detector volume, resulting in partial energy loss, while the remainder are cases where the track contains widely separated, spatially distant charge clusters. In such events, the noise-masking and reconstruction algorithms must operate over volumes that are currently too large to be processed, leading to failures of the reconstructed algorithm.

A significant contribution to the measured RMS energy resolution beyond the intrinsic

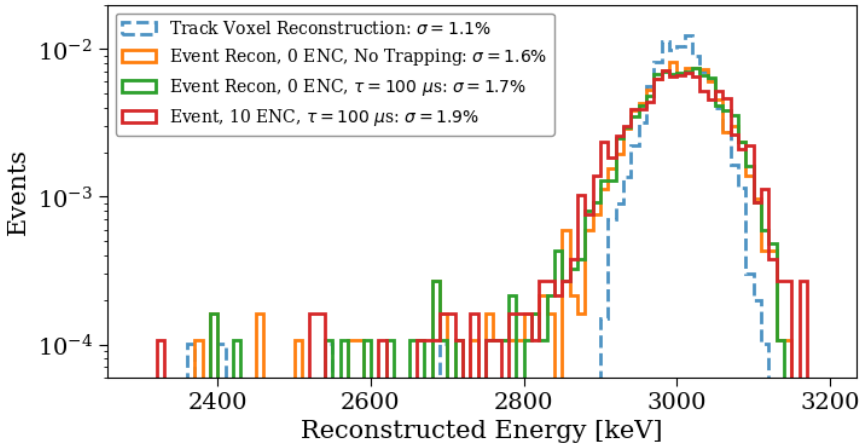

Figure 2.6: **Simulated Energy Spectra of $0\nu\beta\beta$ Events** for four different reconstruction scenarios. Blue-dashed shows the intrinsic energy resolution of aSe, recreated through a voxel-segmented track. Orange shows an idealized Selena limit, with no noise and exact charge collection. Green and Red introduce trapping and noise and are reconstructed with current techniques.

limit originates from the pixelation of the continuous charge track within the detector. When the continuous charge distribution is projected onto a fixed pixel grid, sub-pixel spatial information is lost, and charge sharing between neighboring pixels becomes discretized. In contrast, the study in Section 2.6 adapts cubic volumes centered on the true track geometry rather than on a global pixel lattice. By aligning the voxel sample volumes to the track itself, the study reduced the discretization noise.

This effect can be quantified by performing the same energy reconstruction under idealized conditions (0 ENC and no trapping) while varying the pixel grid alignment for a single event, which produces measurable variations in the reconstructed energy: $\sim 0.4\%$ RMS in for tracks with no noise and diffusion. Additionally, simulations using a 10 μm pixel pitch yield a correspondingly lower energy resolution under ideal conditions, since the finer segmentation reduces the degree of discretization noise. However, these smaller pixels ultimately exhibit a higher overall noise after full reconstruction because the larger number of pixels increases the total contribution of readout noise. Together, these studies provide direct evidence of quantization noise arising from the discrete spatial sampling of a continuous charge

Detector Case	**RMS Resolution**
0 ENC, No Trapping	1.6%
0 ENC, No Trapping, 10 μm pitch pixels	1.4%
0 ENC, $\tau = 40$ μs, No Z-recon	2.2%
0 ENC, $\tau = 100$ μs, No Z-recon	1.8%
0 ENC, $\tau = 400$ μs, No Z-recon	1.7%
0 ENC, $\tau = 40$ μs, Z-recon	1.8%
0 ENC, $\tau = 100$ μs, Z-recon	1.7%
0 ENC, $\tau = 400$ μs, Z-recon	1.7%
10 ENC, $\tau = 100$ μs, Z-recon	1.9%
10 ENC, $\tau = 100$ μs, $\Delta Z = 500$ μm	1.8%
10 ENC, $\tau = 400$ μs, Z-recon	1.9%
10 ENC, $\tau = 100$ μs, Z-Recon, 10 μm pitch pixels	2.1%

Table 2.4: **Selena Event-Level Reconstruction Results at $Q_{\beta\beta}$.** Unless otherwise specified, pixel pitch is 15 μm. Z-reconstruction is done via method described in 2.7.1, with a resolution of about 1300 μm. We also simulate a theoretical case where the z-resolution is improved to 500 μm.

distribution.

The effects of electronic noise and charge trapping further broaden the energy distribution, though their contributions are smaller than that of pixelation. The largest degradation in resolution thus arises from the fixed pixel grid itself. This highlights a potential limitation of pixel-based charge-density energy reconstruction: by enforcing a discrete sampling of the continuous track, pixels inevitably contain charge densities that deviate from the true local values.

A contrasting approach, described previously and in Ref. [69], combines measurements of the total collected charge (rather than per-pixel) and the total track length to recover the intrinsic energy resolution. Such a technique would be effective at removing the mentioned discretization noise, since it would remove per-pixel variations, thus allowing for 1.1% RMS

energy resolution. However, in our simulation, this technique no longer works since a simple count of hit pixels varies with charge diffusion and electronic noise. More advanced topology-reconstruction algorithms could enable more reliable estimates of the effective track length. Consequently, a robust reconstruction of the full track topology will be essential for improving the accuracy of energy reconstruction in the Selena detector.

2.8 Science Program

The primary science goal of Selena is the search for neutrinoless double beta decay. As shown in section 1.4, the $0\nu\beta\beta$ sensitivity is heavily dependent on both the energy resolution ΔE and the background index B. This section discusses their impact on Selena's search for $0\nu\beta\beta$, as well as its sensitivity for other science measurements.

2.8.1 Background Index

The most recent background study of Selena estimates an environmental background index in the ROI of 6×10^{-5} per (keV x ton x year) [72]. This level of background suppression can be achieved through careful material selection, deep underground operation with passive shielding, and advanced particle-identification and discrimination techniques.

To begin with, the ^{82}Se Q-value lies well above the dominant γ-ray backgrounds from natural radioactivity, such as those produced in the ^{238}U and ^{232}Th decay chains. In addition, the fine spatial and temporal resolution of the Selena detector enables detailed identification of event topologies and tagging of radioactive decay chains. As illustrated in Fig. 2.2, a true double-beta decay produces two Bragg peaks—localized regions of high energy deposition that occur as each electron slows down. This characteristic topology provides powerful discrimination against several background classes: external γ rays, which typically yield multi-site or single-site interactions through Compton scattering or photoelectric absorption; α particles, which deposit a dense, single-site charge cloud; and single β decays, which contain only one Bragg peak. Current reconstruction techniques achieve a signal acceptance of roughly 50% for double-beta events, while rejecting more than 99.9% of single-electron

topologies [69].

Although single β decays generally produce only one primary electron, δ rays generated along the track can produce a second energetic electron, yielding a topology that can mimic a double-beta event. High-energy γ rays can also produce $\beta\beta$-like signatures through several interaction channels. In the photoelectric effect, the full γ energy is transferred to a photoelectron, but the subsequent emission of Auger electrons or characteristic X-rays can create additional localized ionization that resembles a multi-electron topology. Compton scattering can result in multiple spatially separated electron recoils when the γ ray undergoes successive scatters; the combined energy of these recoils can fall in the ROI and imitate a two-electron event. Finally, pair production from γ rays above ≈ 4 MeV produces an $e^- e^+$ pair emerging from a common vertex. If one or both 511 keV annihilation photons escape the detector, the visible energy can lie near $Q_{\beta\beta}$, yielding a double-beta–like signature.

The spatial-temporal capabilities of the detector can also be leveraged to identify long-lived radio-contaminants through decay-chain tagging, a technique used by the DAMIC collaboration [13]. An example from the DAMIC CCDs is in Figure 2.7, showing a spatially coincident sequence of two low-energy beta events separated by 4 days, followed by a high-energy alpha event 10 days later. This decay can be identified as the decay of ^{210}Pb ($T_{1/2} = 22$ yr, $Q = 60$ keV) to ^{210}Bi ($T_{1/2} = 5$ days, $Q = 1.1$ MeV) to ^{210}Po ($T_{1/2} = 138$ days, $Q = 5$ MeV), ending in the stable ^{206}Pb. The extremely low probability of a random sequence mimicking this timing and spatial signature enables confident identification and suppression using this technique. This technique can be extended in the Selena detector to tag and suppress a variety of contaminants which might leak into the ROI, such as the daughter isotopes of ^{238}U and ^{232}Th: ^{214}Bi and ^{208}Tl, respectively.

Mitigation of these backgrounds requires minimizing cosmogenic activation and neutron exposure of materials and employing low activation copper or alternative radiopure metals, such as electroformed or underground stored copper. The total backgrounds are listed in table 2.5, and the background spectrum is shown in Figure 2.8.

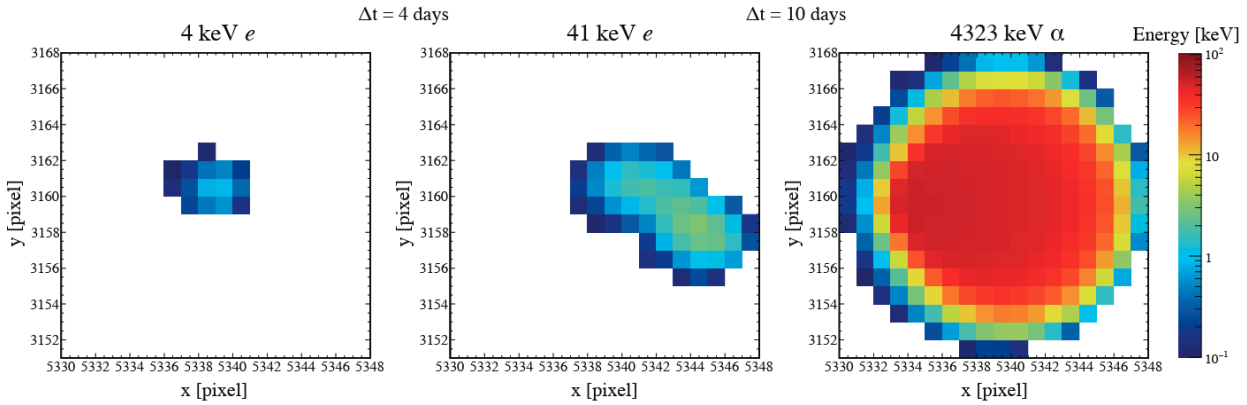

Figure 2.7: **DAMIC CCD Decay Chain Event** Identified to be the decay of radiocontaminant ^{210}Pb→^{210}Bi→^{210}Po→^{206}Pb.

Table 2.5: Estimated background rates and discrimination levels in the ROI for Selena [69]

Background Source	**Rate (keV ton yr)$^{-1}$**	**After disc.**
β-decay (Bulk)	5.8	6.4×10^{-8}
β-decay (Surface)	7.1	2.1×10^{-7}
β-decay (Cosmogenic)	1.7×10^{-3}	2.6×10^{-6}
γ-ray (Photoelectric)	1.3×10^{-2}	1.3×10^{-5}
γ-ray (Compton)	2.8×10^{-2}	7.1×10^{-6}
γ-ray (Pair production)	3.3×10^{-5}	3.3×10^{-6}
Total external backgrounds:		6×10^{-5} **(keV ton yr)$^{-1}$**

2.8.2 Discovery Limit

To estimate the detector's discovery sensitivity to $0\nu\beta\beta$, we performed a likelihood-based analysis using toy Monte Carlo (MC) simulations. The test statistic distribution was evaluated under both background-only and signal-plus-background hypotheses. By scanning over injected signal strengths, we identified the minimum number of signal events needed for a 3σ

discovery. Three detector-response scenarios were investigated: an aSe limit corresponding to the theoretical energy resolution (1.1% RMS), a Selena limit representing the geometry and an ideal pixel performance of the hybrid aSe/CMOS design (1.6% RMS, 7% event loss outside the ROI), and a full simulated reconstruction case using the measured response from prototype data (1.9% RMS with 7% event loss). In each case, we apply a 50% acceptance for $\beta\beta$ events, a result from Ref [69], and assume an exposure of 100 ton-years of ^{82}Se. The test statistic is defined as:

$$\Delta\text{LL} = -2\ln\left(\frac{\mathcal{L}(\text{data} \mid \text{background})}{\mathcal{L}(\text{data} \mid \text{signal} + \text{background})}\right) \tag{2.14}$$

$$\ln\mathcal{L}(n_i \mid \mu_i) = \sum_i \ln P(n_i \mid \mu_i) \tag{2.15}$$

$$P(n \mid \mu) = \frac{e^{-\mu}\mu^n}{n!} \tag{2.16}$$

where n_i and μ_i denote the observed and expected number of counts in bin i, respectively. The sum runs over the region of interest (ROI), typically taken to be 3.0–3.2 MeV to suppress the $2\nu\beta\beta$ background.

Background $2\nu\beta\beta$ event energies were generated using the `DECAY0` event generator [73], assuming a $2\nu\beta\beta$ half-life of 9.6×10^{19} years for ^{82}Se [74]. To model the detector response, the reconstructed spectra from Fig. 2.6 were converted into probability density functions (PDFs). Since only events near the Q-value were of interest, this approximation is sufficient. The resulting PDFs were convolved with the true $2\nu\beta\beta$ energy distributions to obtain the simulated background spectra.

We first generated background-only toy spectra and computed ΔLL values against varying signal-plus-background models. The resulting ΔLL distribution established the 3σ threshold under the null hypothesis, with $\Delta\text{LL}_{3\sigma} = 9$, consistent with Wilks' theorem [75]. Next, we repeated the process with toy spectra including varying $0\nu\beta\beta$ signal counts. For each signal strength, we evaluated how often ΔLL exceeded the 3σ threshold. From this, we determined the number of signal counts that yield a median 3σ discovery significance. For the three scenarios, we found that the theoretical aSe response had a discovery sensitivity

to 27 counts, a $0\nu\beta\beta$ half life of 9.6×10^{27} years, the idealized Selena limit had a sensitivity to 44 counts, a half life of 5.8×10^{27} years, and for a full detector simulation with current reconstruction techniques a sensitivity to 67 counts, a half life of 3.8×10^{27} years.

A projected $0\nu\beta\beta$ half-life sensitivity of (2.3×10^{27}–1×10^{28}) years positions Selena as a natural successor to the ton-scale experiments now entering operation. This sensitivity corresponds to an effective Majorana mass of $\langle m_{\beta\beta} \rangle \simeq$ 10–28 meV, covering the full inverted band. Achieving this level of sensitivity allows the experiment to test a broad class of neutrino mass models and lepton number–violating mechanisms, and may begin to probe regions favored by the minimal Type-I seesaw scenario. In addition, Selena's fine-grained tracking enables reconstruction of electron track topologies, providing sensitivity to kinematic and angular correlations that may help distinguish between different decay mechanisms in the event of a signal. If no signal is observed at this scale, it would strongly constrain the parameter space of Majorana neutrinos and push the discovery frontier into the normal ordering regime.

2.8.3 Additional Science

Under electron neutrino capture, ^{82}Se undergoes a unique triple-decay sequence leading to ^{82}Kr. The capture process, with a threshold energy of 172 keV, is described by:

$$^{82}\mathrm{Se} + \nu_e \rightarrow ^{82}\mathrm{Br} + e^- \tag{2.17}$$

This reaction, known as inverse beta decay, produces ^{82}Br in an excited 1^+ state, which subsequently decays to ^{82}Kr via the following chain:

$$^{82}\mathrm{Br}\ (1^+) \rightarrow\ ^{82}\mathrm{Br}\ (2^-) + \gamma \qquad \Delta E = 29\ \mathrm{keV}, \quad \tau_{1/2} = 7.2\ \mathrm{ns}$$

$$^{82}\mathrm{Br}\ (2^-) \rightarrow\ ^{82}\mathrm{Br}\ (5^-) + \gamma \qquad \Delta E = 46\ \mathrm{keV}, \quad \tau_{1/2} = 6.1\ \mathrm{min}$$

$$^{82}\mathrm{Br}\ (5^-) \rightarrow\ ^{82}\mathrm{Kr}\ (0^+) + \beta^- + \bar{\nu}_e \qquad \Delta E = 3093\ \mathrm{keV}, \quad \tau_{1/2} = 35.3\ \mathrm{h}$$

Due to the 7.2 ns half-life of the initial transition, the prompt signal, defined electron emitted in eq. 2.17, and the first decay will likely be indistinguishable in time. However, all three

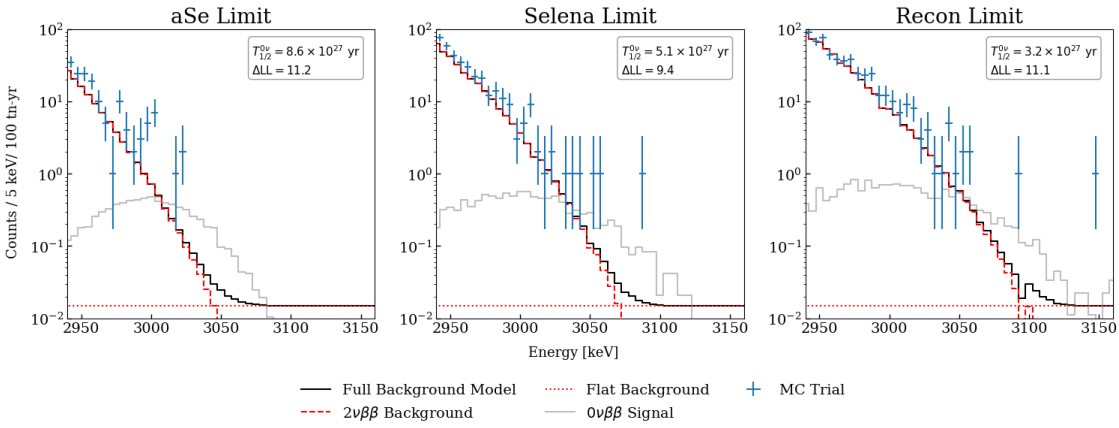

Figure 2.8: **Monte Carlo Trials** for a 100 ton-year exposure of Selena under three detector scenarios. The data points (blue) represent a single toy experiment drawn from the statistical fluctuation of the full background model (black) plus a signal (grey). The *aSe limit* corresponds to a detector with 1.1% RMS energy resolution; the *Selena limit* assumes an idealized detector response; and the *Recon limit* includes the current measured energy and event reconstruction performance. In all cases, the resulting test statistic ΔLL for each trial exceeds the 3σ discovery threshold, demonstrating the detector's sensitivity to the $0\nu\beta\beta$ signal region.

decays occur spatially coincident, producing a unique triple signature. A survey of decay sequences has found no known background processes that produce a similar spatially coincident decay sequence [72]. Thus, leveraging the spatial resolution of the detector allows Selena to perform essentially background-free ν_e spectroscopy with a 172 keV energy threshold.

By detection and measurement of initial prompt electron energy, which corresponds to the neutrino energy, we foresee two primary physics applications for this detection capability:

1. Solar Neutrino Spectroscopy As introduced in Chapter 1, the dominant source of solar neutrinos is the *pp* reaction:

$$p + p \rightarrow d + e^+ + \nu_e \qquad E_\nu \leq 0.42 \text{ MeV} \tag{2.18}$$

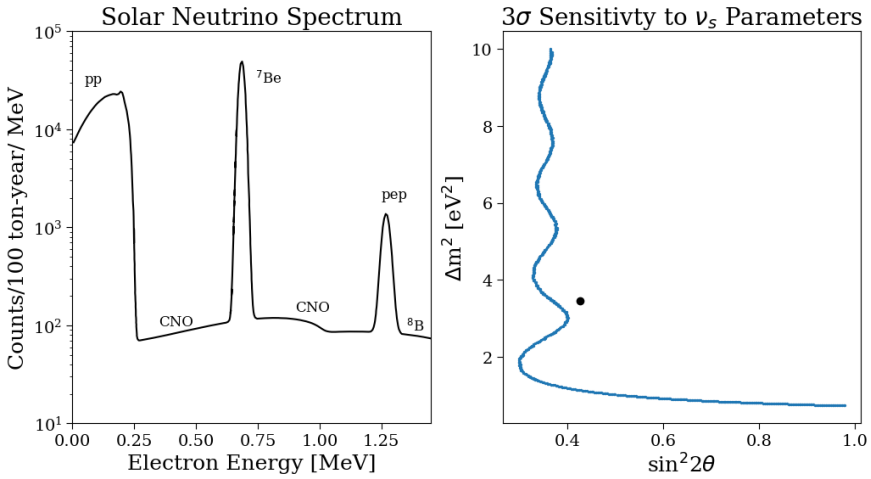

Figure 2.9: **Additional Science Results for Selena Detector** Left: Expected prompt-electron energy spectrum from solar neutrino interactions in a 100 ton-year exposure of the Selena detector, with neutrino species labeled. Right: Sterile neutrino sensitivity curve from electron neutrino captures with a ^{71}Ga source. Right of the blue curve represents the 3σ exclusion contour, and black denotes the best-fit sterile-neutrino parameters associated with the gallium anomaly [76, 77]

which accounts for approximately 91% of the solar neutrino flux. Additional components of the solar neutrino spectrum include:

$$e^- + \mathrm{Be}^7 \rightarrow \mathrm{Li}^7 + \nu_e \qquad E_\nu = 0.38, 0.86 \text{ MeV} \tag{2.19}$$

$$^8\mathrm{B} \rightarrow ^8 \mathrm{Be}^* + e^+ + \nu_e \qquad E_\nu \leq 14 \text{ MeV} \tag{2.20}$$

$$p + e^- + p \rightarrow ^2 \mathrm{H} + \nu_e \qquad E_\nu \leq 1.44 \text{ MeV} \tag{2.21}$$

These reactions comprise the so-called *pp chain*. A second set of fusion processes, the Carbon–Nitrogen–Oxygen (CNO) cycle, also contributes to solar neutrino production. The CNO flux is highly sensitive to the Sun's core metallicity and provides a means to distinguish between high- and low-metallicity solar models [78].

In addition to flux measurements, the solar neutrino spectrum encodes information about neutrino flavor evolution. In particular, the energy-dependent suppression of the ν_e flux due to matter-enhanced oscillations—the Mikheyev–Smirnov–Wolfenstein (MSW) effect—offers a direct probe of neutrino propagation through the solar interior [25].

With a 100 ton-year exposure, Selena is expected to yield the spectrum shown in Fig. 2.9, adapted from Ref. [47]. For *pp* neutrinos, we anticipate $\mathcal{O}(1000)$ tagged capture events, enabling $\sim$1% statistical precision and placing a stringent constraint on the solar neutrino luminosity. For *pep* neutrinos, $\mathcal{O}(100)$ events provide $\sim$10% resolution, directly probing the MSW transition region. CNO neutrinos are expected to be measured with comparable 10% precision, sharpening existing measurements of the CNO cycle and improving constraints on the solar metallicity problem [79]. Moreover, Selena's high energy resolution may allow for direct observation of thermal shift of the ^{7}Be and *pep* lines, enabling the first direct measurement of the solar core temperature via neutrino spectroscopy.

2. Sterile Neutrino Searches via the Gallium Anomaly Selena can also investigate the so-called *gallium anomaly*, a long-standing discrepancy in electron neutrino capture rates observed in calibration measurements by the GALLEX and SAGE experiments. These detectors used high-activity monoenergetic ν_e sources such as ^{51}Cr and ^{37}Ar to measure the reaction:

$$\nu_e + {}^{71}\text{Ga} \rightarrow {}^{71}\text{Ge} + e^- \tag{2.22}$$

However, the observed interaction rates were consistently 10–20% below expectations. This deficit was confirmed in 2022 by the BEST experiment [77], which placed a 3.4 MCi ^{51}Cr source inside two concentric gallium targets at baselines of $\sim$40 cm and $\sim$70 cm. BEST reported measured capture rates of $79 \pm 5\%$ and $77 \pm 5\%$, respectively, compared to predictions.

The leading interpretation of this anomaly involves oscillation into a sterile neutrino. A Selena detector, equipped with a high-activity 3.5 MCi ^{51}Cr source at its center, and a 10 ton active volume, could observe $\mathcal{O}(10^4)$ tagged ν_e capture events within a 60-day exposure. Because of Selena's fine spatial resolution and background-free signature, such a setup could probe sterile neutrino oscillations with high sensitivity. The projected sensitivity reach is shown in Fig. 2.9.

Chapter 3

TOPMETAL-II$^-$

Selena's first effort toward developing a hybrid amorphous selenium (aSe)–CMOS pixel detector utilized the Topmetal-II$^-$ active pixel sensor (APS). Topmetal-II$^-$ is a CMOS pixel array originally designed for low-noise (< 15 e$^-$) direct charge sensing in gaseous time projection chambers [65]. The array consists of 72 x 72 pixels with an 83 μm pitch. Each pixel features an exposed topmetal pad that serves as a direct charge collection node. The chip supports both digital and analog readout modes; however, for this application, only the analog rolling shutter readout was used, described in Section 4.1.3. This section summarizes the initial tests and results obtained with the early hybrid aSe prototypes, which were first reported in Ref. [76]. Given that some technical details of the Topmetal-II$^-$ and its testing setup are reiterated for TopmetalSe, a more extensive technical discussion will be reserved for chapter 4.

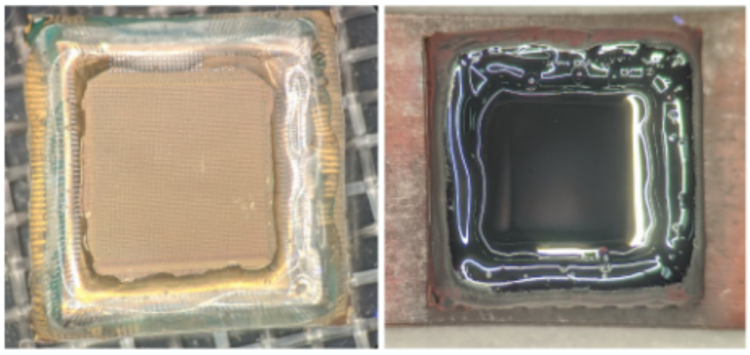

Figure 3.1: **Topmetal-II$^-$ aSe Deposition.** Left shows device pre-deposition, with epoxy covering the wire bonds. Right shows 545 μm deposition of aSe.

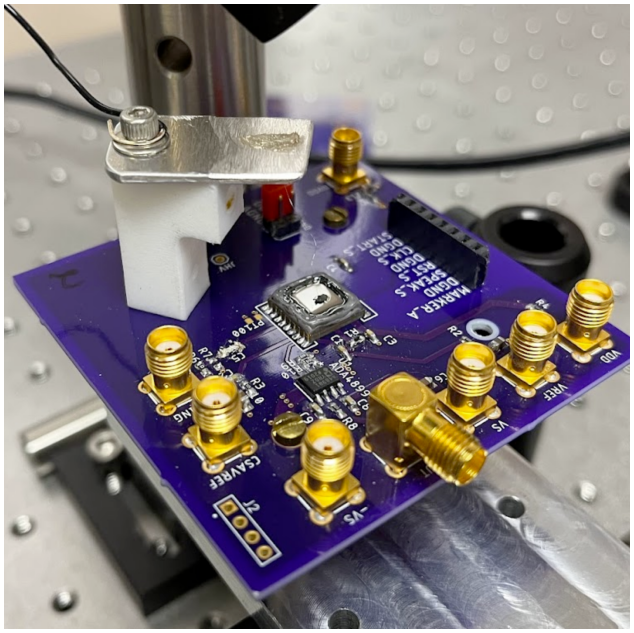

Figure 3.2: **Topmetal-II$^-$ Test Setup** Test board with the aSe/Topmetal-II$^-$ device mounted in the center. HV stand is in the upper-left and is connected to the detector with a small bonding wire and attached via a conductive carbon paint. Test board contains analog I/O (SMA connectors), digital I/O (black headers) and an output buffer amplifier.

3.1 aSe Hybridized Devices

The device is shown in Figure 3.1. To couple the Topmetal–II$^-$ to an aSe layer, the exposed wire bonds are encapsulated in a non-conductive epoxy to protect them during selenium deposition. The aSe layer, with a thickness of 545 μm, is thermally evaporated by Hologic Inc. using a commercial deposition system. Following this, a 20 nm-thick metal electrode is deposited on top of the aSe to serve as the biasing cathode.

Following aSe deposition, the detector is mounted on a test board, and its I/O is soldered into place. This setup, depicted in Figure 3.2, is then situated within a vacuum chamber. The test board provides both I/O to the chip and output buffering for the analog chip signals. External power supplies deliver both power and biasing to the Topmetal-II. The digital control of the pixel array is handled by an external BASYS 3 FPGA Board with a custom firmware. The FPGA supplies to Topmetal-II$^-$ the pixel clock, typically 25 MHz.

The analog output of Topmetal-II$^-$is routed to an output buffer and then digitized using a high resolution CAEN digitizer.To trigger the digitizer readout, we split the array output between the digitizer and a lower resolution trigger ADC connected to the FPGA. The FPGA continuously monitors and stores the pixel values and sends a trigger to the digitizer when a deviation from the pixel baseline is detected, prompting data transfer to the lab computer.

High voltage (HV) is applied to the aSe anode via a 25 μm bonding wire, secured with a small dab of carbon paint and connected to an external HV stand and a polyamide-insulated wire. A CAEN HV supply provides the HV. While typical aSe detectors are operated at $\geq 10V/\mu$m, we were only able to achieve a field of $4V/\mu$m due to sparking at higher voltages. To minimize this risk, we operated with a vacuum pressure $< 10^{-4}$. Despite this reduced field, previous work in Ref. [80, 81] demonstrated single photon x-ray counting in aSe detectors under the same field strength.

Data processing involved converting the raw analog output waveforms into individual image frames. The array was operated with a 25 MHz pixel clock ($\approx$5 kHz frame rate), and the digitizer sampled at 500 MHz, yielding 20 samples per pixel per frame; these were averaged to obtain a single pixel value. Each readout event consisted of five consecutive frames.

Pixel-dependent offsets were corrected using a baseline image constructed from the entire dataset. For each pixel, the median of its values over all frames was computed, which suppresses contamination from occasional radiation hits more effectively than a mean. This median baseline was subtracted from every frame to create an image. The image noise σ was estimated as the σ over all the pixels of a single image, and pixels exceeding 4σ above baseline were identified as radiation events.

3.1.1 Results and Discussion

To measure our hybrid detector's sensitivity to radiation, we irradiated our detector with a ^{57}Co γ source and a ^{90}Sr β source. The sources were placed a $\sim$ cm away from our detector with minimal collimation, resulting in an isotropic exposure over the detector. We biased a

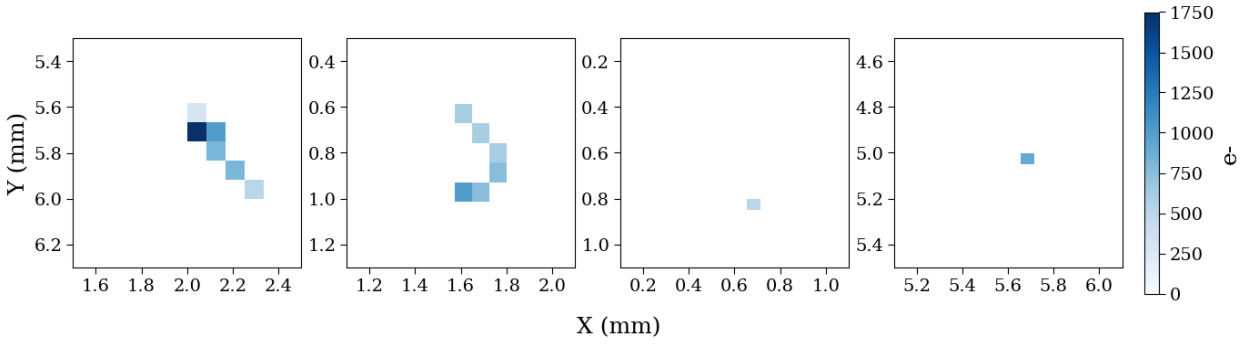

Figure 3.3: β **and** γ **Tracks in Topmetal-II$^-$ coupled aSe Detector** Left two plots show tracks collected from a ^{90}Sr β emitter, while right two plots show γ tracks from a ^{57}Co source. Background pixels below 3σ of the baseline are hidden. Detector was biased at 4 V/μm.

detector at 2 kV ($4V/\mu$m)

^{90}Sr undergoes two sequentialβ decays, first to ^{90}Y ($T_{1/2}$ = 29 yr, Q = 500 keV), and then to ^{90}Zr ($T_{1/2}$ = 64 hr, Q = 2279 keV). In our measurements, we used a source with an activity of $\sim$ 25 μCi, yielding a high rate of β particles, many with MeV-scaled energies. These β particles produce extended charge tracks in the aSe/CMOS detector, which are clearly visible in the recorded data. Figure 3.3 displays representative examples of such tracks, which span multiple pixels across the array. The tracks exhibit energy loss behavior consistent with expectations from ionizing radiation in amorphous selenium, including the presence of Bragg peaks near the end of the particle range, where energy deposition per unit length increases sharply.

^{57}Co, on the other hand, predominantly emits a 122 keV γ ray with an 85% branching ratio, along with a weaker 136 keV γ line (11%). In aSe, γ rays at these energies interact almost entirely via photoelectric absorption, producing a single photoelectron with a range < 20 μm [82]. Figure 3.3 shows a typical event, where all the energy is deposited over a single pixel. We observed a very good noise performance in the background pixels of 23 e$^-$ RMS. Despite the low-noise and data collection over several days in various readout configurations

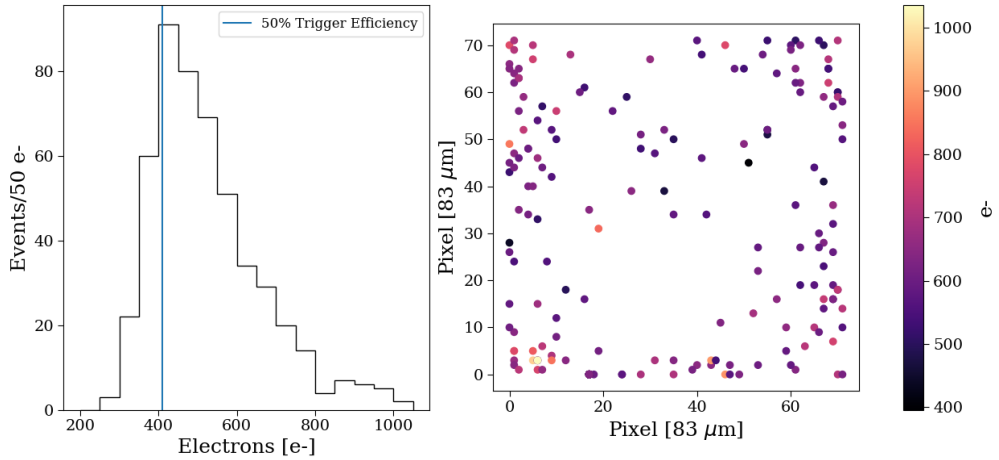

Figure 3.4: **Energy Spectrum and Spatial Distribution of ^{57}Co events in aSe/Topmetal-II$^-$** Left shows an energy spectrum taken from a representative dataset at 4V/μm. The apparent peak is likely a result of the trigger cut-off, while the expected peak at 1220 e$^-$ is not visible. Right shows locations of a subset of events on the pixel array, demonstrating anisotropy of event locations.

and assembling energy spectra, we did not observe a distinct monoenergetic peak at 122 keV. However, our results demonstrate the ability of aSe/CMOS detectors for single electron and photon detection.

The absence of a clear 122 keV peak in our data may be attributed to two primary factors: (1) non-uniform electric field distribution across the XY plane of the array, and/or (2) incomplete charge collection due to pixel geometry. Evidence of field non-uniformity is shown in Figure 3.1, where the aSe layer and top electrode are visibly uneven across the Topmetal–II$^-$ array. This unevenness results from the epoxy coating over the wirebonds, which prevents a flat deposition. We suspect that this geometry not only limited the maximum applicable high voltage to below 2 kV due to sparking, but also distorted the internal electric field within the detector. Figure 3.4 presents a scatter plot of ^{57}Co event locations across the XY plane, revealing anisotropy in their spatial distribution. This further supports the conclusion that the electric field in the aSe layer deviates from a uniform, vertical profile.

Figure 3.4 also shows an energy spectrum from one of our data runs. Using the calibration from Ref. [51], the 122 keV peak is expected at 1220 e$^-$ under the applied field; however, we

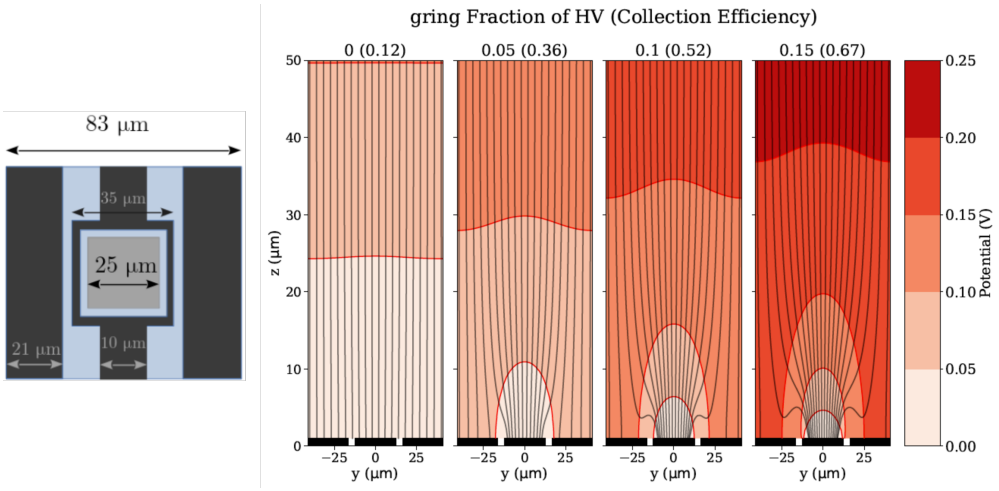

Figure 3.5: **Topmetal-II$^-$ Pixel Geometry and Collection Efficiency Simulations** Left is top-down view of a pixel, showing the metal electrode (light grey), interlayer dielectric (blue) and guard ring (dark grey). Right is the cross sectional view of the simulated electric field lines and potential of a single pixel. The HV electrode is located far above the top boundary of the plot, while pixel structure lies at the bottom. Simulations are shown for varying guard ring bias values (expressed as a fraction of the applied HV), with the corresponding collection efficiency indicated above each panel.

observe only a broad distribution below 1000 e$^-$. The overlaid trigger efficiency line suggests that the apparent peak is likely an artifact introduced by the trigger threshold. This suggests that our pixels lack full charge collection from the aSe, which comes from the Topmetal-II$^-$ pixel geometry. Figure 3.5 illustrates the individual pixel geometry. The central 25 μm x 25 μm area is the exposed collection electrode, surrounded by a metal structure known as the guard ring (guard ring) which can be pulsed and biased independently. The guard ring and collection electrode are separated by a thin region of oxide passivation and everything besides the collection electrode is covered in an oxide passivation layer. The collection node in the center occupies only $\sim$ 10% of the total pixel area, meaning that only the small fraction of charge drifting directly above the small collection node was effectively collected during our testing procedure.

We investigated this hypothesis through a Finite Element Analysis (FEA) simulation of the pixel geometry inside the detector in COMSOL. In the simulation, the HV electrode

is biased at 1 V and the collection electrode at 0 V. Under periodic boundary conditions, COMSOL solved Maxwell equations for the electric field lines, allowing us to visualize the trajectories of the charge carriers. We defined the collection efficiency to be the fraction of field lines which end on the collection electrode. Under the baseline biasing conditions (0 V guard ring bias) of our detector, the simulated collection efficiency was $\sim 10\%$.

We explored the possibility of improving this efficiency by biasing the surrounding guard ring structure. Simulations were repeated with the guard ring biased between 0 and 1 V, while the collection node remained at 0 V. As shown in Figure 3.5, increasing the guard ring voltage improved field line focusing and collection efficiency. However, implementing this approach in practice would require guard ring biases of several hundred volts, beyond the design limits of the Topmetal-II$^-$ architecture.

Chapter 4

TOPMETAL-SE

TopmetalSe is a low-noise CMOS pixel array fabricated in the open-source Skywater 130 nm process and the first prototype pixel array designed for Selena. The design carries over the basic analog readout structure used in the Topmetal-II$^-$, with each pixel containing an exposed top metal electrode directly connected to a CSA and a rolling shutter array readout. The pixel pitch is drastically decreased from 83 μm to 15 μm, which we identified as a target geometry in Chapter 2. We designed the pixel performance to match that of the Topmetal-II$^-$, with low noise ($10 - 20$ e$^-$) and low power consumption (< 1 μW/pixel). Additionally, we have optimized the electrode pixel geometry to imrove the charge collection efficiency from the previous generation. This chapter will discuss the design and testing of the TopmetalSe.

4.1 Design

The TopmetalSe (TMSe) sensor was developed using the open-source SkyWater 130 nm CMOS process, released in 2021 by Efabless in collaboration with Google[1]. The availability of a fully open-source process design kit (PDK) provided us with a unique opportunity to explore custom ASIC design at low cost and with minimal barriers to entry. The TMSe was submitted for tapeout on a Multi Project Wafer (MPW) run in June 2022 and was delivered in June 2023. The full chip is 3.6 x 5.2 mm^2, shown in Figure 4.1. Although the die includes additional circuitry and unused space, the central feature is the 100 x 100 pixel array. (1.5 x 1.5 mm^2). The following section describes the pixel architecture in detail, including in-pixel

[1] https://www.skywatertechnology.com/efabless-launches-chipignite-with-skywater-to-bring-chip-creation-to-the-masses/

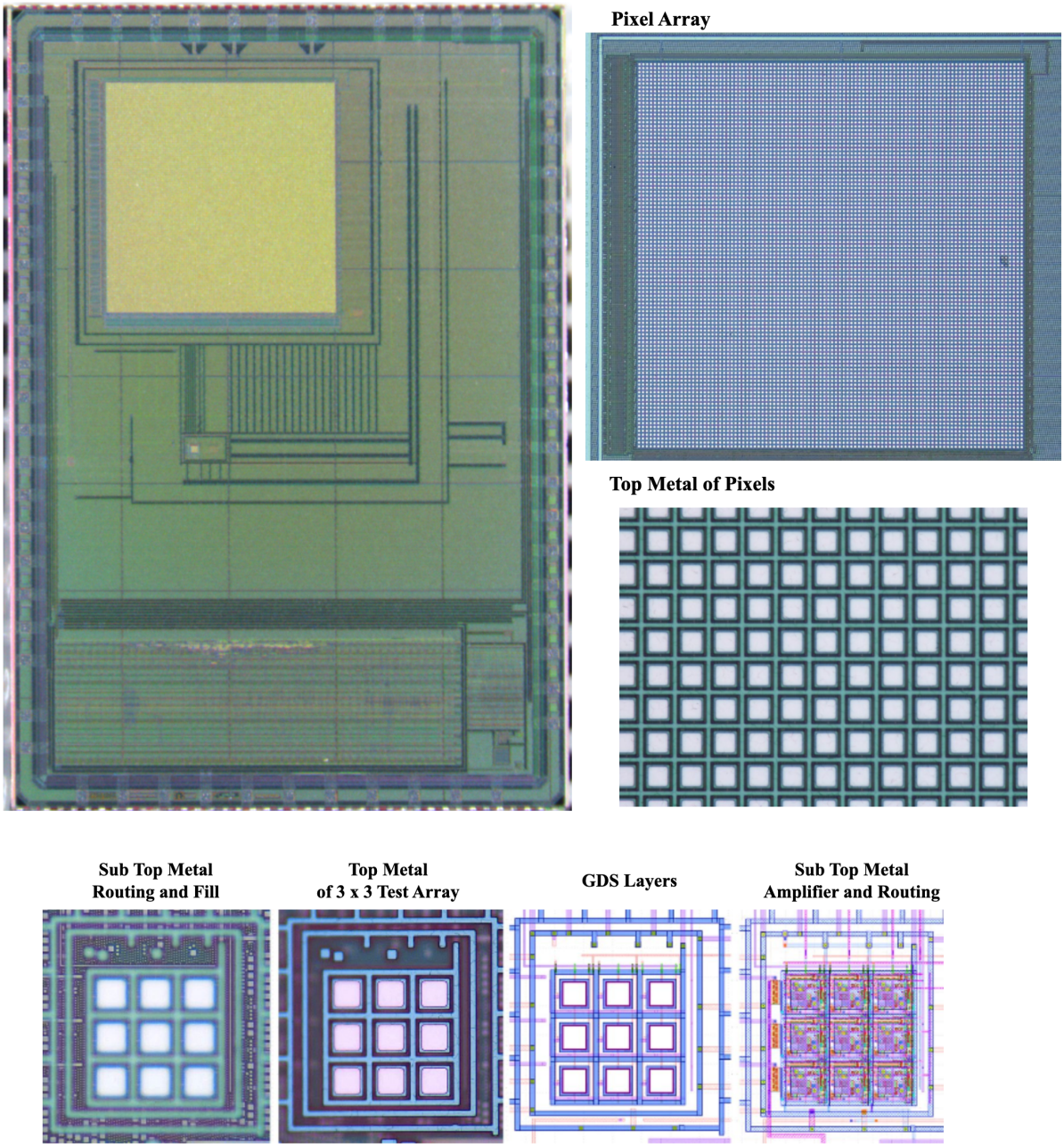

Figure 4.1: **Micrograph of TopmetalSe** Top left shows the total die size is 3.588 x 5.188 mm^2. The periphery is the I/O pad ring, bottom quarter is the Caravel RISC-V SOC, while the the rest above is the TopmetalSe project space. The large pixel array is in light green and covers 1.5 x 1.5 mm^2. Top right shows a zoom in on the actual pixel array, showing the top metal layers with exposed electrodes. Bottom panels show underlying structure of the 3 x 3 test array, showing micrographs of the top two metal routing layers (left), and the underlying structures designed during layout (right).

amplifier, the charge collection electrode, and the array readout structure.

4.1.1 Pixel Frontend

Like the Topmetal-II$^-$, the pixel frontend consists of charge sensitive amplifier (CSA). Unlike the Topmetal-II$^-$, however, the open-source nature of the TMSe enables a more detailed discussion of the underlying circuitry.

Figure 4.2 shows the schematic of the pixel readout circuit. The input stage (purple dotted box) employs a telescopic cascode OpAmp, an amplifier topology known for its high gain, low noise and low power consumption, useful for in-pixel amplifiers. Its open-loop voltage gain is typically approximated as [83]:

$$A = g_{m1} R_{out} \tag{4.1}$$

$$R_{out} = [\ r_{o1}(g_{m3} r_{o3})\ ||\ r_{o6}(g_{m8} r_{o8})\ ] \tag{4.2}$$

where g_m is the mosfet transconductance and R_{out} is the parallel combination of the output resistances of the NMOS and PMOS branches. In the schematic, M1–M4 form the NMOS input branch: M1 and M2 are the differential input pair, while M3 and M4 serve as NMOS cascode devices that increase output resistance. PMOS devices M5–M8 form the cascode current-mirror load, providing the high-gain telescopic stage. The bias transistors Mb1 and Mb2 are NMOS current sources, while Mb3 is a PMOS bias device for the source-follower stage.

The feedback network (dashed orange) consists of a metal–insulator–metal (MiM) capacitor and a PMOS transistor Mf. The MiM capacitor integrates the charge signal at the input node, and its value is determined by its size: 8fF for a 4 μm^2 capacitor. For an OpAmp with a large open-loop gain, its closed-loop gain can be approximated by [59]:

$$G = -\frac{A}{\frac{1}{A} + \frac{1}{A_{fb}}} \tag{4.3}$$

$$G \approx -\frac{1}{A_{fb}} \tag{4.4}$$

where A is the open-loop gain described in eq. 4.2, and A_{fb} is the gain of the feedback network. For a feedback capacitor:

$$G = -1/C_f \tag{4.5}$$

There is an additional gain factor resulting from the two source-follower stages, M9 and M11. Neither behaves as an ideal source follower due to their finite output impedance and limited current drive capability. As a result, each stage contributes a voltage attenuation factor, typically less than unity, which must be included in the overall system gain. The total system gain is therefore given by the product of the CSA gain and the combined attenuation factors of M9 and M11, which can be modeled as:

$$G_{\text{total}} = \left(-\frac{1}{C_f}\right) \cdot \gamma_9 \cdot \gamma_{11}, \tag{4.6}$$

where γ_9 and γ_{11} represent the voltage gain (typically $\sim$0.7–0.9) of each source-follower stage, depending on their bias current and load.

The transistor Mf acts to discharge the feedback capacitor. By tuning CSA_VREF and VREF to keep Mf in the sub-threshold region (weak inversion), Mf acts as a very high-value resistor, R_f. Its value: [83]:

$$R_f \approx \alpha \exp\left[V_{th} - V_{SG}\right] \tag{4.7}$$

$$V_{SG} = VREF - CSA\_VREF \tag{4.8}$$

where α is a term which contains all the process dependent variables and V_{th} is the threshold voltage. In general, we tune R_f to maximize the RC decay time so that the CSA output retains the full signal peak long enough to be sampled during rolling-shutter readout. In a rolling-shutter architecture, pixel rows are read out sequentially rather than simultaneously; therefore, the signal must persist until the row containing the hit pixel is addressed.

Lastly, M9 serves as a level-shifting source follower that buffers the CSA output and ensures that its voltage swing remains within the range required to keep the CSA input correctly biased through the feedback loop. Without this stage, the CSA output could shift the input bias point and destabilize the amplifier operation.

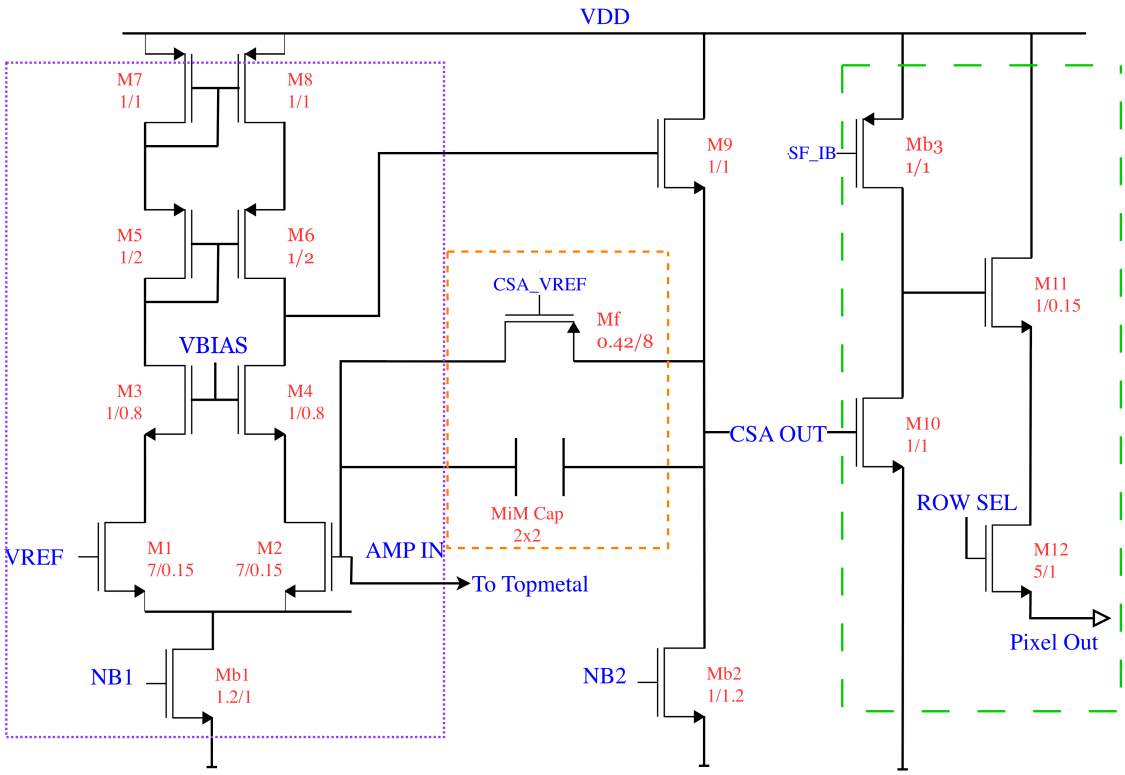

Figure 4.2: **Pixel Schematic** Purple dotted shows the pixel frontend cascode operational amplifier. Orange dashed shows the feedback network. Green dashed shows the output stage. All body connections can be assumed to be GND for the NFETs, and VDD for the PFETS. Red labels next to each MOSFET indicate transistor dimensions in width/length (W/L) in microns.

The output stage (dashed green) consists of an additional source follower stage to ensure high input impedance and high drive strength to the pixel output. M12 acts as a row selection switch, moving the pixel signal onto the output column line when ROW SEL goes high.

4.1.2 Pixel Geometry and Charge Collection

Figure 4.3 shows the topmetal layout of an individual pixel. The geometry was drawn to maximize the charge collection but was limited by the Skywater process rules, namely the minimum width and spacing of the topmetal layer of 1.6 μm. The regions between the metal are filled with a passivation layer known as the top nitride, which has dielectric constant of

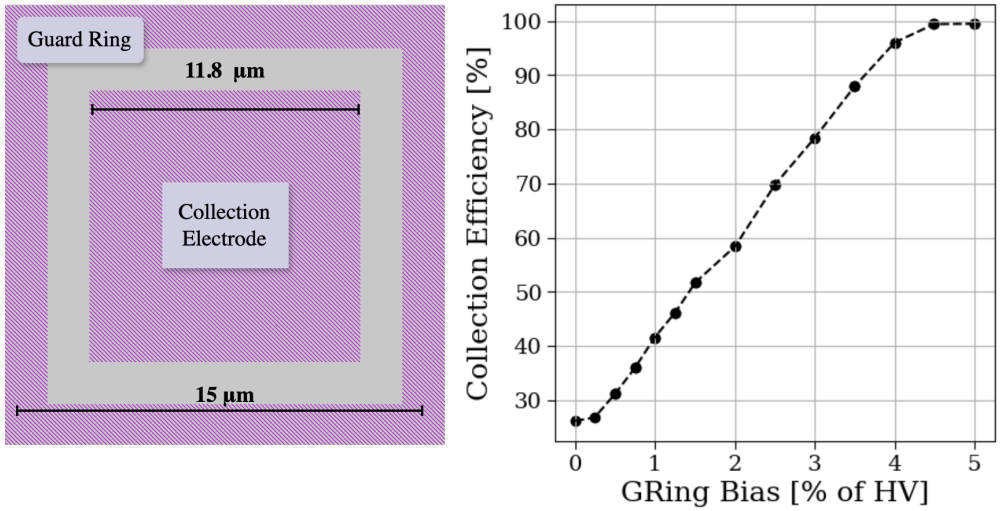

Figure 4.3: **TopmetalSe Pixel Top Metal Geometry and Collection Efficiency** Left shows the pixel geometry, which was limited by the Skywater 130 nm PDK. Collection Efficiency was taken from simulation of the electric field lines in COMSOL. It was defined as the fraction of field lines ending on the collection electrode in the center. X-axis is the DC bias applied on the Guard Ring structure. Simulation was done by E. Solis.

7.5. All areas but the central collection electrode is covered in a top oxide with a dielectric constant of 3.9. The collection electrode is directly connected to the in-pixel amplifiers through vias, conductive plugs for routing signals between metal layers. The 1.6 μm width guard ring (guard ring) is shared between pixels, giving an effective 0.8 μm width per pixel. Parasitic extraction performed using MAGIC VLSI gives the parasitic capacitance between the guard ring and the collection electrode as 3.1 fF. By pulsing a voltage pulse on the guard ring, we can use this capacitance to inject charge and calibrate our in-pixel amplifiers, demonstrated in section 4.3.1.

Like the Topmetal-II$^-$, we model the collection efficiency of the pixel through FEA simulations in COMSOL. Electric field line simulations reveal the trajectories of drifting charge carriers, which we use to calculate the collection efficiency. Applying a DC bias to the guard ring enhances focusing of field lines toward the collection electrode. Figure 4.3 shows the simulated collection efficiency as a function of guard ring bias for a TopmetalSe pixel coupled to a 500 μm aSe layer. The results demonstrate that meaningful improvements in collection

efficiency can be achieved within realistic guard ring biasing ranges. This reflects the updated pixel geometry, in which the exposed electrode occupies a larger fraction of the total pixel area.

4.1.3 Array Readout

The pixel selection of the 100 x 100 pixel array is similar to a switched memory array. As described above, each pixel's output is connected to a shared column line and is activated by a row selection signal. Likewise, each column line is gated by a column selection signal and ultimately connected to a single shared output line.

To implement the rolling shutter readout, two 1 x 100 shift registers are used, one for row selection and one for column selection. The parallel outputs of these shift registers are connected to the corresponding row and column selection lines. By shifting a high signal through the registers on each clock cycle, a new row and column are sequentially selected, enabling pixel-by-pixel readout across the array. Figure 4.4 demonstrates this readout method.

The single output line is buffered via an open-source OpAmp design which had been submitted to a previous eFabless tapeout[2]. The OpAmp is connected as a voltage follower (gain of 1) in order to drive any output loads. Its output is directly connected an analog I/O pad for wirebonding.

4.2 Test Setup

To test the TopmetalSe chip, it is mounted onto a custom PCB that provides signal I/O, power and bias regulation, output buffering, and connectivity to external equipment. A top-level diagram of the entire test system is shown in Figure 4.5. This section will describe the custom-designed components in detail.

---

[2] `https://github.com/diegohernando/caravel_fulgor_opamp`

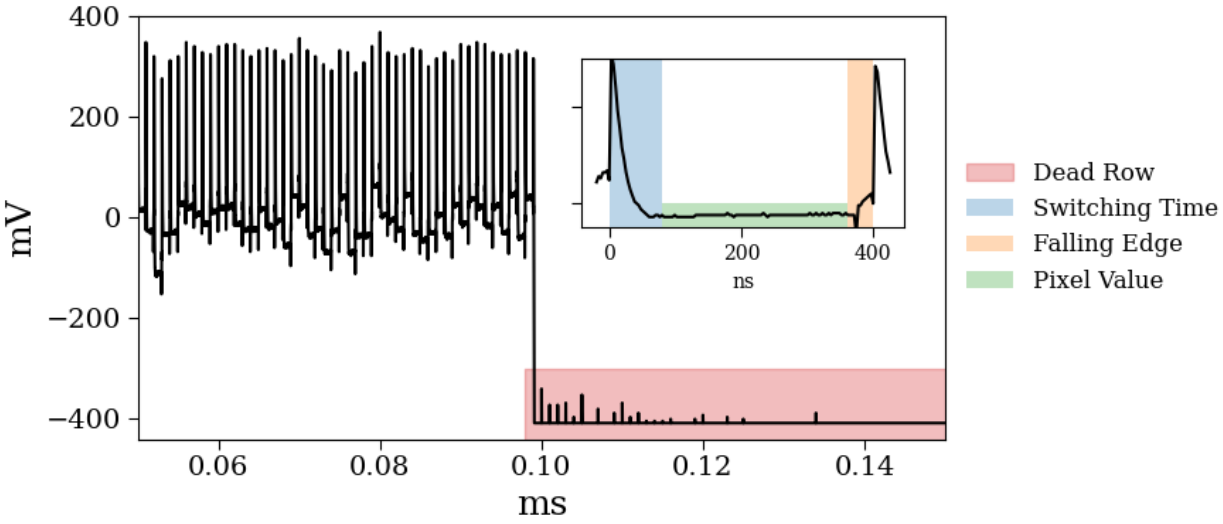

Figure 4.4: **Rolling Shutter Readout** Shows the analog readout signal of TopmetalSe over 10 μs. Inset plot shows a single pixel, where blue is the transistor switch, green is the pixel value that gets averaged over, orange is the anomalous falling edge effect, which gets pushed into the switching time by increasing the pixel clock duty cycle.

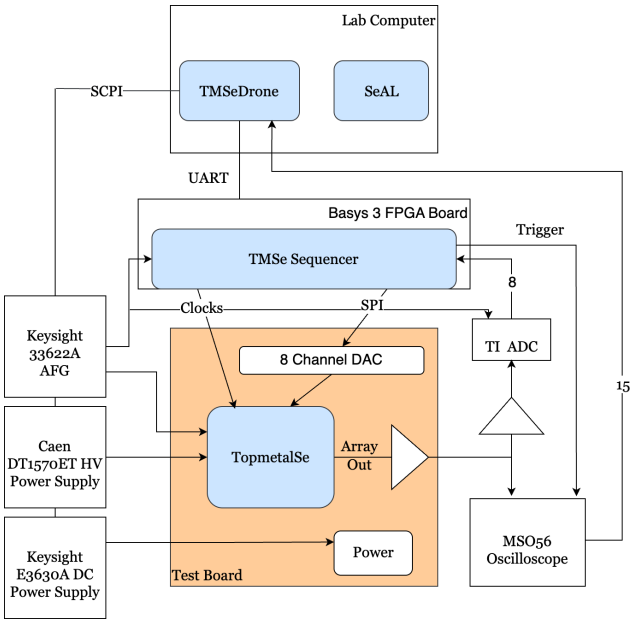

Figure 4.5: **Testing Setup for TopmetalSe**

4.2.1 Test Board

The test board was designed in collaboration with the CENPA electrical engineering team, D. Peterson and T. Van Wechel. TopmetalSe is mounted and wirebonded onto a carrier, which plugs into our test board. For power, a ±5 V power rail is supplied by an external DC power supply; onboard voltage regulators generate the 1.8 V and 3.3 V rails required for chip operation, while the ±5V rail powers the analog output buffers. These buffers are implemented using ADA4899 OpAmps configured as source followers to drive 50 Ω lines. An onboard TI DAC8568 digital-to-analog converter (DAC) sets the chip's bias voltages/currents. There are also components on the PCB to communicate with the embedded RISCV CPU (the caravel core), but our design makes no use of it.

4.2.2 TopmetalSe Sequencer

The PCB interfaces with a BASYS 3 FPGA development board, the code for which is called the Sequencer. It manages the rolling shutter pixel selection and communicates with the DAC via an SPI bus. The rolling shutter is managed by the clock sequencer that directly communicates with the row and column shift registers.

The FPGA itself is controlled over a USB connection from the lab PC, enabling real-time control and data acquisition during testing. The protocol uses UART with a baud rate of 9600 and 8-bit words. The exact data format of the 8-bit words is described on the TMSe Sequencer GitHub.[3] Through 4 control bits, the FPGA can be selected to perform the following:

- **DAC Bias Control** with the following 32 bits for channel and voltage selection.
- **Small Array Pixel Selection** via the following 4 bits.
- **Small Array Pixel Selection** via the hardware switches on the BASYS3 board.

[3] `https://github.com/selena0vbb/TopmetalSe_Sequencer`

- **Large Array Pixel Selection** with the following 16 bits.

- **Large Array Rolling Shutter** on/off.

4.2.3 Trigger

In order to decrease the data processing requirements, we developed a pixel-by-pixel trigger on the FPGA to accommodate the varying pixel baselines all on the complex rolling shutter analog readout. The trigger was originally developed for Topmetal-II$^-$ testing, but we repurposed it for TopmetalSe and summarize its operation here. The output from the array was split using a 50 Ω RF splitter. One branch was directed to the oscilloscope for digitization, while the other was routed to a dedicated trigger amplifier. This amplifier applied a DC offset to center the signal baseline and amplified deviations from the baseline with a gain of six. The resulting signal was digitized by a fast 8-bit Texas Instruments ADC, operating at a clock rate in synchronization with the pixel clock. The digital output from the ADC was sent in parallel to an Artix-7 FPGA, where a real-time comparison was performed between successive pixel values. Specifically, for each pixel p_{ij}, the FPGA evaluated whether the change in signal between consecutive frames exceeded a user-defined threshold T_{trig} in ADU, triggering on a decrease in amplitude consistent with the expected negative polarity of aSe-induced charge pulses:

$$p_{ij}[t] - p_{ij}[t-1] < T_{\text{trig}}. \tag{4.9}$$

Upon satisfying this trigger condition for any pixel, the system initiated a full readout by digitizing the waveform on the oscilloscope and transferring to the computer and capturing the response from the entire sensor array rather than from only the triggered pixel.

4.2.4 TopmetalSe Drone

The software to control the test system is a python package called TopmetalSe Drone.[4] It provides central control over all the lab equipment for the testing setup. Standard SCPI commands communicate with the HV and non-HV power supplies, as well as the arbitrary function generator (AFG) for supplying the clocks and any test pulses. UART commands manage the FPGA code and configuration. The software accepts configuration **.ini** files to precisely set bias voltages and currents, pixel selection, and clocking.

Data output is handled by the Tektronix MSO56 oscilloscope using the Tektronix HSI for fast data transfer. The oscilloscope front-end allows fine control over waveform resolution and record length. The exact data length and resolution can be tuned using the oscilloscope front-end. Several readout modes are supported:

- **Single pixel mode** captures multiple waveforms from a single pixel when the pixel clock is halted. The resulting waveform(s) are saved in a .ROOT file.

- **Frame mode** records a single rolling shutter readout over the full array. The data are stored either as the full analog waveform or processed images in a .npy file.

- **Multi-exposure mode** enables sequential rolling shutter acquisitions triggered by the FPGA.

- **Video mode** provides a semi-continuous stream (∼2 FPS) of real-time readout and frame processing from the full pixel array.

The multi-functionality of TopmetalSeDrone allows for near fully automated control and readout of TopmetalSe.

---

[4] `https://github.com/selena0vbb/TopmetalSeDrone`

4.3 Test Results

The capabilities of the TopmetalSe prototype are demonstrated through a series of targeted tests. We begin by evaluating the performance of the in-pixel amplifier, described in section 4.1.1, to verify its gain, noise and variation. This is followed by a demonstration of image acquisition from the pixel array, confirming readout functionality across the array. We then show that the system is capable of measuring charge collected on the pixel electrode, ensuring its suitability for charge-sensing applications. Finally, we perform a precise calibration of the charge collection using the photoelectric effect, establishing a quantitative relationship between input charge and output signal.

4.3.1 Single Pixel Performance

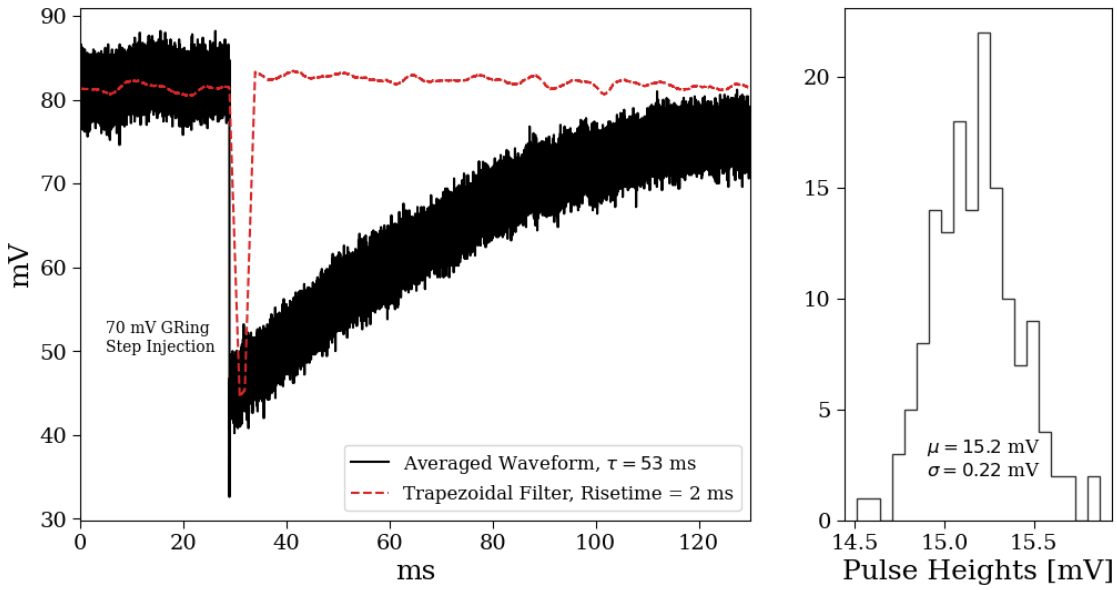

Figure 4.6: **Single Pixel Pulse** Left: Averaged response to a 70 mV step injection, showing an exponential decay with $\tau = 53$ ms and corresponding trapezoidal filter output with a risetime of 5 ms. Right: Histogram of extracted pulse heights, fitted with mean $\mu = 15.2$ mV and $\sigma = 0.22$ mV. Parasitic capacitances from EDA software results in a gain of 11 mV/e$^-$and ENC of 20 e$^-$

We measure the output response of the in-pixel amplifiers by injecting a test pulse via the

parasitic capacitance of the pixel guard ring to the input electrode, 3.1 fF. A low-frequency ($\leq$ 5 Hz) square wave of 70 mV ($\sim$1350 e^-) is used as the test signal, allowing sufficient time for the output to decay back to baseline between pulses. Since the ultimate application involves measuring positive charge (holes) generated in aSe, the analysis focuses on the amplifier's response to the positive edge of the input pulse, corresponding to the negative edge of the output.

For a single pixel, the result is shown in Figure 4.6. TopmetalSe Sequencer and TopmetalSe Drone allow us to stop the rolling shutter on a selected pixel to collect full single pixel waveforms. We digitize and save the output using an MSO56 oscilloscope.

The voltage output of the CSA is described by the following differential equation:

$$\frac{dV}{dt} = \frac{V}{\tau_f} - \frac{i(t)}{G_{total}} \tag{4.10}$$

where $\tau_f = R_f C_f$, and G_{total} is the effective charge to voltage gain. For a short input current pulse that can be approximated as a delta function:

$$i(t) = Q\delta(t) \tag{4.11}$$

$$V(t) = \frac{Q}{G_{\text{total}}} e^{-t/\tau_f} \qquad t > 0, \tag{4.12}$$

where Q is the total injected charge. The peak voltage $V = Q/G_{\text{total}}$ thus corresponds directly to the gain of the system.

To obtain an initial estimate of the waveform parameters, we fit the waveform to the following form:

$$V(t) = S\left(\alpha\left[t - t_0\right]\right) \times A e^{\frac{t-t_0}{\tau}} \tag{4.13}$$

$$S(x) = \frac{1}{1 + e^{-x}} \tag{4.14}$$

where $S(x)$ is the logistic sigmoid function, which acts as sharp step function centered at t_0, the time of pulse injection (assuming sufficiently large α). A is the initial pulse height estimate, and τ is the CSA decay constant.

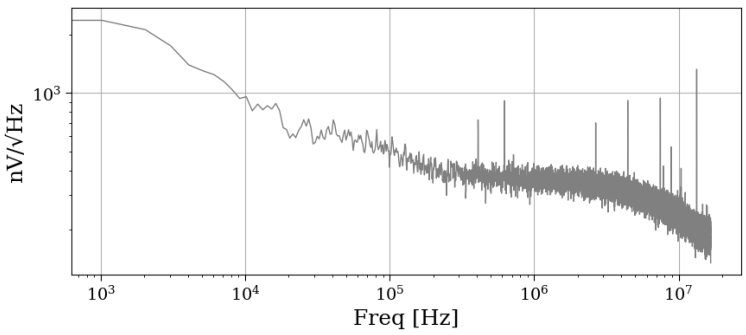

Figure 4.7: **Single Pixel Noise Spectral Density**

Traditionally, CSAs are measured using a trapezoidal filter, used for its optimal noise rejection and signal shaping. The filter uses a tunable rise time and flat top time to extract the pulse height in an ideal frequency window, suppressing both low-frequency and high frequency noise. We implement a trapezoidal filter using digital signal processing (DSP) in software. The DSP filter first performs a pole-zero correction to remove the decay time of the signal, given by the fitted value of τ. The trapezoidal filter then works by performing a difference of two moving windows, separated by a time delay F. The window length R defines the rise time of the filter, while F defines the flat top. The signal height is given by the pulse height during the flat top.

Over multiple pulses, the mean (μ) and width (σ) of the distribution of pulse heights give us our charge conversion gain and the equivalent noise charge (ENC). For the plotted pixel, the charge conversion gain is calculated as $G = 15.2$ mV/1350 e^- $= 11.2$ $\mu V/e-$.

The ENC is measured as $ENC = \sigma/G = 20e^-$. Figure 4.7 shows the amplitude spectral density (ASD) of the baseline noise for a single pixel across a frequency range of 1 kHz to 20 MHz. The spectrum demonstrates a characteristic 1/f (flicker) noise, which dominates below 100 kHz. The white noise extends from this point up until the corner $\sim$ 4 MHz, a result of the limited analog bandwidth of the CSA.

We can repeat calibration of across the entire array. Figure 4.8 shows the distribution of the charge conversion gain, ENC and decay time across the entire array with a trapezoidal filter risetime of 1 ms. The variation of pixel behavior is expected as a result of the inherent

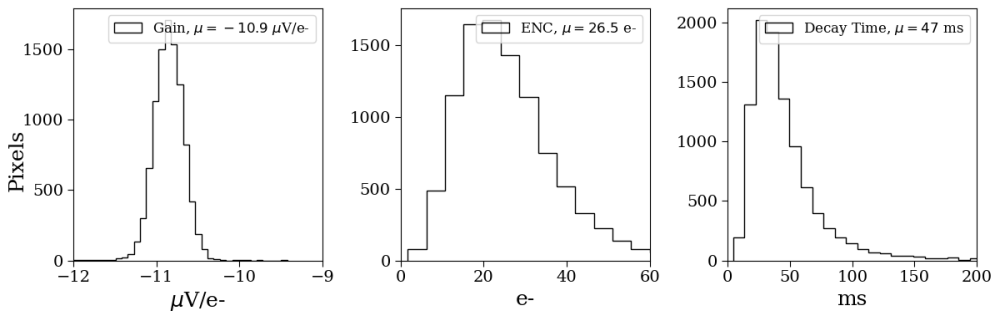

Figure 4.8: **Distribution of Pixel Array Calibration**

CMOS process variation. We report the mean gain as -11 μV/e$^-$and ENC as 26 e$^-$with a mean CSA decay time of 47 ms.

During typical operation, each pixel in the array consumes approximately 913 nW of static power when it is not actively being read out. This power consumption arises primarily from the biasing of the CSA and source follower, which remain continuously active. When a pixel is selected for readout via the rolling shutter and connected to the shared column output buffer, its power consumption increases by an additional 10.8 μ W. Based on the pixel pitch and array geometry, the average static power density across the sensor is approximately 405 μW/cm^2, which is low enough to support passive cooling and minimizes thermal load onto an aSe layer.

4.3.2 Array Imaging

To read out images from the pixel array, a target with a clear structure was needed to generate a visually distinct image. We did this by focusing visible light from a commercial bike light onto the pixel array. Although the pixels were not specifically designed for photon detection, incident photons can still ionize charge within the MOSFETs in the silicon, generating a measurable current. Figure 4.9 shows the light spot and the captured signal, read out through the rolling shutter. The image is generated by first taking an ambient set of frames, where the chip is kept in the dark, and then exposing the chip to light and subtracting the mean of ambient frames from the exposure.

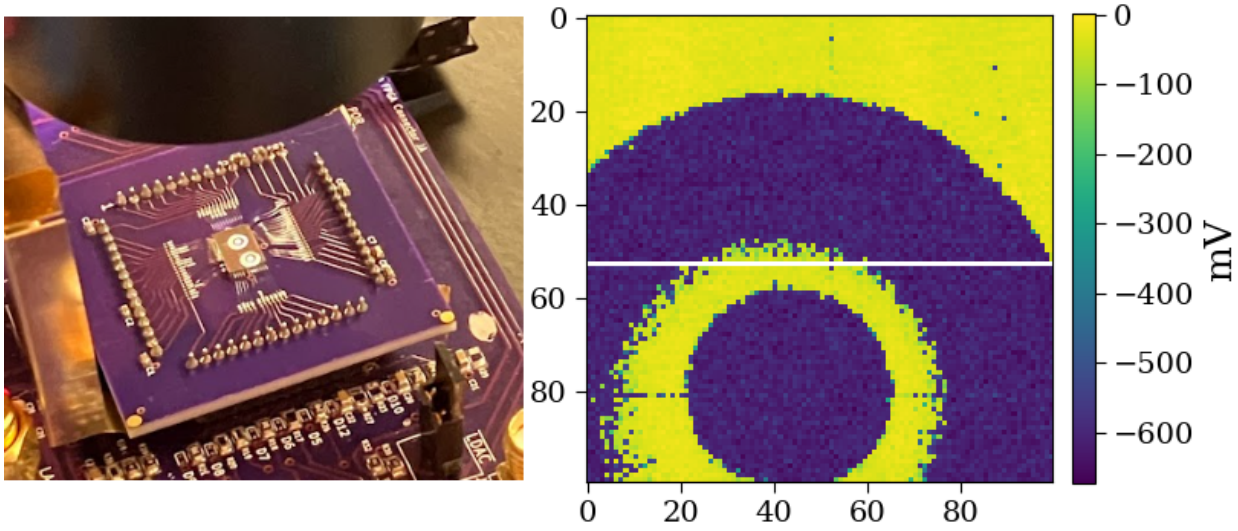

Figure 4.9: **TopmetalSe Imaging** Left: Photograph of the TopmetalSe detector under illumination from bike light and focusing. Right: Reconstructed 2D charge image from a uniform light exposure, which caused pixels to saturate with charge. White band across the middle is a result of a dead row.

We read the array with a pixel clock frequency of 2.5 MHz. An example of the rolling shutter readout is in Figure 4.4. In this mode, each row is sequentially enabled for readout while all remaining rows remain inactive, producing a characteristic waveform consisting of a brief switching transient followed by a stable interval during which the pixel output is valid. We compute each pixel value by averaging over this stable interval. Notably, the image shows that a single row, row 53, was left disconnected during the layout. This dead row produces a clear gap in the rolling-shutter waveform that we can use to identify the row indices, allowing us to find the beginning of the array and reconstruct the full frame.

Although the system was designed to support pixel clock rates exceeding 10 MHz, three key limitations reduced the practical clock speed to below 5 MHz. First, the row-select transistor (M12 in Figure 4.2) was sized with a width-to-length ratio of 5/1, resulting in a slow switching time with a maximum pixel clock frequency of 10 MHz. Strangely, the measured transistor switching time was approximately twice as slow as predicted by simulation, limiting

the clock to 5 MHz. We suspect this is discrepancy due to parasitic effects from the layout which were not fully captured.

Second, we observed an anomalous coupling effect associated with the falling edge of the pixel clock, which injected a transient pulse onto the signal line. This issue was mitigated by maximizing the duty cycle of the pixel clock, thereby shifting the injected pulse closer in time to the following pixel switch event and allowing a clean pixel signal to sample from.

Finally, due to the nature of the rolling shutter readout, we found that frame noise scaled inversely with the pixel sampling time. That is, slower pixel clocks resulted in reduced noise. This behavior was confirmed in the noise spectral density shown in Figure 4.7, where the flat white noise region spans roughly 100 kHz to 4 MHz. Integration over timescales longer than a few microseconds corresponds to averaging over this flat region, where noise samples are uncorrelated. Consequently, the total RMS noise in this regime scales with $1/\sqrt{N}$, where N is the number of independent samples. However, at shorter timescales, below a microsecond, the spectrum is no longer flat. The spectral density rolls off above several MHz due to bandwidth limit of the front-end electronics. In this high-frequency regime, the noise is no longer white, and samples are no longer statistically independent. As a result, the expected $1/\sqrt{N}$ reduction in noise with integration time breaks down, and further time-averaging does not yield as large improvements in the noise. During typical readout, we operate the clock anywhere between 1 and 5 MHz, with a high duty cycle of 90% and above, as limited by our function generator. The result is that, under typical operation, the frame noise is 65-90 e^-.

4.3.3 Charge Imaging

With the pixel amplifiers and rolling shutter functioning, the next step was to verify the TopmetalSe chip's ability to sense external charge. To do this, an ^{241}Am alpha source was positioned above the sensor in air, at the top of a region with a high electric drift field. In ambient air, alpha particles from the source travel less than 5 cm and generate over 100,000 ion pairs along their paths [84]. By placing the sensor to avoid direct alpha hits, the system instead captures the ionization trails produced by the drifting ions, enabling imaging of the

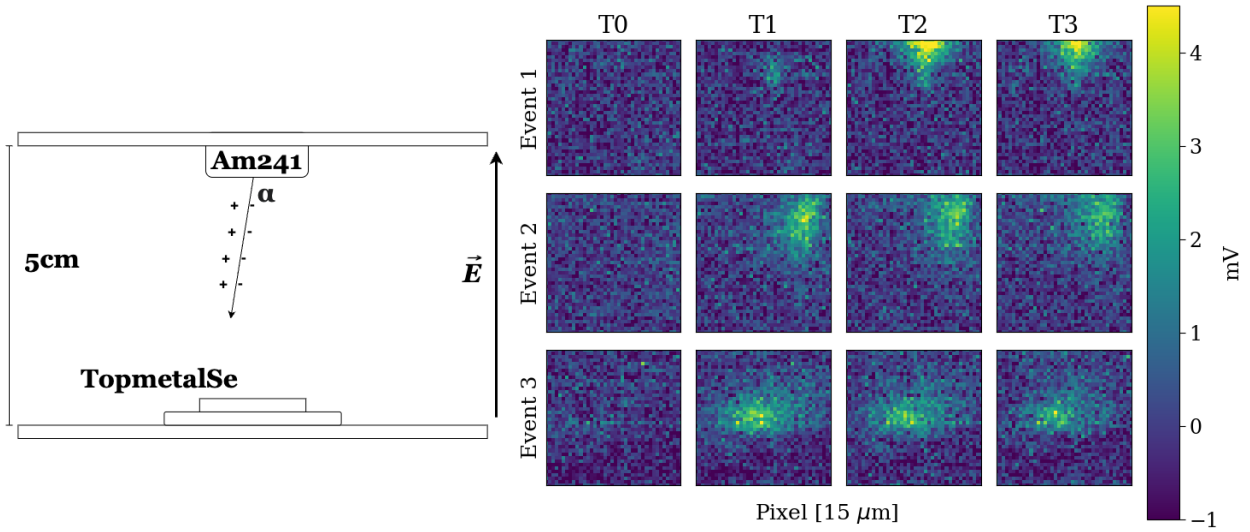

Figure 4.10: **Alpha Drift Imaging with TopmetalSe** Left: Experimental setup showing α emission from an ^{241}Am source drifting under an electric field toward a Topmetal-Se detector. Right: Time-resolved pixel maps for three events (rows) across four time slices (T0–T3), illustrating the evolution and signal decay of the drifting charge cloud as it approaches the sensor.

resulting charge tracks. A diagram of the test setup is shown in Figure 4.10 (left).

The result is shown in Figure 4.10 (right). In this test, four consecutive frames were captured per readout event. Due to the baseline variation of pixels, each frame is constructed by subtracting a baseline frame, taken as the mean of a set of unexposed images. Data was taken with a long decay time on the CSA so as to maximize the signal strength. The events shown were selected to clearly show the arrival of drifting ions at the pixel array. That is, frame 0 shows no charge, and frame 1 reveals the appearance of an ion cloud. Because of the long decay times of the CSA, subsequent frames demonstrate a combination of CSA decay and additional ion drift. Frames were acquired using a 2.5 MHz pixel clock, corresponding to a frame rate of 250 Hz. The images demonstrate the ability of TopmetalSe to image charge tracks via the pixel collection electrode.

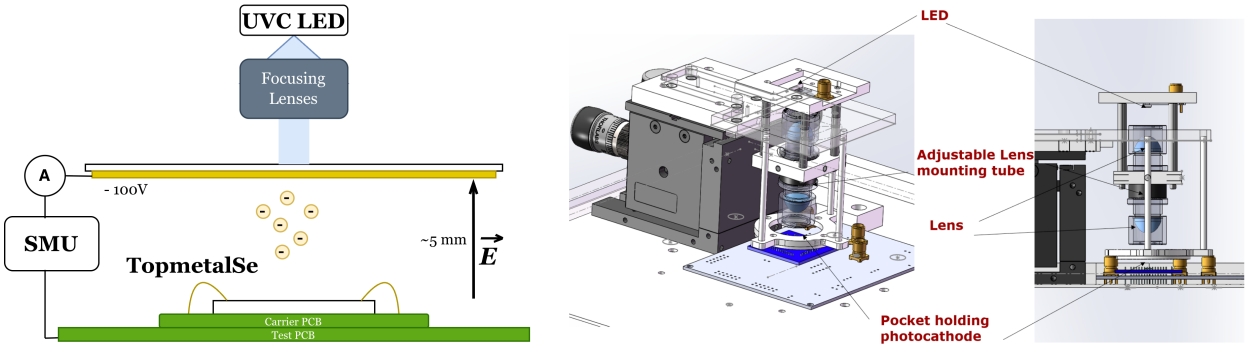

Figure 4.11: **Photoelectric Test Stand** A UVC LED is focused onto the photocathode using an adjustable lens assembly positioned approximately 3 mm above the TopmetalSe device. The electric field ($\vec{E}$) drives photoemitted electrons/ions toward the sensor surface, and the resulting current is monitored using a source measurement unit (SMU). The adjustable lens tube allows fine focusing of the UV beam onto the photocathode. TopmetalSe is attached and wirebonded below on a carrier PCB.

4.3.4 Direct Charge Calibration

Lastly, we performed a calibration of the charge conversion gain using ions generated via the photoelectric effect. The photoelectric effect refers to the emission of electrons from a material upon exposure to photons with energy exceeding the material's work function [10]. We exploit this phenomenon to inject a known quantity of charge into the pixel array for calibration.

The experimental setup, illustrated in Figure 4.11, consists of a photocathode charge source positioned ∼5 mm above the pixel array. The source comprises a 235 nm UVC LED from Crystal IS, focused onto a 7 nm gold layer sputtered onto a 200 μm sapphire substrate. Gold is selected for its chemical stability in ambient conditions, while sapphire is chosen for its high transmittance in the deep UV range [85], enabling backside illumination of the photocathode and front-side electron emission. A set of high numerical aperture UV-grade fused silica lenses, housed in an adjustable lens tube, is used to tightly focus the LED output and produce a localized charge spot on the array. Live monitoring via TopmetalSeDrone allows for precise placement and focusing. Biasing of the photocathode

is achieved using a Keithley 2460 Source Measure Unit (SMU), which provides both voltage and picoamp precision current readout. Triaxial cables are employed to enable low-leakage current measurements, utilizing a driven guard to reduce parasitic currents.

In ambient conditions, the emitted photoelectrons travel a short distance before undergoing either two-body or three-body electron attachment with molecules in air:

$$e^- + O_2 \rightarrow O_2^- \tag{4.15}$$

$$e^- + O_2 + O_2 \rightarrow O_2^- + O_2 \tag{4.16}$$

$$e^- + O_2 + N_2 \rightarrow O_2^- + N_2 \tag{4.17}$$

This reaction dominates at low energies (< 1eV) [86–89]. The drift velocity of O_2^- ions is relatively slow [90, 91], giving drift times $\mathcal{O}(1)$ ms. This is well within our long CSA integration window ($\mathcal{O}(10)$ ms), ensuring all ions contribute to the measured signal. Moreover, electron detachment from O_2^- becomes relevant at these timescales at much higher values of reduced fields [92], over two orders of magnitude above our operating value ($E/p \approx 0.26$ V/[cm Torr]). Thus, electron detachment of O_2^- is negligible over its drift, ensuring that the total induced signal matches the total photoemitted charge.

To calibrate our results, we perform an independent measurement of this effect without TopmetalSe. We designed a measurement electrode with the same dimensions as the active pixel array of TopmetalSe, placed onto a carrier PCB which can be mounted in the same position as TopmetalSe. We measure the current induced by the drift of ions through our system by placing the metal plate anode at the `FORCE Hi` terminal of the SMU and biasing at positive voltages, and the photocathode at `FORCE Lo`. To account for leakage through the system, we subtract off a measurement done with the bias on and the LED off from the LED on measurement. The result is shown in Figure 4.12.

During standard TopmetalSe operation, the photocathode is biased to negative voltages relative to the chip and board ground. Practically, this is achieved by connecting the photocathode to the `FORCE Hi` terminal of the SMU, while `FORCE Lo` is tied to the board ground. This configuration enables direct biasing and measurement of the emitted photocurrent with

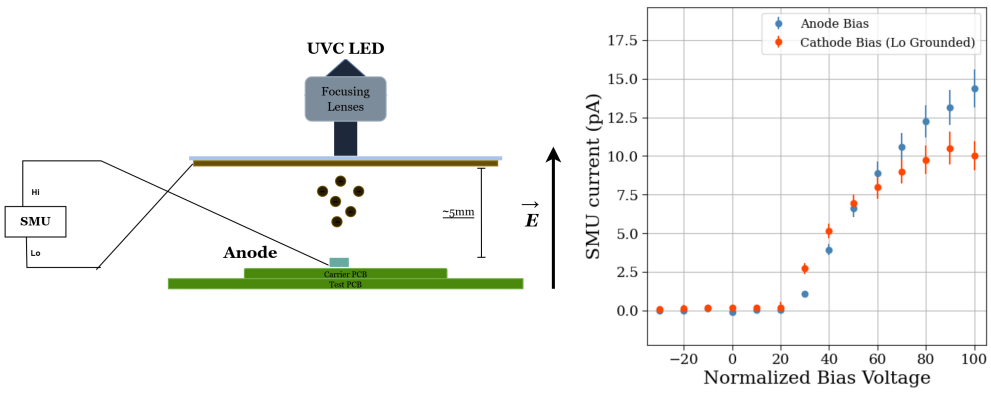

Figure 4.12: **IV Measurement of Photo-Induced Ion Drift.** Schematic (left) and corresponding IV measurement (right) performed using a metal collection anode with the same dimensions as the TopmetalSe pixel array. Measurement is performed both with the anode biased (isolated SMU configuration) and with the cathode biased (identical to the Topmetal-Se setup), yields systematically lower measured current due to parasitic return paths through the shared ground of the SMU.

TopmetalSe in place, mitigating variations in ambient and mechanical conditions that would arise from replacing the chip with a metal anode. However, because the SMU terminals shares ground with the rest of the electronics, the circuit is not isolated, leading to unreliable current measurements [93]. Since the emitted charge drifts toward 0 V and `FORCE Lo` is not isolated, alternative current paths can form within the setup, effectively bypassing part of the measured signal. To quantify this effect, we measured the IV curve with both the system ground and a metal collection anode tied to `FORCE Lo`, and again with `FORCE Lo` disconnected from the system ground, all while biasing the photocathode negatively through `FORCE Hi`. In both configurations the measured current was unchanged, as the SMU LO, cable shields, and instrument chassis all are kept at 0 V. The results, shown in Figure 4.12, indicate a (1.4 ± 0.2)-fold reduction in measured current when biasing the photocathode at -100 V compared to an equivalent configuration with the anode at +100 V, an effect that must be corrected for in calibration measurements.

To measure the TopmetalSe response, we pulse the LED, allowing TopmetalSe to capture discrete bursts of charge rather than a continuous signal. With assistance from T. Van Wechel

and D. Peterson, a custom fast-pulsed LED driver circuit was developed, triggered via 5V TTL pulses from a function generator. The LED is operated near its maximum rated forward current ($\lesssim$ 50mA). To avoid pileup during the pixel decay time, the LED is pulsed at 2Hz.

Single Pixel Waveforms

In order to understand signal formation in TopmetalSe, we first examine single-pixel waveforms under pulsed charge illumination. Figure 4.13 shows the response of a single pixel under a 4 ms illumination pulse, averaged over 10 pulses to reduce noise and smooth the signal.

In contrast to the earlier test-pulse configuration using the guard ring, where the CSA output represented the integration of a delta-like current injection, the rectangular LED pulse produces a finite-duration current input. Consequently, the CSA voltage response no longer corresponds to the instantaneous integration of a delta function, but instead follows

$$V_{\text{out}}(t) = \begin{cases} \dfrac{Q_{in}\tau}{GT_p}\left(1 - e^{-t/\tau}\right), & 0 < t < T_p, \\ \dfrac{Q_{in}\tau}{GT_p}\left(1 - e^{-T_p/\tau}\right) e^{-(t-T_p)/\tau_f}, & t > T_p, \end{cases} \tag{4.18}$$

where Q_{in} is charge injected during a pulse of width T_p. The first term represents the charging of the feedback capacitor during the current pulse, while the second term describes its exponential decay once the input current is removed. This function holds only under the assumption of the small pixel effect.

The single-pixel waveform shown in Figure 4.13 reveals several additional features. The LED drive pulse is overlaid for comparison. During LED operation, a small perturbation appears in the waveform, likely arising from capacitive coupling between the LED driving line and a TopmetalSe bias or output connection. This artifact does not correspond to real signal in the CSAs, as evidenced by the lack of a decay component. We account for this in fitting the waveform by including a transient offset term that is added during the LED pulse interval.

We also observe a field-dependent delay between the LED on/off transitions and the onset/end of CSA integration. This delay is attributed to the finite drift velocity of the photo-generated ions. To capture this behavior, an additional fit parameter is introduced to represent the ion drift delay, resulting in the full model:

$$V(t) = \begin{cases} V_0, & t \leq T_{on}, \\ V_0 + \delta v + \frac{Q_{in}\tau}{GT_p}\left(1 - e^{\frac{-t+[T_{on}+\Delta T]}{\tau}}\right), & T_{on} < t \leq T_{on} + T_p, \\ V_0 + \frac{Q_{in}\tau}{GT_p}\left(1 - e^{\frac{-t+[T_{on}+\Delta T]}{\tau}}\right), & T_{on} + T_p < t \leq T_{on} + T_p + \Delta T, \\ V_0 + \frac{Q_{in}\tau}{GT_p}\left(1 - e^{-\frac{T_p}{\tau}}\right) e^{\frac{-t+[T_{on}+\Delta T+T_p]}{\tau}}, & t > T_{on} + T_p + \Delta T. \end{cases} \tag{4.19}$$

where T_{on} is the start of the LED pulse, ΔT is the drift time, and δv is the slight signal offset introduced by LED coupling. An interesting measurement which comes out of this is the ion mobility, which is done by extracting the ΔT for single pixel waveforms at different bias voltages, shown in Figure 4.13. For an approximate drift gap of 5 ± 1 mm, we measure an ion mobility of 2.6 ± 0.5 cm^2/Vs, in agreement with other measurements [87, 88, 91]. The observed timing capabilities further illustrates the small-pixel effect in TopmetalSe, where each pixel responds exclusively to the drift of charge directly above its own electrode.

Frame Reconstruction

To reconstruct single-pixel waveforms over an entire frame during rolling-shutter readout, we must adapt the model to account for the rolling-shutter readout. In standard operation, pixels are read sequentially at a clock frequency of 2.5 MHz, corresponding to a full-frame rate of 250 Hz. This results in an effective sampling rate of only 250 Hz per pixel, which is insufficient to resolve the pixel response to the LED pulse. To overcome this limitation, we acquire multiple frames with the LED pulse triggered at different time offsets relative to the start of the array readout. By combining single-pixel waveforms from 10 such offsets, each spaced by one-tenth of a frame, we effectively increase the sampling rate by a factor of ten,

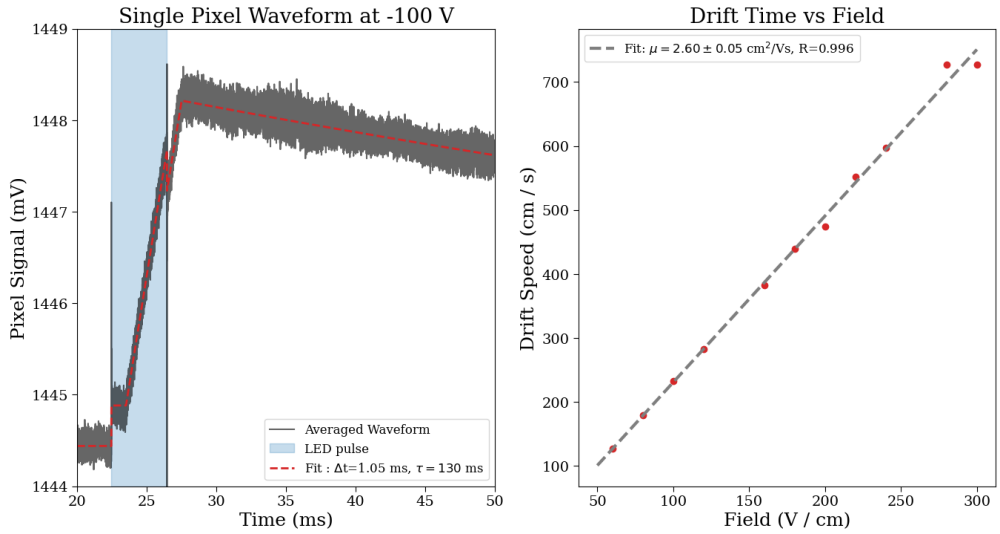

Figure 4.13: **Single Pixel Response to Ion Pulse.** (Left) Averaged single-pixel waveform at -100 V showing the integrated ion-drift signal following the LED pulse. The fit includes a delayed exponential rise and decay corresponding to the ion arrival and recombination. (Right) Extracted drift velocity as a function of electric field, yielding an ion mobility consistent with oxygen-ion transport.

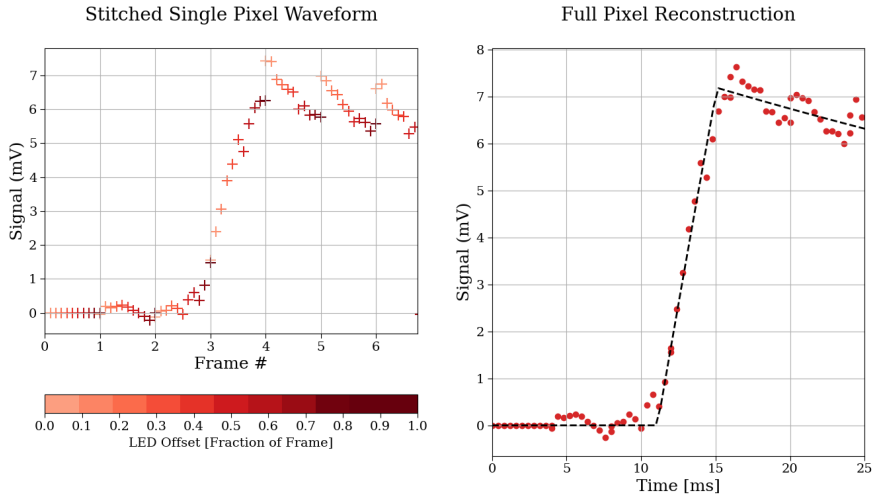

Figure 4.14: **Single Pixel Reconstruction For Rolling Shutter Data.** (Left) Stitched single-pixel waveform constructed from multiple rolling-shutter readouts at different LED trigger offsets to increase sampling rate. Discontinuities in waveform are a result of variations in the injected charge and were corrected by normalizing by the measured current on the SMU. (Right) Reconstructed continuous waveform obtained by aligning, normalizing to the SMU current and fitting the stitched samples, showing the full charge integration and decay behavior of a single pixel.

enabling reliable waveform fitting for individual pixel responses. For each offset, we acquire 1,000 readouts, each consisting of 8 frames.

During this procedure, the photocathode is biased at -100 V, and the SMU current is recorded after every 1,000-frame acquisition to monitor and correct for any drift in the photocurrent due to changes in ambient conditions over the several-hour data collection period. We observe approximately a 12% decrease in the measured current over the course of the run. To account for this, each signal measurement at a given offset is normalized by the relative decrease in the measured current. The reconstructed single-pixel waveform for one representative pixel is shown in Figure 4.14.

To reconstruct the full signal across the array, we first generate an averaged image by averaging all readout events and subtracting the frame immediately before the LED pulse from the frame immediately after. This allows us select a subset of pixels with amplitudes exceeding 0.2 mV, ensuring that only pixels containing a clear signal are included in the fit and avoiding spurious results from noise-dominated regions. We apply the stitching and fitting to this subset of pixels, and the resulting image, shown in Figure 4.15, highlights the improvement of this method over a simple frame-difference approach, which underestimated the total signal due to the relatively long current integration time.

To perform the final calibration, the total signal is obtained by summing the reconstructed waveform amplitudes over all pixels containing charge. The measured SMU current is corrected using the previously determined correction factor and multiplied by the pulse width of 4 ms, yielding a calibrated pixel gain of

$$G = 11 \pm 2 \ \mu\text{V}/e^- \tag{4.20}$$

The dominant contribution to the uncertainty arises from the SMU current measurement. Although the resulting 20% noise uncertainty is relatively high, the measured gain remains consistent with the earlier result and is obtained independently of any assumptions of simulated parasitic capacitance

Surprisingly, increasing the guard ring bias does not enhance signal strength or collec-

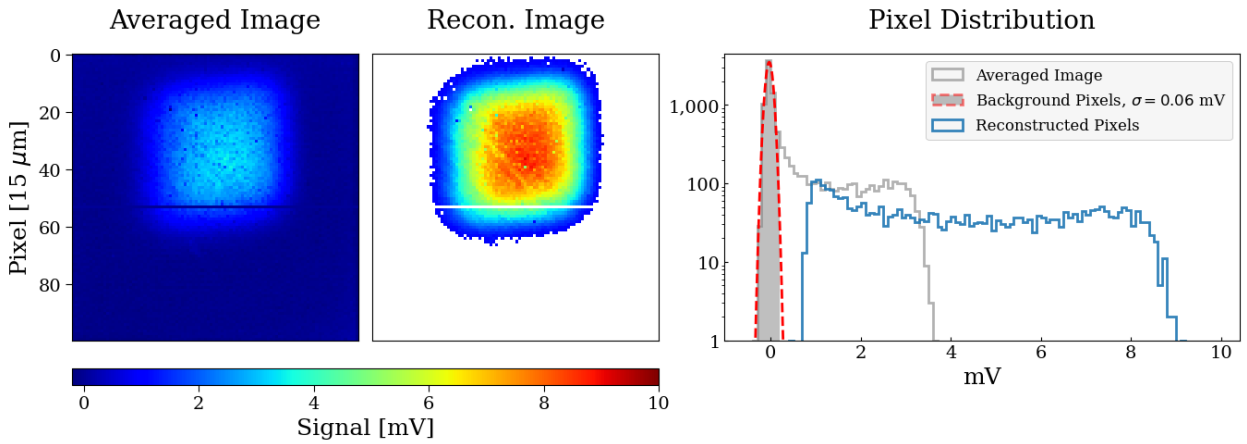

Figure 4.15: **Reconstructed Ion Spot on TopmetalSe.** (Left) Averaged image of the ion-induced signal obtained from frame subtraction. (Center) Fully reconstructed image using stitched single-pixel waveform fitting, showing improved charge recovery and spatial uniformity. (Right) Pixel-level signal distribution comparing the averaged and reconstructed methods.

tion efficiency, in contrast with simulations (Figure 4.3). The measured collection efficiency reaches or exceeds 100%, implying full charge collection even at 0 V guard ring bias. We hypothesize that the intense photoelectron emission ($\mathcal{O}(10^5 e^-)$ per pulse) causes fast ion accumulation on the passivation layer, which modifies the local field configuration to focus charge toward the pixel. This ion layer likely persists between pulses, providing sustained focusing.

4.4 Additional Prototypes & Further Work

There are currently two additional prototypes that have been designed and taped out but have not yet been brought up or characterized. In this section, we describe their designs, current status, additional electronic prototyping efforts, and future prototyping goals.

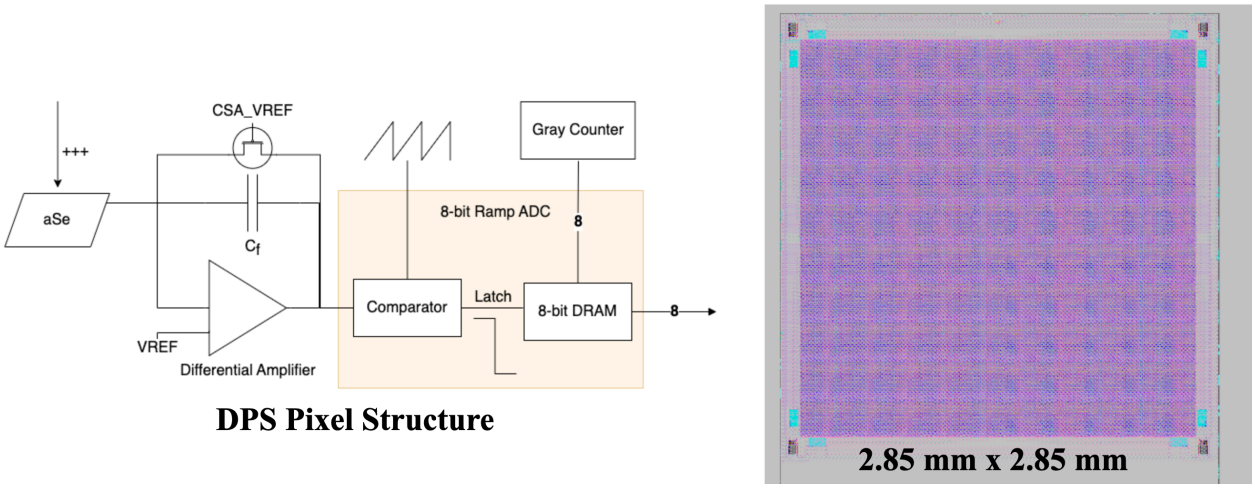

Figure 4.16: **TMSe Future Prototypes**

4.4.1 TopmetalSe — Digital Pixel Sensor

We designed a variant of the TopmetalSe pixel incorporating in-pixel digitization via a ramp-type analog-to-digital converter (ADC), referred to as the Digital Pixel Sensor (DPS), following the architecture introduced in Ref. [94]. The pixel front-end remains identical to the design shown in Figure 4.2, but its output is connected to an in-pixel comparator. This comparator compares the pixel output voltage against a global reference ramp signal distributed across the array. When the ramp voltage intersects the pixel signal, the comparator toggles, and a local digital counter—clocked synchronously with the ramp—is latched to encode the signal amplitude. This architecture enables fully parallel, in-pixel digitization, significantly reducing readout time and improving scalability for high-resolution imaging. The pixel layout is illustrated in Figure 4.16.

The prototype was developed to demonstrate the feasibility and compactness of the DPS architecture within the same pixel footprint as TopmetalSe. It includes several small 3×3 arrays and a few isolated pixels for individual testing. The chips were delivered in September 2023. Since our efforts were focused on TopmetalSe, the devices have not yet been brought up and tested. Future testing will require the design and fabrication of a dedicated readout

board and support hardware.

4.4.2 SNRLxP0

We also developed a larger-format prototype to increase the active area for charge sensing by abutting four TopmetalSe arrays, each with an independent readout channel. To accommodate layout constraints, each sub-array consists of 95×95 pixels, resulting in a total active area of 2.85×2.85 mm^2. The pixel front-end was preserved with minor modifications: we increased the W/L ratio of the row-selection transistor (M12) to improve switching speed and simplified the biasing scheme to reduce the number of bias lines required per pixel.

The SNRLxP0 prototype used an openframe version of the Caravel padframe, omitting the embedded RISC-V SoC in exchange for a larger project area. However, this also required more complex I/O configuration and FPGA interfacing. The design was submitted for tapeout in September 2024. Devices were received September 2025, but have also yet to be tested. Testing will require a custom readout board capable of interfacing with the four-channel output.

4.4.3 Noise Reduction

With Topmetal-II$^-$, we measured a lower ENC of approximately 15 e^- in isolated single-pixel measurements and approximately 23 e^- during full rolling-shutter frame readout. The single-pixel noise reflects the intrinsic performance of the CSA; further reductions in future prototypes could be achieved through continued optimization of the front-end amplifier design, focusing on input device sizing and biasing. In contrast, the increased noise observed during rolling-shutter operation arises primarily from readout-related constraints, such as finite pixel sampling time, front-end bandwidth and clocking capabilities. Future prototypes of TopmetalSe pixels will therefore prioritize co-optimization of the CSA bandwidth and rolling-shutter timing to ensure operation within the white-noise-dominated regime, where predictable noise scaling with integration time can be maintained during full-frame readout. This will require careful simulation of noise spectra and corresponding time-domain response.

Smart Triggering

To replicate the low-noise performance observed in single-pixel tests while reading out the full pixel array, we developed a *Smart Triggering* strategy. Single-pixel measurements have demonstrated that, with integration times exceeding $\mathcal{O}(10)$ μs, we can reliably achieve noise levels < 30 e^-. While such performance is not achievable under a conventional rolling shutter readout, it becomes feasible by integrating only over regions of interest (ROI) identified by a trigger.

As described in Section 4.2.3, the trigger module flags pixels containing significant charge. Once tagged, a slow integration (> 1 μs) is performed over a window surrounding the triggered pixel. Although the row and column switches are sequentially scanned via shift registers, the use of a high-speed clock allows the scan to complete quickly enough to prevent significant signal decay. The associated FPGA logic has been developed and is currently undergoing testing with TopmetalSe.

4.4.4 Future Directions

A key area of development lies in the design of fully-featured pixels for the Selena detector, which will require more advanced digital readout capable of capturing both pulse height and time-of-arrival (TOA) information. A pixel pitch in the 10–15 μm range is necessary to achieve the spatial resolution required for directional ionization track reconstruction and energy resolution. Implementing such functionality at this scale poses challenges, including the integration of low-noise analog front-ends, high-speed digitization, and efficient in-pixel data handling. These developments are essential for realizing a scalable, high-resolution detector architecture suitable for future-generation neutrino physics. Future prototypes will need to strike a balance between pixel pitch, noise and timing resolution, dynamic range, and system-level constraints such as power, data bandwidth and scalability.

Chapter 5

TOPMETAL-SE/ASE HYBRID DEVICES

We integrate amorphous selenium (aSe) with the TopmetalSe sensor to demonstrate its capability for direct charge collection from the selenium layer. This chapter outlines the packaging strategy we developed to enable aSe deposition, along with our testing methodology and results.

5.1 Packaging and aSe Deposition

To overcome limitations encountered in aSe deposition onto the earlier Topmetal-II$^-$ design, we developed a new packaging approach tailored to the TopmetalSe detector. Our initial hypothesis was that the uneven selenium deposition observed in epoxy-encapsulated, wirebonded assemblies distorted the electric field geometry and limited the maximum high voltage (HV) that could be safely applied across the aSe layer. This distortion was likely caused by surface asymmetries introduced by the wirebonds and encapsulant, as well as stray voltages from the wirebonds. To address these issues, we adopted a flip-chip bonding approach.

Flip-chip bonding is a packaging technique in which the chip is mounted face-down onto a substrate using conductive bumps at its I/O pads [95,96], eliminating the need for wirebonds and resulting in a flatter overall package. For our application, the uniform topography provided by flip-chip packaging is intended to the quality of selenium evaporation and enables the application of higher, more uniform electric fields across the detector.

Our interposer design used a 3 cm $\times$ 3 cm sapphire substrate, 200 μm thick. Sapphire was chosen for its excellent dielectric strength and insulating properties, allowing operation at elevated bias voltages [97]. A 2 μm aluminum layer was thermally evaporated and patterned

on the bottom surface to route signals from the central flip-chip area to outer bonding pads. A rectangular window was laser-cut through the sapphire using an LPKF Protolaser, exposing the pixel array to allow direct aSe deposition. To shield the aSe layer from parasitic electric fields, a conductive ground mesh was patterned on the top surface of the sapphire interposer.

We evaluated several interconnect technologies for bonding the chip pads to the interposer. While commercial flip-chip processes typically employ solder bumps and under bump metallization (UBM), these methods are wafer-scale and unsuitable for our diced chips. Instead, we explored gold thermocompression bonding, thermosonic bonding, and conductive epoxy or anisotropic conductive film (ACF) bonding.

In gold thermocompression bonding, stud bumps are formed using a gold wire bonder and compressed under heat and pressure to create solid-state bonds. However, the required parameters often caused pad damage and electrical shorts. Thermosonic bonding, which adds ultrasonic energy to lower bonding force and temperature, showed marginal improvement but suffered from similar reliability issues across both Topmetal-II$^-$ and TopmetalSe.

The most robust solution was conductive epoxy bonding. We used Masterbond EP3HTSDA-2, which is compatible with Hologic's evaporation process. Under a microscope, M. Conde manually dispensed the epoxy onto each interposer pad. Gold stud bumps were first applied to the chip pads using a Westbond 4700E ball bonder. To improve mechanical stability, we added dabs of non-conductive epoxy (a mix of MasterBond EP4UF-80 and EP4TC-80) between the sapphire and inactive chip regions. The mixture was tuned for viscosity to minimize flow while allowing flexibility under pressure.

Alignment and bonding were performed using a Finetech Pico flip-chip bonder, with a low force of 1 N to avoid damaging delicate chip structures. The epoxy was cured using a multi-step thermal profile: 15 minutes at 90°C, 15 minutes at 150°C, and a final 20 minutes at 90°C. This process yielded mechanically and electrically reliable die-level interconnects.

For selenium deposition, we designed a custom jig to secure devices in Hologic's evaporation chamber. The jig, developed by R. Roenhelt and machined by N. Miedema, also

functioned as a shadow mask. To account for possible flip-chip yield losses, the jig accommodated both flip-chip and wirebonded devices. Each slot included a two-piece mask set: one for selenium and one for the electrode layer. For wirebonded devices, chips were mounted on custom PCBs. Unlike prior work, we did not use epoxy encapsulation over the wires, relying instead on the high dielectric strength of aSe to prevent shorts.

In total, we prepared and submitted eight flip-chip packaged devices and three wirebonded devices for selenium and electrode deposition at Hologic. The complete packaging and deposition setup is shown in Figure 5.1. The final stack consisted of a 545 μm amorphous selenium layer topped with a 22 nm chromium electrode. Additionally, Hologic deposited a proprietary hole-blocking layer between the electrode and the aSe to suppress dark current by limiting charge injection from the electrode.

5.2 aSe Detector Testing and Results

The packaged devices are shown in Figure 5.1, and the experimental test stand is shown in Figure 5.2. To apply high voltage (HV), we used a small dab of Graphite Conductive Adhesive 154 (Electron Microscopy Sciences) to secure a 25 μm aluminum bonding wire. This wire was routed to a PTFE post connected to an HV cable. Flip-chip devices were wire-bonded to a carrier PCB, while the wire-bonded devices could be directly plugged into our test board. To prevent HV discharge in ambient air, all testing was conducted inside a vacuum chamber pumped down to $\leq 1 \times 10^{-3}$ mbar.

All wire-bonded packages electrically survived the selenium deposition, indicating that the aSe did not short the exposed wires. However, due to the highly directional nature of thermal evaporation, the wire bonds became uniformly coated with a thin layer of aSe, as evident in Figure 5.1. During HV application, the CAEN power supply drew significantly higher current—on the order of a few µA at 1 kV—compared to typical operation with Topmetal-II$^-$ devices, which drew less than 20 nA at 2 kV. Since this elevated current was not accompanied by any increase in pixel signal, we infer that the current did not reach the pixel array. Instead, it likely flowed through the selenium-coated wire bonds. Prolonged

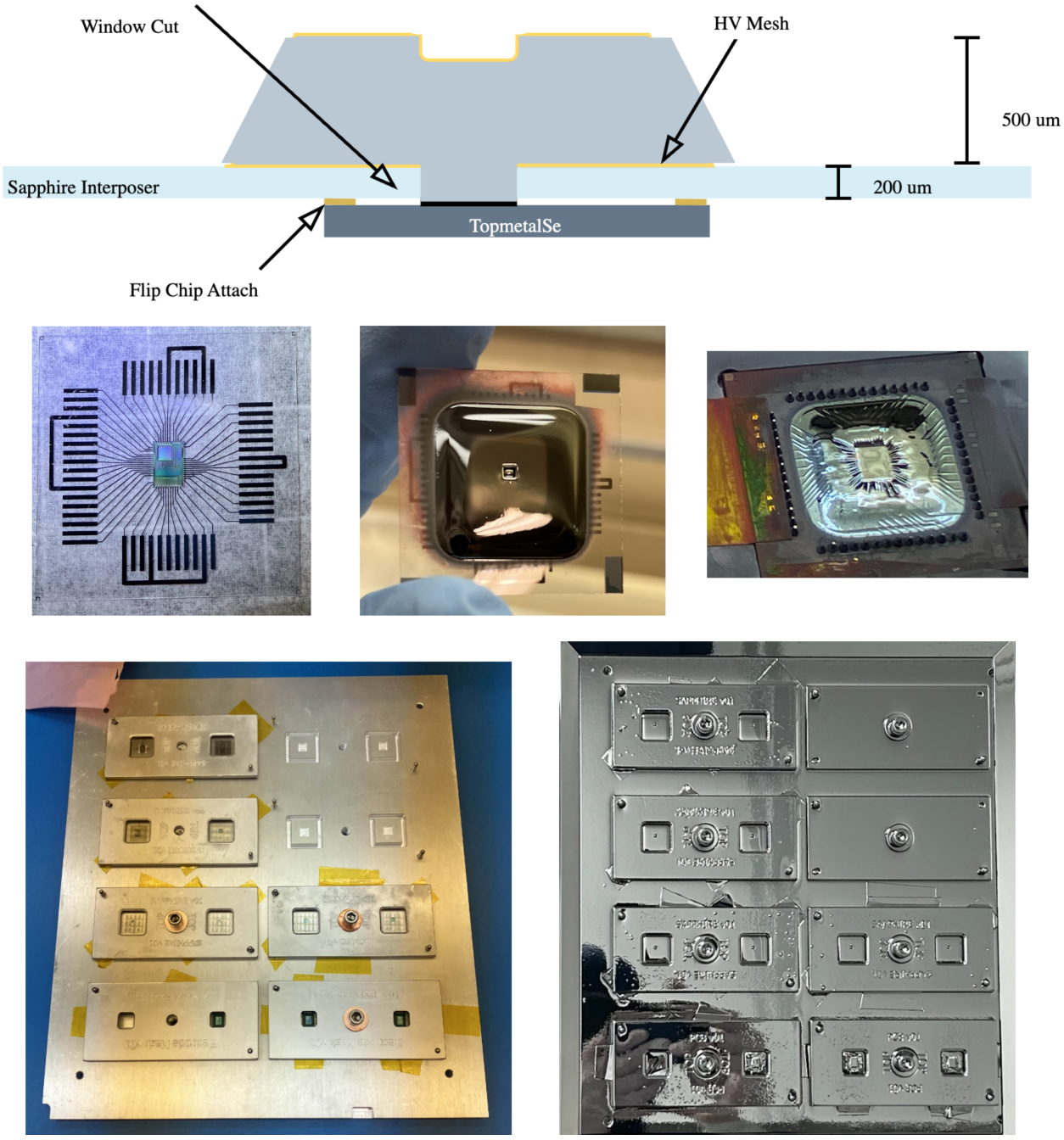

Figure 5.1: **Device Packaging and Deposition of aSe** Top shows flip-chip package concept. Middle shows aSe devices. Left is flip-chip package prior to deposition. Middle shows 545 μm on the flip chip package. Righto shows 545 μm on wire bonded packages. A highly directional deposition results in such sharp features. Bottom shows deposition jig before and after deposition.

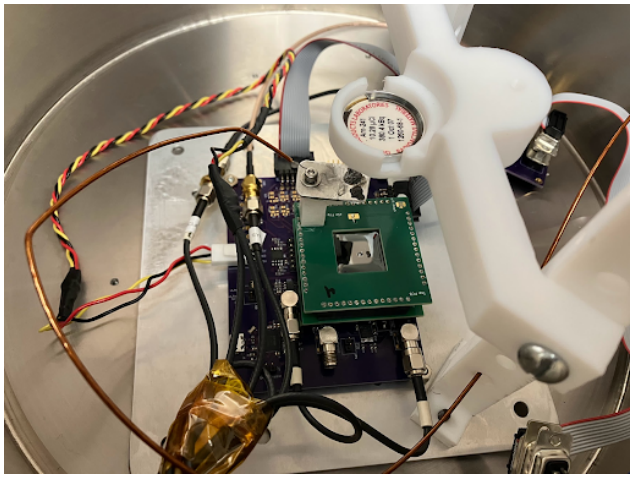

Figure 5.2: **Hybrid aSe/TMSe Device Test Stand** Device is secured and wirebonded to a carrier PCB. White teflon stand acts as a source holder for 1 inch button sources. High voltage is applied to the top electrode via a wire contact secured with conductive paint, while signals are read out through the PCB to external DAQ electronics. The assembly is housed inside a vacuum chamber with cable routing for biasing and readout.

operation under these conditions led to HV trips and permanent damage to the electronics.

Although the flip-chip packages provided more reliable HV biasing, they presented their own challenges. The deposition profile (Figure 5.3) revealed sharp step coverage at the edge of the pocket. As a result, the Cr electrode did not form a continuous film from outside the pixel pocket to the inner aSe surface. Using a probe station, we verified continuity across the outer electrode ($\sim$1 kΩ), but measured an open connection between the electrode outside the pocket and the region inside. This discontinuity occasionally led to HV trips during ramp-up, likely due to large potential differences. We ultimately resolved the issue by adding a second aluminum wire directly into the pocket using another dab of conductive adhesive, establishing a reliable HV contact.

Visual inspection confirms significant inhomogeneity in the aSe deposition. Rather than forming the intended flat 545 μm film, the deposited selenium accumulated into a raised central mound with tapered, sloping sidewalls. This morphology is consistent with directional thermal evaporation, in which the vapor flux arrives predominantly normal to the source and therefore fails to coat vertical or recessed features inside the $\sim$200 μm-deep pocket [98,99]. A

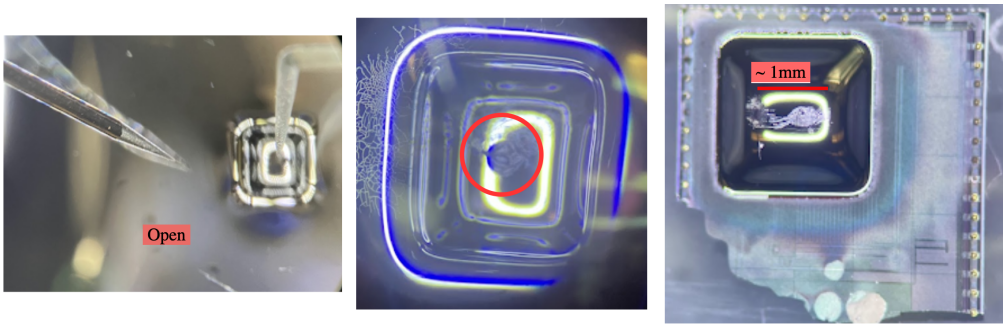

Figure 5.3: **aSe Deposition Details** Left shows probing between aSe pocket and rest of the aSe deposition, demonstrating an open electrical connection between the two regions. Middle shows the HV contact using a 25μm wire and carbon paint to remedy this open connection. Right shows top-down view of exposed pocket deposition after mechanically removing TMSe off off the flip chip assembly. The aSe layer reveals a sloped deposition profile toward the edge of the pocket, indicating poor step coverage across the pocket.

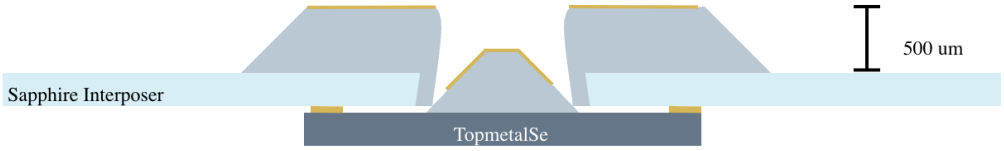

Figure 5.4: **Suspected Cross-sectional aSe Deposition Profile** Due to the geometry of the package, the interposer edges partially shadow the pixel array, producing a tapered aSe profile over the array.

simplified schematic of the suspected cross-sectional deposition profile is shown in Figure 5.4.

We also observed failures caused by the HV aluminum wire being displaced into contact with nearby conductive pins, resulting in shorts and permanent damage. This was resolved by tensioning the wire to eliminate slack and reduce the chance of unintentional contact. With these mitigations, we were able to ramp the HV up to 5 kV, which was the maximum sustainable voltage before frequent trips occurred. Ramp rates above 2 V/s often caused failures. Typical operations voltages were between 2–4 kV for stability, though successful data were also acquired at 5 kV.

The HV power supply current draw remained below 20 nA during stable HV operation. We estimated the aSe sample leakage by analyzing empty frames collected under HV bias, as

most of this is attributed to leakage through the HV wire shielding. Subtracting the baseline pixel values at 0 V from those at applied HV, the DC leakage current into the pixels is given by:

$$I_{ij} = \frac{S_{ij}}{\tau \times G} \tag{5.1}$$

$$I_{tot} \approx \sum_{ij} \frac{S_{ij}}{\bar{\tau}\bar{G}} \tag{5.2}$$

where S is the signal deviation from the baseline in μV, τ is the decay time and G is the gain in e^-/μV. We summed over all pixels using average values of τ and G for simplicity. Leakage appears concentrated at the array's edges and corners, which we attribute to thinning and asymmetry in the aSe near the pocket edges. We calculate the estimated resistivity by isolating our study to the center of the array:

$$\rho = \frac{5 \text{ kV}}{2 \text{ pA}} * (1 \times 1) \text{ mm}^2/545 \ \mu\text{m} \approx 2 \times 10^{12} \Omega\text{m} \tag{5.3}$$

approximately one order of magnitude lower than values previously reported for Hologic samples, which were measured at much higher electric fields of $\sim$40 V/μm [69]. However, this discrepancy is not concerning and remains consistent with typical commercialized aSe dark-current behavior at these fields [100].

5.2.1 Ionization

To test ionization detection, we positioned a 1-inch radioactive button source $\sim$ 5 mm above the device. As in previous tests with Topmetal-II$^-$, we used both a ^{90}Sr beta source and a ^{57}Co gamma source (see Section 3). Devices were biased for long decay times and low noise, enabling the trigger system described in Section 4.2.3. HV was ramped between 2–5 kV (fields of 3.7–9.1 V/μm). Higher fields improved SNR and track visibility. Data were acquired using a Tektronix MSO56 at 250 MS/s, recording 4 frames per event (1–2 pre-trigger). We subtracted the first (baseline) frame from the second (signal) frame to generate event images.

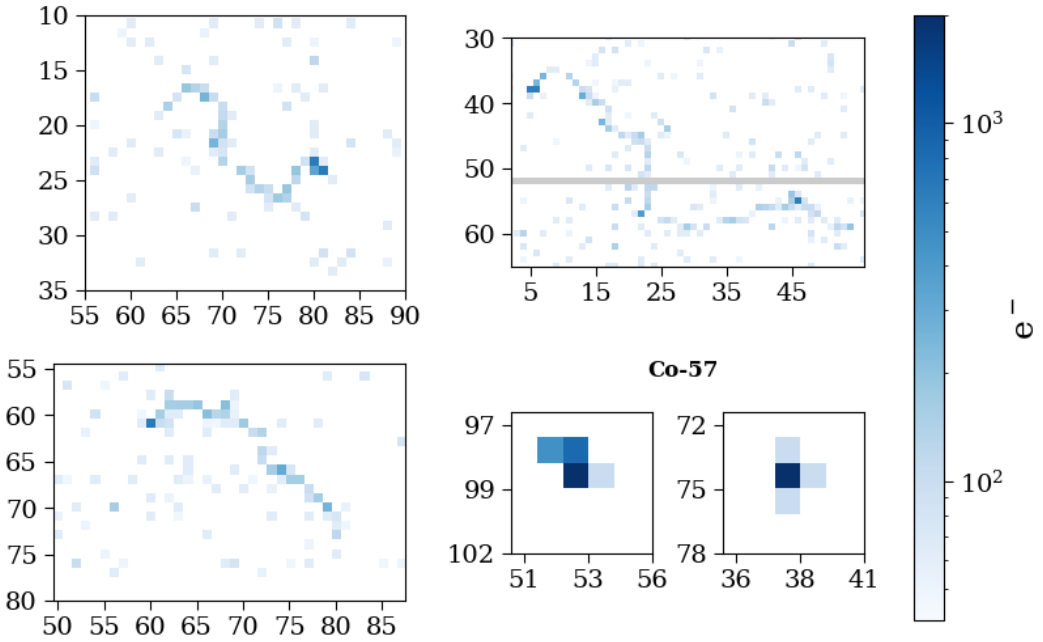

Figure 5.5: **Ionization Tracks in aSe coupled TMSe** : β tracks taken with a ^{90}Sr source. Bottom right two are particularly feature-rich energy depositions from a ^{57}Co γ source. Pixels below 1σ of the baseline are hidden.

Figure 5.5 shows ^{90}Sr beta events, highlighting the enhanced spatial resolution relative to Topmetal-II$^-$. Whereas tracks previously spanned < 10 pixels, TopmetalSe events extend over 40 pixels, with clear Bragg peaks near track endpoints. Despite higher noise (see Section 4.3.2 and smaller pixel size reducing SNR, these tracks demonstrate the superior spatial resolution of the system.

For ^{57}Co, representative tracks are also shown in Figure 5.5. The 122 keV gammas are primarily absorbed via the photoelectric effect, transferring most of their energy to a K-shell photoelectron (binding energy $\sim$13 keV). Based on the CSDA range, ionization spans approximately 15–20 μm, typically yielding 1–2 pixel clusters [82].

For spectral analysis, we applied a threshold of 3σ above baseline to isolate significant signals. We then clustered pixels within a 2-pixel radius of the highest signal pixel and summed them to reconstruct the energy of the event. We varied the applied high voltage (HV) and guard ring (guard ring) bias to study changes in spectral shape and charge col-

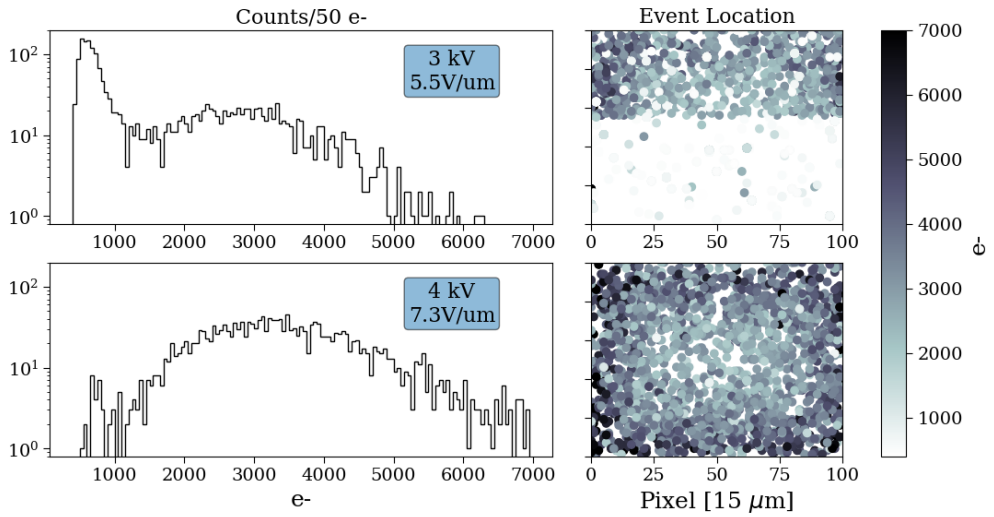

Figure 5.6: **Energy and Spatial Distribution of ^{57}Co Events** at two different HV parameters. Left shows energy spectra while right shows the event locations, colored by their energy. There is no obvious photoabsorption present in the energy spectra. The spatial distribution show large spatial asymmetry. At lower HV, this is seen as a higher fraction of events near the top of the sensor, while at higher HV, the preference of events is towards the edge, where the aSe is thinner. For reference, the expected ^{57}Co line is at 1667 at 5.5 V/μmand 2220 electrons at 7.3 V/μm.

lection efficiency. While HV was increased up to 5 kV (corresponding to 9.1 V/μm) with the guard ring held at 0 V, guard ring bias was swept from 0 V to 100 V at fixed HV = 2 kV. Simulation results (Figure 4.3) indicate corresponding charge collection efficiencies of approximately 30%, 50%, 80%, 95%, and 100%. guard ring biases above 100 V introduced anomalies in the pixel array readout and were thus avoided.

The resulting spectra are shown in Figure 5.6. No distinct photoabsorption peak was observed. Similar to results from Topmetal-II$^-$, we found anisotropic spatial distributions of events, with higher energy depositions preferentially occurring near the edges of the array. However, in TopmetalSe devices, the anisotropy exhibited stronger asymmetry in the x–y distribution, with a consistent bias toward one side or corner, depending on the device. As HV increased, events became more evenly distributed, although edge-focused behavior remained visible. Cuts based on event location did not yield any clear improvement in the spectral shape.

Notably, we observed little change in spectral shape with varying guard ring bias. As in the photoelectric testing, we suspect that charge accumulation on the pixel passivation layer may shape the electric field sufficiently to achieve high collection efficiency. In this case, the accumulated charge likely results from continuous leakage current. Thus, we infer that the observed spectral shape is dominated by field anisotropy caused by uneven aSe deposition. Figure 5.7 shows spectra acquired at increasing guard ring bias with a fixed HV of 2 kV, confirming minimal variation in collection efficiency. These data also show pronounced spatial anisotropy in the event distribution at lower HV values.

5.3 Discussion of Results

The TopmetalSe detectors coupled with amorphous selenium (aSe) demonstrated marked improvements in spatial resolution compared to earlier Topmetal-II$^-$ implementations. The ability to image extended ionization tracks with visible Bragg peaks from ^{90}Sr beta particles highlights the benefit of combining fine-pitch CMOS sensors with a thick, high-Z photoconductive layer. While the resolution gain is partially offset by increased noise and smaller

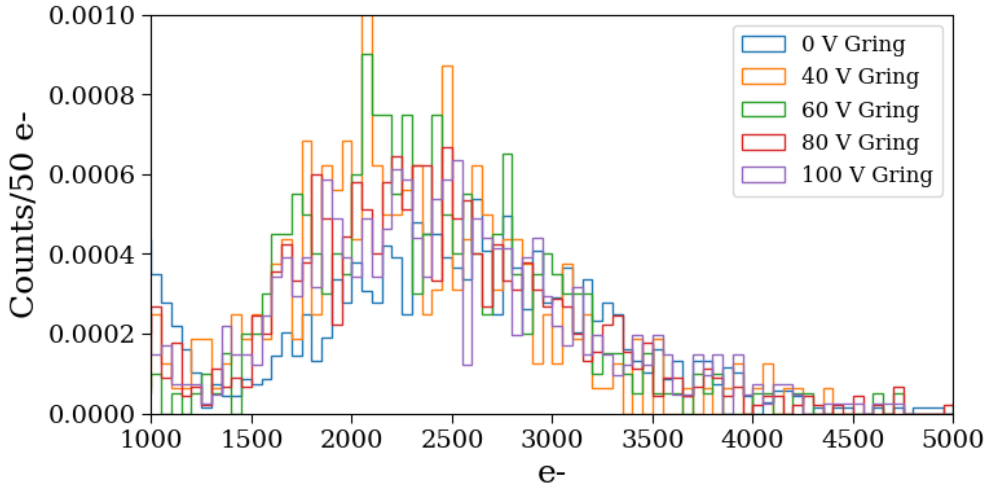

Figure 5.7: **^{57}Co Event Spectra at 2 kV at Increasing Guard Ring Biases** Expected ^{57}Co line is at 1200 electrons. All data runs were acquired for the same duration.

pixels, the improved event morphology and track length are significant for directional and spectral studies.

However, reliable high-voltage (HV) operation presented notable engineering challenges. While flip-chip devices allowed for more stable biasing than wire-bonded packages, they still suffered from the effects of directional aSe deposition. The sharp geometry at the window cut created discontinuities in the chromium electrode coverage, preventing continuous HV contact across the aSe surface. This led to potential differences and occasional HV trips, which we resolved by introducing a secondary contact wire inside the pocket. Wire-bonded devices, on the other hand, exhibited high leakage currents due to selenium coating the wires themselves. This resulted in substantial current draw without corresponding increases in pixel signal, suggesting parasitic currents along the wires. In both cases, improper HV application often led to irreversible damage, emphasizing the importance of proper HV contact.

Spatial anisotropies in event distributions were also consistently observed across devices, with preferential signal clustering near edges or corners of the array. This behavior can again be traced back to the nonuniform aSe deposition profile, where the central region is flat and the field lines are more uniform, while edges suffer from increased field strength and thinner

selenium coverage. As HV increases, this anisotropy diminishes somewhat due to stronger overall fields, but it does not disappear, indicating that field shaping strategies and improved deposition uniformity will be critical for future optimization.

We also suspect that the combined effects of deposition geometry and nonuniform field configuration significantly distort the measured energy spectra. As a result, even when restricting our analysis to a localized region within the detector array, we are unable to resolve a clear photoabsorption peak from the ^{57}Co gamma source. This suggests that spatial nonuniformities in the detector response persist even at small scales, further emphasizing the need for more uniform material deposition and field engineering.

In the case of the flip-chip TopmetalSe devices, the absence of wirebonds eliminates the possibility that wirebond-related field distortions are responsible for the observed spatial anisotropy in the event distribution. This suggests that the anisotropy arises from a different mechanism. One possible explanation is that the aSe deposition on the earlier Topmetal-II$^-$ devices was similarly influenced by the directional nature of thermal evaporation. The devices are shown in Figure 3.1, where, in the pre-deposition Topmetal-II$^-$ devices, the epoxy edges form a sharp pocket at the pixel array edges, similar to Figure 5.4. As a result, we observe a slight ramp in the aSe thickness near the transition region between the pixel array and the surrounding epoxy edge. Although this ramp is less pronounced than in the TopmetalSe devices, it still results in a gradual reduction in selenium thickness and an associated increase in electric field magnitude due to the reduced drift length.

Interestingly, we found little dependence of the gamma-induced spectra on guard ring (guard ring) bias. Despite simulations suggesting that guard ring bias should significantly improve charge collection efficiency, the spectral shape remained qualitatively unchanged even as the guard ring was biased up to 100 V. This behavior could be explained by passive charge buildup on the pixel passivation surface, induced by steady leakage current, which may generate internal field gradients sufficient to guide charge carriers effectively. This phenomenon was also observed in photoelectric testing, further suggesting that the field distribution within the detector is shaped more by accumulated surface charge and deposition

geometry than by external guard ring bias.

5.3.1 Further Work

Future iterations of aSe-coupled CMOS detectors will require continued improvements in both the uniformity of the aSe deposition and the reliability of high-voltage (HV) application. In general, detector performance improved with increasing HV, as the enhanced electric field strength led to better charge collection, improved signal-to-noise ratio (SNR), and greater spatial uniformity in event distributions. However, stable HV operation remains a challenge due to risks of dielectric breakdown, leakage current through surface irregularities, and localized field enhancements caused by nonuniform deposition. One route to achieving stability is through the use of thinner aSe layers, which reduce the required bias voltage and minimize the chance of field-induced damage, which comes at the cost of reduced gamma-ray detection efficiency due to the shorter absorption path. Alternatively, increasing the deposition area can reduce the severity of edge effects and improve overall uniformity. Work in Ref. [101] demonstrated successful single-photon counting using a CMOS detector coupled to aSe with a thinner aSe layer and a large-area deposition.

An ideal CMOS package would feature a planarized surface in which the active pixel array is flush with a surrounding substrate, such as a sapphire interposer. This configuration enables more uniform aSe deposition over a large area while minimizing surface topography that can lead to step coverage issues and electric field nonuniformities. It should be noted taht commfercial flat-panel aSe detectors, such as those from Hologic, routinely achieve uniform deposition over $\mathcal{O}(10-100)$ cm^2, illustrating that large-area aSe coating is feasible over planar surfaces. To this end, we are exploring the use of conductive inks and printable materials to fabricate planar, low-profile contacts that can bridge from the sensor surface to a surrounding support structure and electronics [102]. Such approaches offer the potential for simplified packaging and better mechanical and electrical integration for larger area arrays. It should be noted that such packaging challenges are largely confined to the R&D phase. At the wafer level, access to advanced capabilities such as through-silicon vias (TSVs) can

effectively mitigate these issues.

Further investigation is also required into the role of guard ring (guard ring) biasing and the ability to focus field lines into the active region. While we did not observe a measurable effect from guard ring biasing in this work, there is no fundamental reason why field shaping should not influence charge collection. It is possible that surface charge or leakage-induced charging may have masked any additional influence from the guard ring potential. Work in Ref. [103] explored a similar "field-focusing" strategy, but was unable to make notable measurements with their devices. Controlled measurements across varying device geometries may be necessary to fully understand and isolate these effects. One example is to fabricate simple arrays of electrodes with varying geometries and minimal readout complexity. For example, all electrodes of a given geometry could be connected and readout as a single channel. A single die could include multiple such arrays, with each array containing "pixels" (electrodes) of distinct geometries. This would facilitate straightforward aSe deposition and could enable basic spectral characterization.

Chapter 6

CONCLUSION

The work presented in this thesis contributes to the development and characterization of hybrid amorphous selenium (aSe)–CMOS detectors for rare event searches, with a particular focus on neutrinoless double beta decay ($0\nu\beta\beta$) in ^{82}Se. The proposed detector concept, named *Selena*, combines the high-resolution imaging capabilities of CMOS pixel arrays with the ionization and decay properties of amorphous ^{82}Se, offering a promising technology for topological event reconstruction and background suppression.

6.1 Summary of Contributions

In Chapter 1, we outlined the motivation for studying $0\nu\beta\beta$ decay, which serves as a unique probe into the Majorana nature of neutrinos, lepton number violation, and the absolute neutrino mass scale. We reviewed the theoretical framework underlying the search, including neutrino oscillations, the seesaw mechanism, and the effective Majorana mass parameter $\langle m_{\beta\beta} \rangle$.

Chapter 2 described the Selena detector concept, which employs stacked detector modules consisting of enriched aSe layers deposited directly onto large-area CMOS pixel arrays. We detailed the ionization physics of aSe, including carrier transport, trapping, recombination, and diffusion. We introduced a simulation framework combining `Geant4` charge deposition, analytical diffusion modeling, and COMSOL-based weighting potential calculations to model charge induction and pixel response. A novel depth and energy reconstruction algorithm demonstrated the Selena detector's capabilities.

Chapters 3 and 4 detailed the design, testing, and evolution of the Topmetal series of pixel sensors. Topmetal-II$^-$ was used as an initial proof-of-concept for coupling CMOS pixels

to aSe for ionization imaging. TopmetalSe advanced this work by implementing finer pitch pixels, improved top metal pixel geometry, and in-pixel digitization circuits, all critical for scaling to large-format arrays. Characterization confirmed successful charge collection and demonstrated spatially resolved charge imaging.

In Chapter 5, we demonstrated the integration of TopmetalSe devices with thermally evaporated aSe, including the development of a flip-chip compatible packaging approach. We investigated the impact of high voltage biasing, and guard ring bias on signal uniformity and collection efficiency. Imaging of β and γ events validated the expected track morphology, and energy spectra from ^{57}Co sources confirmed basic ionization detection performance.

6.2 Scientific Outlook

This work establishes the feasibility of aSe-CMOS hybrid detectors for rare event physics. We showed that with appropriate detector geometry and high field operation, hole-dominated unipolar sensing can be realized in aSe films exceeding 500 µm in thickness. The low electronic noise and small pixel pitch of the CMOS readout arrays enabled detailed track topology reconstruction, opening the door to powerful background discrimination techniques.

Simulations based on the developed detector model project that a 100 ton-year exposure with Selena could achieve a discovery sensitivity to $0\nu\beta\beta$ in ^{82}Se with a half-life sensitivity between 2.3×10^{27} years and 9.6×10^{27} years, corresponding to $\langle m_{\beta\beta}\rangle \sim$ 10–28 meV. This level of sensitivity would fully cover the inverted mass ordering regime and begin to probe normal ordering. Beyond $0\nu\beta\beta$, the detector's imaging and temporal resolution enable additional science targets, including solar neutrino spectroscopy and sterile neutrino oscillation studies with artificial sources.

6.3 Future Directions

Several avenues remain for future investigation and development:

- **aSe Integration at R&D and Large-Scale:** Development of aSe coupling at the

R&D Scale (individual dies) remains a packaging and fabrication challenge. While larger arrays will prove easier in terms of aSe deposition, they will also present significant hurdles in balancing dead space, power consumption and increased readout complexity

- **Event reconstruction:** Track topology reconstruction would benefit from additional approaches, incorporating more advanced branch handling for tracking and additional techniques for z_0 estimates. These improvements would directly benefit the energy resolution and discovery capabilities of Selena.

- **High Voltage** Stability in HV application is a challenge and will be an increasing challenge at thicker aSe layers.

- **Background validation:** Experimental verification of background rejection efficiencies using tagged α, γ, and β sources is needed to validate the expected suppression factors and tune event selection algorithms.

- **Electronics development:** Continued development of in-pixel digitization, power consumption, and readout architectures is necessary for scaling to million-pixel arrays while maintaining low noise and minimal power density.

6.4 Final Remarks

This work demonstrates the technical feasibility and scientific promise of hybrid aSe-CMOS pixel detectors for precision ionization imaging. The Selena detector concept represents a new frontier in rare event searches, offering a unique combination of fine spatial resolution, low noise, and material scalability with its target isotope. With continued development, it will enable the next generation of experiments capable of resolving the fundamental nature of the neutrino and answering some of the most profound questions in modern physics.

BIBLIOGRAPHY

[1] Ernest Rutherford. Uranium radiation and the electrical conduction produced by it. *Philosophical Magazine*, 47(284):109–163, 1899.

[2] E. Fermi. Tentativo di una teoria dei raggi β. *Il Nuovo Cimento*, 11:1–19, 1934.

[3] W. Pauli. Letter to the physical society of tübingen. 1930. Unpublished letter proposing the neutrino.

[4] Benjamin J.P. Jones. The physics of neutrinoless double beta decay: A primer. *arXiv:2108.09364 [nucl-ex]*, 2021.

[5] Kevork N. Abazajian, Mario A. Acero, Sanjib K. Agarwalla, et al. Light sterile neutrinos: A white paper. *arXiv e-prints*, 2012.

[6] David J. Griffiths. *Introduction to Elementary Particles*. Wiley, 1987.

[7] Donald H. Perkins. *Introduction to High Energy Physics*. Cambridge University Press, 2000.

[8] H. Bethe. Zur theorie des durchgangs schneller korpuskularstrahlen durch materie. *Annalen der Physik*, 397(3):325–400, 1930.

[9] W. R. Leo. *Techniques for Nuclear and Particle Physics Experiments*. Springer, Berlin, Heidelberg, 1994.

[10] Glenn F. Knoll. *Radiation Detection and Measurement*. John Wiley & Sons, 4th edition, 2010.

[11] LEGEND Collaboration. The large enriched germanium experiment for neutrinoless double beta decay (legend). *AIP Conf. Proc.*, 2334:060003, 2021.

[12] GERDA Collaboration. Final results of gerda on the search for neutrinoless double-β decay. *Phys. Rev. Lett.*, 125(25):252502, 2020.

[13] The DAMIC collaboration. Measurement of the bulk radioactive contamination of detector-grade silicon with damic at snolab. *Journal of Instrumentation*, 16(06):P06019, jun 2021.

[14] nEXO Collaboration. Sensitivity and discovery potential of nexo to neutrinoless double beta decay. *Phys. Rev. C*, 105(1):015501, 2022.

[15] M. Agostini et al. Comprehensive measurement of *pp*-chain solar neutrinos. *Nature*, 562:505–510, 2018.

[16] S. Andringa et al. Current status and future prospects of the sno+ experiment. *Advances in High Energy Physics*, 2016:6194250, 2016.

[17] MINOS+ Collaboration. Search for sterile neutrinos in minos and minos+ using a two-detector fit. *Physical Review Letters*, 122(9):091803, 2019.

[18] M. Goldhaber, L. Grodzins, and A. W. Sunyar. Helicity of neutrinos. *Phys. Rev.*, 109:1015–1017, Feb 1958.

[19] C. L. Cowan, F. Reines, et al. Detection of the free neutrino: A confirmation. *Science*, 124:103–104, 1956.

[20] G. Danby et al. Observation of high-energy neutrino reactions and the existence of two kinds of neutrinos. *Phys. Rev. Lett.*, 9:36, 1962.

[21] K. Kodama et al. Observation of tau neutrino interactions. *Phys. Lett. B*, 504:218–224, 2001.

[22] B. T. Cleveland et al. Measurement of the solar electron neutrino flux with the homestake chlorine detector. *The Astrophysical Journal*, 496:505–526, 1998.

[23] Q. R. Ahmad and others (SNO Collaboration). Measurement of the rate of $\nu_e + d \rightarrow p + p + e^-$ produced by ^8b solar neutrinos at the sudbury neutrino observatory. *Phys. Rev. Lett.*, 87(7):071301, 2001.

[24] R. L. Workman *et al.* (Particle Data Group). Review of particle physics. *Prog. Theor. Exp. Phys.*, 2022:083C01, 2022.

[25] Lincoln Wolfenstein. Neutrino oscillations in matter. *Phys. Rev. D*, 17(9):2369–2374, 1978.

[26] F. et al. An. Neutrino physics with juno. *J. Phys. G*, 43:030401, 2016.

[27] B. et al. Abi. Deep underground neutrino experiment (dune). *arXiv preprint*, 2020.

[28] K. et al. Abe. Hyper-kamiokande design report. *arXiv preprint*, 2018.

[29] Planck Collaboration. Planck 2018 results. vi. cosmological parameters. *Astronomy & Astrophysics*, 641:A6, 2020.

[30] KATRIN Collaboration. Direct neutrino-mass measurement based on 259 days of katrin data. *Science*, 388(6743):180–185, 2025.

[31] Claude Amsler. *Nuclear and Particle Physics*. Taylor & Francis, 1 edition, 2010. Chapter on neutrino masses and the seesaw mechanism.

[32] A. D. Sakharov. Violation of cp invariance, c asymmetry, and baryon asymmetry of the universe. *Soviet Physics Uspekhi*, 34:392, 1991.

[33] Peter Arnold and Larry McLerran. Sphalerons, small fluctuations, and baryon-number violation in electroweak theory. *Phys. Rev. D*, 36:581–595, Jul 1987.

[34] A. et al. Aguilar. Evidence for neutrino oscillations from the observation of $\bar{\nu}_e$ appearance in a $\bar{\nu}_\mu$ beam. *Phys. Rev. D*, 64:112007, 2001.

[35] A. A. et al. Aguilar-Arevalo. Significant excess of electronlike events in the miniboone short-baseline neutrino experiment. *Phys. Rev. Lett.*, 121:221801, 2018.

[36] Daya Bay Collaboration. Search for a light sterile neutrino at daya bay. *Phys. Rev. Lett.*, 113:141802, Oct 2014.

[37] KamLAND-Zen Collaboration. Search for the majorana nature of neutrinos in the inverted mass ordering region with kamland-zen. *Phys. Rev. Lett.*, 130(5):051801, 2023.

[38] CUPID-0 Collaboration. Final result on the neutrinoless double beta decay of ^{82}se with cupid-0. *Phys. Rev. Lett.*, 129:No. 132502, 2022.

[39] S. Dell'Oro, S. Marcocci, M. Viel, and F. Vissani. Neutrinoless double beta decay: 2015 review. *arXiv:1601.07512 [hep-ph]*, 2016.

[40] Majorana Collaboration. Search for neutrinoless double-beta decay in ^{76}ge with the majorana demonstrator. *Phys. Rev. Lett.*, 120:132502, Mar 2018.

[41] EXO-200 Collaboration. Search for neutrinoless double-beta decay with the upgraded exo-200 detector. *Phys. Rev. Lett.*, 123(16):161802, 2019.

[42] CUPID Collaboration. Cupid: The cuore upgrade with particle identification. *Journal of Physics: Conference Series*, 1468(1):012210, feb 2020.

[43] CUORE Collaboration. Search for neutrinoless double-beta decay with the complete cuore dataset. *Phys. Rev. Lett.*, 126:171801, Apr 2021.

[44] CUPID-Mo Collaboration. Final result of the cupid-mo experiment on neutrinoless double-β decay of ^{100}mo. *Phys. Rev. Lett.*, 126:181802, 2021.

[45] LEGEND Collaboration. First results on the search for lepton number violating neutrinoless double beta decay with the legend-200 experiment. *arXiv preprint arXiv:2505.10440*, 2025.

[46] KamLAND-Zen Collaboration. Search for majorana neutrinos with the complete kamland-zen dataset. *Phys. Rev. Lett.*, pages –, Oct 2025.

[47] A. E. Chavarria, C. Galbiati, B. Hernandez-Molinero, Al. Ianni, X. Li, Y. Mei, D. Montanino, X. Ni, C. Peña Garay, A. Piers, and H. Wang. Snowmass 2021 white paper: The selena neutrino experiment, 2022.

[48] Kaitlin Hellier, Emmie Benard, Christopher C. Scott, Karim S. Karim, and Shiva Abbaszadeh. Recent progress in the development of a-se/cmos sensors for x-ray detection. *Quantum Beam Science*, 5(4), 2021.

[49] Saeed Abbaszadeh, Richard A. Glick, and Wei Zhao. Amorphous selenium-based direct-conversion detectors for medical imaging. In *Medical Imaging 2017: Physics of Medical Imaging*, volume 10132 of *Proc. SPIE*, page 101320J, 2017.

[50] Krishna C. Mandal, Sung Hoon Kang, Michael Choi, and Gerald E. Jellison Jr. Amorphous selenium based detectors for medical imaging applications. In F. Patrick Doty, H. Bradford Barber, Hans Roehrig, Larry A. Franks, Arnold Burger, and Ralph B. James, editors, *Hard X-Ray and Gamma-Ray Detector Physics and Penetrating Radiation Systems VIII*, volume 6319, page 63190N. International Society for Optics and Photonics, SPIE, 2006.

[51] X. Li, A.E. Chavarria, S. Bogdanovich, C. Galbiati, A. Piers, and B. Polischuk. Measurement of the ionization response of amorphous selenium with 122 kev γ rays. *Journal of Instrumentation*, 16(06):P06018, June 2021.

[52] S.M. Sze and Kwok K. Ng. *Physics of Semiconductor Devices*. John Wiley & Sons, 3rd edition, 2006.

[53] M. J. Berger, J. H. Hubbell, S. M. Seltzer, J. Chang, J. S. Coursey, R. Sukumar, D. S. Zucker, and K. Olsen. XCOM: Photon Cross Sections Database. `https://physics.nist.gov/PhysRefData/Xcom/html/xcom1.html`, 2010. National Institute of Standards and Technology, Accessed June 2025.

[54] Andy LaBella, Jann Stavro, Sebastien Léveillé, Wei Zhao, and Amir H. Goldan. Picosecond time resolution with avalanche amorphous selenium. *ACS Photonics*, 6(6):1338–1344, 2019.

[55] K. Tanioka. High-gain avalanche rushing amorphous photoconductor (harp) detector. *Nuclear Instruments and Methods in Physics Research Section A: Accelerators, Spectrometers, Detectors and Associated Equipment*, 608(1, Supplement):S15–S17, 2009. Compton sources for X/γ rays: Physics and applications.

[56] Ahmet Camlica, Denny Lee, Hyunsuk Jang, M. Zahangir Kabir, and Karim Karim. Energy resolution of amorphous selenium detectors: conventional vs unipolar charge sensing. In Wei Zhao and Lifeng Yu, editors, *Medical Imaging 2022: Physics of Medical Imaging*, volume PC12031, page PC120310G. International Society for Optics and Photonics, SPIE, 2022.

[57] Mark D. Tabak and Peter J. Warter. Field-controlled photogeneration and free-carrier transport in amorphous selenium films. *Phys. Rev.*, 173:899–907, Sep 1968.

[58] Zhong He. Review of the shockley–ramo theorem and its application in semiconductor gamma-ray detectors. *Nuclear Instruments and Methods in Physics Research Section A: Accelerators, Spectrometers, Detectors and Associated Equipment*, 463(1):250–267, 2001.

[59] Helmuth. Spieler. *Semiconductor detector systems*. Series on semiconductor science and technology ; 12. Oxford University Press, Oxford ;, 2005.

[60] J.D. Eskin, H.H. Barrett, H.B. Barber, and J.M. Woolfenden. The effect of pixel geometry on spatial and spectral resolution in a cdznte imaging array. In *1995 IEEE Nuclear Science Symposium and Medical Imaging Conference Record*, volume 1, pages 544–548 vol.1, 1995.

[61] Munir El-Desouki, M. Jamal Deen, Qiyin Fang, Louis Liu, Frances Tse, and David Armstrong. Cmos image sensors for high speed applications. *Sensors*, 9(1):430–444, 2009.

[62] ALICE Collaboration. The alpide pixel sensor chip for the upgrade of the alice inner tracking system. *Nucl. Instrum. Meth. A*, 824:434–438, 2016.

[63] X. Llopart, J. Alozy, R. Ballabriga, M. Campbell, R. Casanova, V. Gromov, E.H.M. Heijne, T. Poikela, E. Santin, V. Sriskaran, L. Tlustos, and A. Vitkovskiy. Timepix4, a large area pixel detector readout chip which can be tiled on 4 sides providing sub-200 ps timestamp binning. *Journal of Instrumentation*, 17(01):C01044, jan 2022.

[64] V. Sriskaran, J. Alozy, R. Ballabriga, M. Campbell, P. Christodoulou, E. Heijne, A. Koukab, T. Kugathasan, X. Llopart, M. Piller, A. Pulli, J.-M. Sallese, and L. Tlustos. High-rate, high-resolution single photon x-ray imaging: Medipix4, a large 4-side buttable pixel readout chip with high granularity and spectroscopic capabilities. *Journal of Instrumentation*, 19(02):P02024, feb 2024.

[65] Mangmang An, Chufeng Chen, Chaosong Gao, Mikyung Han, Rong Ji, Xiaoting Li, Yuan Mei, Quan Sun, Xiangming Sun, Kai Wang, Le Xiao, Ping Yang, and Wei Zhou. A low-noise cmos pixel direct charge sensor, topmetal-ii. *Nuclear Instruments and Methods in Physics Research Section A: Accelerators, Spectrometers, Detectors and Associated Equipment*, 810:144–150, February 2016.

[66] Alireza Parsafar, Christopher C. Scott, Abdallah El-Falou, Peter M. Levine, and Karim S. Karim. Direct-conversion cmos x-ray imager with 5.6 μm $\times$ 6.25 μm pixels. *IEEE Electron Device Letters*, 36(5):481–483, 2015.

[67] Yun Zhe Li, Mohamed Hamid, Christopher C. Scott, Rhiannon Lohr, Abdallah El-Falou, Peter M. Levine, and Karim S. Karim. A monolithic amorphous-selenium/cmos visible-light imager with sub-9-μm pixel pitch and extended full-well capacity. *IEEE Sensors Journal*, 21(1):339–346, 2021.

[68] O. Bubon, K. Jandieri, S. D. Baranovskii, S. O. Kasap, and A. Reznik. Columnar recombination for x-ray generated electron-holes in amorphous selenium and its significance in a-se x-ray detectors. *Journal of Applied Physics*, 119(12):124511, 03 2016.

[69] Xinran Li and Cristiano Galbiati. *The energy resolution and the energy deposition processes in disordered targets for rare-event searches*. PhD thesis, Princeton University, Princeton, 2021.

[70] R Mankel. Pattern recognition and event reconstruction in particle physics experiments. *Reports on Progress in Physics*, 67(4):553–622, March 2004.

[71] Are Strandlie and Rudolf Frühwirth. Track and vertex reconstruction: From classical to adaptive methods. *Rev. Mod. Phys.*, 82:1419–1458, May 2010.

[72] Alvaro E. Chavarria. Background rejection in highly pixelated solid-state detectors. *AIP Conference Proceedings*, 2908(1):100002, 09 2023.

[73] V. I. Tretyak. Decay0: event generator for initial kinematics of particles in radioactive decays. In *Presentation at MEDEX'15 Workshop*, 2015. Available online at `https://agenda.infn.it/event/9358/attachments/57515/67844/Tretyak_2015.pdf`.

[74] A. S. Barabash. Average and recommended half-life values for two-neutrino double beta decay: upgrade-2019. *AIP Advances*, 10(1):085003, 2020.

[75] Frederick James. *Statistical Methods in Experimental Physics*. World Scientific, 2nd edition, 2006.

[76] Alexander Daniel Piers and Alvaro Chavarria. *Results from a 3.1 kg day target exposure with skipper CCDs from DAMIC at SNOLAB and other beyond the standard model searches with semiconductor detectors*. PhD thesis, University of Washington, Seattle, 2023.

[77] V. Barinov, V.N. Gavrin, et al. Results of the baksan experiment on sterile transitions (best). *Phys. Rev. Lett.*, 128(23):232501, 2022.

[78] Borexino Collaboration. Experimental evidence of neutrinos produced in the cno fusion cycle in the sun. *Nature*, 587:577–582, 2020.

[79] D. Basilico, G. Bellini, J. Benziger, R. Biondi, B. Caccianiga, F. Calaprice, A. Caminata, A. Chepurnov, D. D'Angelo, A. Derbin, A. Di Giacinto, V. Di Marcello, X. F. Ding, A. Di Ludovico, L. Di Noto, I. Drachnev, D. Franco, C. Galbiati, C. Ghiano, M. Giammarchi, A. Goretti, M. Gromov, D. Guffanti, Aldo Ianni, Andrea Ianni, A. Jany, V. Kobychev, G. Korga, S. Kumaran, M. Laubenstein, E. Litvinovich, P. Lombardi, I. Lomskaya, L. Ludhova, I. Machulin, J. Martyn, E. Meroni, L. Miramonti, M. Misiaszek, V. Muratova, R. Nugmanov, L. Oberauer, V. Orekhov, F. Ortica, M. Pallavicini, L. Pelicci, Ö. Penek, L. Pietrofaccia, N. Pilipenko, A. Pocar, G. Raikov, M. T. Ranalli, G. Ranucci, A. Razeto, A. Re, N. Rossi, S. Schönert, D. Semenov, G. Settanta, M. Skorokhvatov, A. Singhal, O. Smirnov, A. Sotnikov, R. Tartaglia, G. Testera, E. Unzhakov, F. L. Villante, A. Vishneva, R. B. Vogelaar, F. von Feilitzsch, M. Wojcik, M. Wurm, S. Zavatarelli, K. Zuber, and G. Zuzel. Final results of borexino on cno solar neutrinos. *Phys. Rev. D*, 108:102005, Nov 2023.

[80] Abdallah El-Falou, Ahmet Camlica, Reza Mohammadi, Peter M. Levine, and Karim S. Karim. A monolithic amorphous-selenium/cmos single-photon-counting x-ray detector. *IEEE Transactions on Electron Devices*, 68(4):1746–1752, 2021.

[81] A. Camlica, A. El-Falou, R. Mohammadi, P. M. Levine, and K. S. Karim. Cmos-integrated single-photon-counting x-ray detector using an amorphous-selenium photoconductor with $11 \times 11 - \boldsymbol{\mu}\mathbf{m}^2$ pixels. In *2018 IEEE International Electron Devices Meeting (IEDM)*, pages 32.5.1–32.5.4, 2018.

[82] National Institute of Standards and Technology. Estar: Stopping powers and ranges for electrons. `https://physics.nist.gov/PhysRefData/Star/Text/ESTAR.html`. Accessed 2025-06.

[83] Behzad. Razavi. *Design of analog CMOS integrated circuits*. McGraw-Hill Education, New York, NY, second edition. edition, 2016.

[84] G Charpak, P Benaben, P Breuil, and V Peskov. Detectors for alpha particles and x-rays operating in ambient air in pulse counting mode or/and with gas amplification. *Journal of Instrumentation*, 3(02):P02006, feb 2008.

[85] Elena Dobrovinskaya, Leonid Lytvynov, and Valerian Pishchik. *Properties of Sapphire*, pages 55–176. Springer US, 01 1970.

[86] Y. Itikawa and A. Ichimura. Cross sections for collisions of electrons and photons with atomic oxygen. *Journal of Physical and Chemical Reference Data*, 19(3):637–651, 05 1990.

[87] L. M. Chanin, A. V. Phelps, and M. A. Biondi. Measurements of the attachment of low-energy electrons to oxygen molecules. *Phys. Rev.*, 128:219–230, Oct 1962.

[88] Guillaume Boissonnat, Jean-Marc Fontbonne, Jean Colin, Aurelien Remadi, and Samuel Salvador. Measurement of ion and electron drift velocity and electronic attachment in air for ionization chambers, 2016.

[89] N. L. Aleksandrov. Three-body electron attachment to o2 molecules in water-air mixtures in strong electric field. *Physics of Plasmas*, 32(4):043513, 04 2025.

[90] A Ponomarev and Nickolay Aleksandrov. Monte carlo simulation of electron detachment properties for o2- ions in oxygen and oxygen:nitrogen mixtures. *Plasma Sources Science and Technology*, 24, 04 2015.

[91] Yui Okuyama, Yuka Yasuzawa, and Hirotake Sugawara. Effects of a small amount of h2o on negative ion mobility and ion-molecule reactions in o2 at atmospheric pressure. *Electrical Engineering in Japan*, 216(1):e23413, 2023.

[92] D. W. Goodson, R. J. Corbin, and Lothar Frommhold. Electron avalanches in oxygen: Detachment from the diatomic ion o_2^-. *Phys. Rev. A*, 9:2049–2059, May 1974.

[93] Keithley Instruments, Inc. *Low Level Measurements Handbook: Precision DC Current, Voltage, and Resistance Measurements*. Keithley Instruments, Inc., Cleveland, Ohio, 7th edition, 2014.

[94] S. Kleinfelder, SukHwan Lim, Xinqiao Liu, and A. El Gamal. A 10000 frames/s cmos digital pixel sensor. *IEEE Journal of Solid-State Circuits*, 36(12):2049–2059, 2001.

[95] John H. Lau. *Flip Chip Technologies*. McGraw-Hill, 1996.

[96] G. LaRosa. Advanced flip chip packaging. In Rao R. Tummala, E. J. Rymaszewski, and Alan G. Klopfenstein, editors, *Microelectronics Packaging Handbook: Advanced Packaging*, pages 419–462. Springer, 2007.

[97] J. M. Luttinger, K. P. Rodbell, and G. Weisz. Sapphire as an insulating substrate material. *Journal of Applied Physics*, 31(7):1202–1205, 1960.

[98] Tansel Karabacak and Toh-Ming Lu. Enhanced step coverage by oblique angle physical vapor deposition. *Journal of Applied Physics*, 97(12):124504, 06 2005.

[99] Stephen A. Campbell. *Fabrication Engineering at the Micro- and Nanoscale*. Oxford University Press, 4 edition, 2018.

[100] G. Belev and S.O. Kasap. Reduction of the dark current in stabilized a-se based x-ray detectors. *Journal of Non-Crystalline Solids*, 352(9):1616–1620, 2006. Amorphous and Nanocrystalline Semiconductors - Science and Technology.

[101] Reza Mohammadi, Peter M. Levine, and Karim S. Karim. Experimental demonstration of the small pixel effect in an amorphous photoconductor using a monolithic spectral single photon counting capable cmos-integrated amorphous-selenium sensor. In *2022 International Electron Devices Meeting (IEDM)*, pages 467–470, 2022.

[102] Ahmad Al Shboul, Mohsen Ketabi, and Ricardo Izquierdo. Conductive green graphene inks for printed electronics. In *2021 IEEE 16th Nanotechnology Materials and Devices Conference (NMDC)*, pages 1–4, 2021.

[103] Zain Hussain Warsi and Karim Karim. *Design, Fabrication and Characterization of a Unipolar Charge Sensing Amorphous Selenium X-ray Detector*. PhD thesis, University of Waterloo, Waterloo, 2023.